Megathrust Heterogeneity, Crustal Accretion, and a Topographic Embayment in the Western Nepal Himalaya : Insights From the Inversion of Thermochronological Data

Fan, Suoya

2022-07

Fan , S , Murphy , M A , Whipp , D M , Saylor , J E , Copeland , P , Hoxey , A K , Taylor , M H & Stockli , D F 2022 , ' Megathrust Heterogeneity, Crustal Accretion, and a Topographic Embayment in the Western Nepal Himalaya : Insights From the Inversion of Thermochronological Data ' , Tectonics , vol. 41 , no. 7 , e2021TC007071 . https://doi.org/10.1029/2021TC007071

http://hdl.handle.net/10138/348264
https://doi.org/10.1029/2021TC007071

Tectonics®

RESEARCH ARTICLE
10.1029/2021TC007071

Key Points:

- Thermochronologic data and thermokinematic modeling results suggest a complex 3D geometry of the megathrust in the western Nepal Himalaya
- Crustal accretion along the midlower crustal ramp in the megathrust is a mechanism of maintaining the edge of a plateau-like landscape
- The development of the 3D megathrust geometry may have controlled the first-order evolution of an embayment and regional drainage system

Supporting Information:

Supporting Information may be found in the online version of this article.

Correspondence to:

S. Fan,
suoyafan@ucsb.edu

Citation:

Fan, S., Murphy, M. A., Whipp, D. M., Saylor, J. E., Copeland, P., Hoxey, A. K., et al. (2022). Megathrust heterogeneity, crustal accretion, and a topographic embayment in the western Nepal Himalaya: Insights from the inversion of thermochronological data. *Tectonics*, *41*, e2021TC007071. https://doi.org/10.1029/2021TC007071

Received 12 SEP 2021
Accepted 26 JUN 2022

Megathrust Heterogeneity, Crustal Accretion, and a Topographic Embayment in the Western Nepal Himalaya: Insights From the Inversion of Thermochronological Data

Suoya Fan[1,2], Michael A. Murphy[1], David M. Whipp[3], Joel E. Saylor[4], Peter Copeland[1], Andrew K. Hoxey[5], Michael H. Taylor[5], and Daniel F. Stockli[6]

[1]Department of Earth and Atmospheric Sciences, University of Houston, Houston, TX, USA, [2]Now at Department of Earth Science, University of California, Santa Barbara, CA, USA, [3]Department of Geosciences and Geography, Institute of Seismology, University of Helsinki, Helsinki, Finland, [4]Department of Earth, Ocean and Atmospheric Sciences, University of British Columbia, Vancouver, BC, Canada, [5]Department of Geology, University of Kansas, Lawrence, KS, USA, [6]Department of Geological Sciences, Jackson School of Geosciences, University of Texas at Austin, Austin, TX, USA

Abstract Between 81°30′E and 83°E, the Himalayan range's "perfect" arcuate shape is interrupted by an embayment. We hypothesize that thrust geometry and duplexing along the megathrust at midlower-crustal depths play a leading role in growth of the embayment as well the southern margin of the Tibetan plateau. To test this hypothesis, we conducted thermokinematic modeling of published thermochronologic data from the topographic and structural embayment in the western Nepal Himalaya to investigate the three-dimensional geometry and kinematics of the megathrust at midlower-crustal depths. Models that can best reproduce observed cooling ages suggest that the megathrust in the western Nepal Himalaya is best described as two ramps connected by a long flat that extends further north than in segments to the east and west. These models suggest that the high-slope zone along the embayment lies above the foreland limb of an antiformal crustal accretion zone on the megathrust with lateral and oblique ramps at midlower-crustal depths. The lateral and oblique ramps may have initiated by ca. 10 Ma. This process may have controlled along-strike variation in Himalayan-plateau growth and therefore development of the topographic embayment. Finally, we analyze geological and morphologic features and propose an evolution model in which landscape and drainage systems across the central-western Himalaya evolve in response to crustal accretion at depth and the three-dimensional geometry of the megathrust. Our work highlights the importance of crustal accretion at different depths in orogenic-wedge growth and that the midlower crustal accretion determines the location of plateau edge.

1. Introduction

For large orogens, the roles of the geometry and kinematics of the megathrust in controlling strain accumulation and the feedback mechanisms between deformation and erosion are keys to understanding the growth of the orogenic wedge and the evolution of its morphology. The Himalayan orogenic wedge is a classical natural laboratory to study this, because it exhibits both along-strike consistency in first-order tectonic-morphologic framework and pronounced along-strike segmentation. Early studies show that the tectonostratigraphy, major shear zones, deformation styles, and morphologic features are generally continuous along the strike of the >1,500 km orogen (Burg & Chen, 1984; Gansser, 1964; Heim & Gansser, 1939; Le Fort, 1975; Pêcher, 1989; Yin, 2006; Figure 1). Along with these features, concentrated microseismicity, maximum horizontal strain rate, zones of high river gradient, and zones of high relief are interpreted to be collocated along a small circle or "perfect arc" (Bendick & Bilham, 2001; Seeber & Gornitz, 1983). This arc is interpreted to represent the active-uplift front of the high Himalaya based on geological, geophysical, and geomorphological observations and to mark the plateau margin, the transition between a taper-shaped outer wedge and a high-elevation, low-relief inner-wedge plateau (Fan & Murphy, 2021 and references therein). It is thought to form through deformation associated with a midlower crustal ramp in the megathrust, which connects an upper-crustal flat below the outer wedge and a flat seismic reflector extending beneath Tibet (Hauck et al., 1998; Nábělek et al., 2009). In this paper, we use "uplift" to refer to the "rock uplift" discussed in England and Molnar (1990).

Megathrust kinematic models can be classified into three main groups (Figure 2): (a) thrusting of the orogenic wedge over a crustal ramp (Cattin & Avouac, 2000; Coutand et al., 2014; Elliott et al., 2016; Gansser, 1964; Jackson & Bilham, 1994; Lavé & Avouac, 2001; Robert et al., 2009, 2011), (b) thrusting of the orogenic wedge

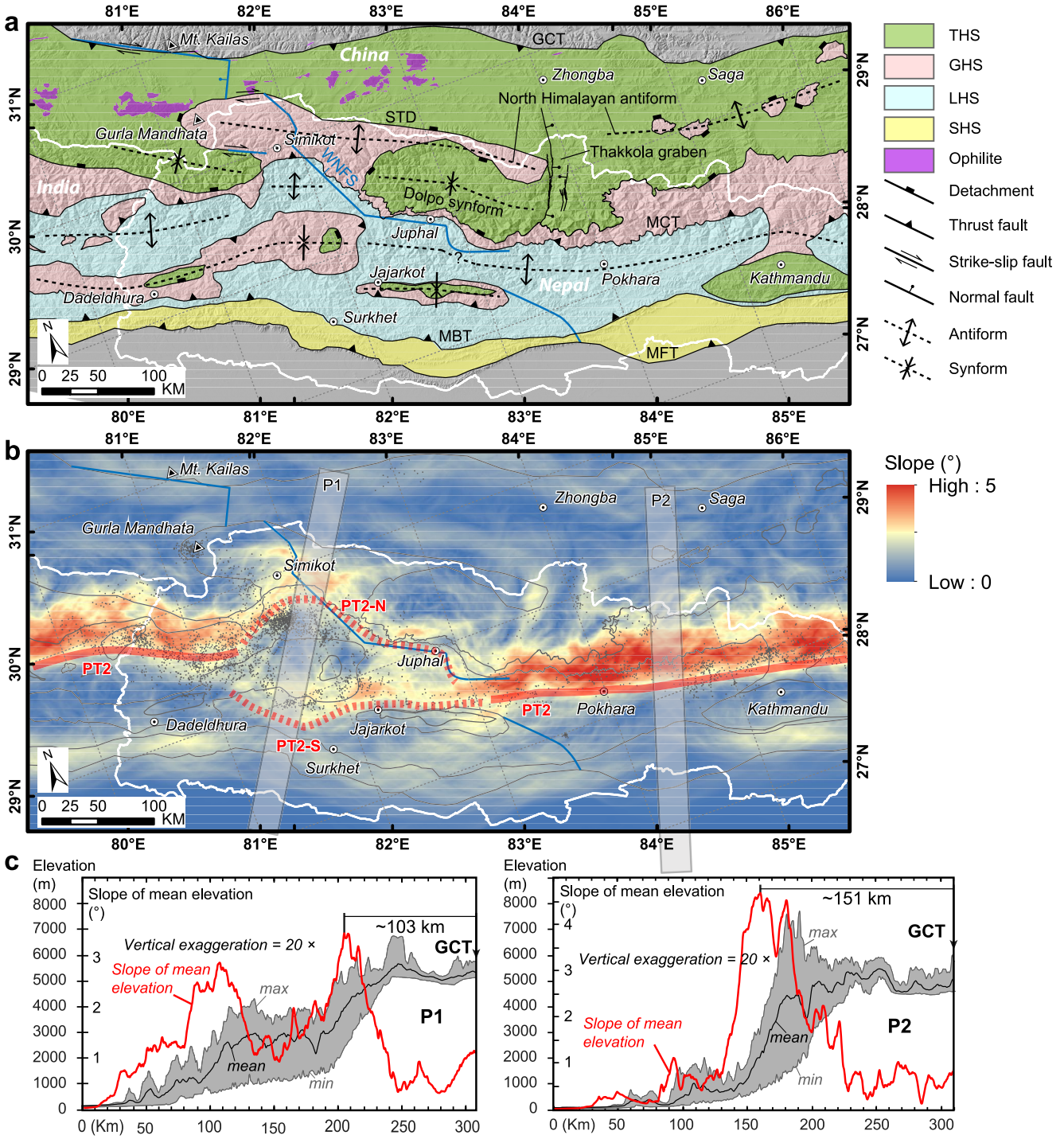

Figure 1. Geological map (a) and slope of mean elevation map (b) of central-western Nepal and adjacent areas and (c) topographic swath profiles and slope of mean elevation profiles of western and central Nepal Himalaya. Gray dots in (b) show earthquake hypocenters from 1995 to 2004, relocated by Ader et al. (2012). Gray lines in (b) are major faults shown in (a). Slope of mean elevation was calculated by first smoothing the topography by taking the mean within a 25 km moving window and then calculating the slope of the resulting grid. THS, Tethyan Himalayan Sequence; GHS, Greater Himalayan Sequence; LHS, Lesser Himalayan Sequence; SHS, Sub-Himalayan Sequence; GCT, Great Counter Thrust; STD, South Tibet Detachment; MCT, Main Central Thrust; MBT, Main Boundary Thrust; MFT, Main Frontal Thrust; WNFS, Western Nepal Fault System.

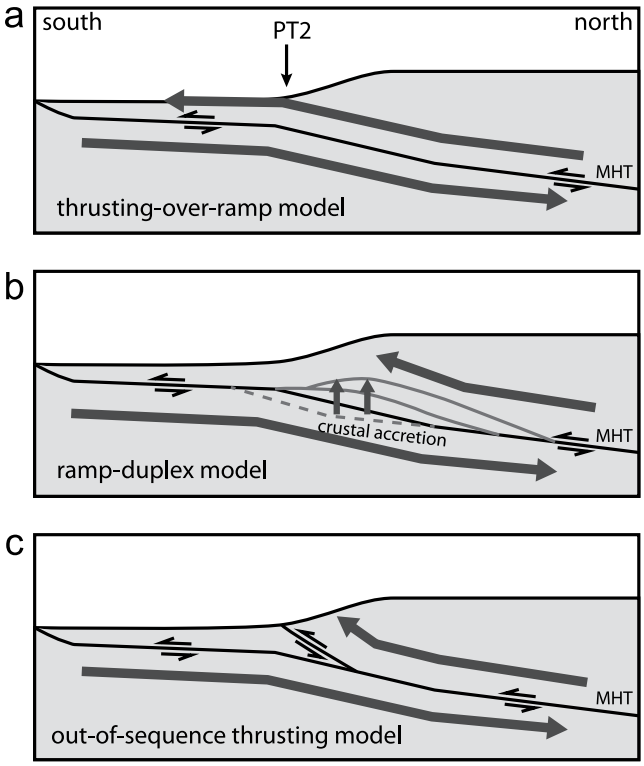

Figure 2. Simplified sketch of the kinematic models of Main Himalayan Thrust (MHT) explains the formation of physiographic transition (PT2) between outer wedge and inner wedge. (a) Overthrusting and underthrusting along the MHT ramp. (b) Crustal accretion in the form of duplexes along MHT ramp. (c) Out-of-sequence thrusting at the physiographic transition.

over a crustal ramp accompanied by localized transfer of material from the footwall to hanging wall via duplexing or accretion (Adams et al., 2016; Avouac, 2003; Bollinger et al., 2004, 2006; Cannon & Murphy, 2014; Fan & Murphy, 2021; Grandin et al., 2012; Herman et al., 2010; Landry et al., 2016; Stübner et al., 2018), and (c) out-of-sequence thrusting (Harrison et al., 1997; Hodges et al., 2004; Thiede et al., 2004, 2005; Whipple et al., 2016; Wobus et al., 2003, 2005, 2006) or a hybrid of out-of-sequence thrusting and duplex model. Besides the dispute over the kinematics controlling the active-uplift zone, an increasing number of studies challenge the notion of a "perfect arc" orogenic system with evidence of noncylindricity in surface geology, wedge morphology, and the deep megathrust geometry (Cannon et al., 2018; Dal Zilio et al., 2020a; Duncan et al., 2003; Eugster et al., 2018; Fan & Murphy, 2021; Hetényi et al., 2016; Yin, 2006). One pronounced deviation from the "perfect arc" shape of the Himalaya is the bifurcation of several features defining the active-uplift front in western Nepal Himalaya (Figure 1; Harvey et al., 2015). The northern branch of the bifurcation has been interpreted to represent the active-uplift zone, implying that there is a recession or embayment in the active-uplift front of the wedge (Cannon et al., 2018; Fan & Murphy, 2021). Some studies have ascribed this along-strike anomaly to an along-strike difference in the number and location of ramps in the Himalayan megathrust, the Main Himalayan Thrust (MHT; Fan & Murphy, 2021; Harvey et al., 2015; Robert et al., 2011; van der Beek et al., 2016). This conceptual interpretation is consistent with the observation of a longer upper-crustal flat in the megathrust in western Nepal than in some other sectors (Subedi et al., 2018) and the pattern of microseismicity (Ader et al., 2012; Hoste-Colomer et al., 2018). However, in western Nepal, although the MHT upper-crustal flat and the structures above it in the outer wedge are well-studied (DeCelles et al., 2020 and references therein), the geometry and kinematics of the MHT at aseismic slip depths are not well understood.

A better understanding of the geometry of the megathrust in western Nepal Himalaya is also crucial to assess seismic hazard in the region. Within a thickened continental crust, the downdip limit of the seismogenic zone along a megathrust should be located where the megathrust intersects the temperature-controlled transition between seismic and aseismic slip depths (Hyndman et al., 1997). Therefore, the megathrust geometry should be the determining factor for the along-strike variation in the location of the downdip limit of the seismogenic zone. The along-strike complexity of this limit in the Himalaya is implied by the heterogeneity shown in coupling models derived from geodetic data (Ader et al., 2012; Dal Zilio et al., 2020a; Jouanne et al., 2017; Li et al., 2018; Marechal et al., 2016; Sreejith et al., 2018; Stevens & Avouac, 2015; Yadav et al., 2019). The potential along-strike changes in the geometry of the MHT require the existence of lateral or oblique ramps. These ramps, including frontal ramps at the front of the wedge, could act as barriers to rupture propagation during large earthquakes, as suggested by studies on the 2015 M_w 7.8 Gorkha earthquake in central Nepal (Bai et al., 2019; Duputel et al., 2016; Elliott et al., 2016; Hubbard et al., 2016; Kumar et al., 2017; Wang et al., 2017, 2019; Zhang et al., 2017). In western Nepal Himalaya, the along-strike extent of the embayment approximately corresponds to the region devastated in the 1505 AD earthquake (Bollinger et al., 2016), and other large historical earthquakes have been reported (Ghazoui et al., 2019; Hossler et al., 2016; Murphy et al., 2014). These observations suggest significant seismic hazard for western Nepal and that the megathrust lateral ramps may control rupture propagation.

To address these issues, we investigate the geometry and kinematics of the megathrust from the perspective of thermokinematics. In this contribution, we report new zircon (U-Th)/He ages. Most of our samples are located in the eastern limb of the embayment. The rest of the samples are located in the hinterland of the Himalayan orogenic plateau, the hinterland or inner wedge part of the Himalayan range which has a plateau topography. Previously published thermochronologic data are used to inform inversion models with different megathrust kinematics. We also take this opportunity to discuss the general evolution of crustal ramps and topography in western Nepal by comparing our study with observations in adjacent areas. We conclude by summarizing sedimentary

studies across the Himalaya orogen and propose a conceptual model for the landscape and drainage system evolution that highlights the role of deep crustal accretion in the development of the Himalayan orogenic plateau.

2. Geological Setting

2.1. Tectonostratigraphy and Structures

The Himalayan orogen is characterized by several rock sequences juxtaposed by major east-west-striking shear zones (Gansser, 1964; Le Fort, 1975; Yin, 2006). From structurally high to low levels in the thrust wedge, these rock sequences include the Tethyan Himalayan Sequence (THS), the Greater Himalayan Sequence (GHS), the Lesser Himalayan Sequence (LHS), and the Siwalik Group (SG; Figure 1). The THS is a deformed package of metasedimentary rocks that experienced greenschist to amphibolite facies metamorphism (Burchfiel et al., 1992; Gaetani & Garzanti, 1991; Liu & Einsele, 1994; Murphy & Yin, 2003; Myrow et al., 2009). The THS primarily crops out from the Indus-Yarlung suture zone to the South Tibet Detachment (STD), a top-to-the-north shear zone cut by north-dipping normal brittle fault (Burchfiel et al., 1992; Burg et al., 1984; Carosi et al., 1998; Coleman, 1996; Cottle et al., 2015a; Edwards et al., 1996; Godin et al., 2006b; Grujic et al., 2002; Hodges et al., 1992; Kellett & Grujic, 2012; Kellett et al., 2010; Searle, 2010; Webb et al., 2007). The GHS, in the footwall of the STD, is composed of middle amphibolite facies to lower granulite facies metasedimentary and metaigneous rocks (Iaccarino et al., 2017; Kohn, 2014; Martin et al., 2009; Murphy et al., 2002; Pêcher, 1989; Searle & Godin, 2003; Vannay & Hodges, 1996). It is juxtaposed against the LHS along the Main Central Thrust (MCT), a top-to-south thrust-sense shear zone (Brunel, 1986; Burg & Chen, 1984; Robinson et al., 2003; Schelling, 1992). The MCT is primarily active during the late Oligocene-middle Miocene (e.g., Braden et al., 2020; Carosi et al., 2018; Catlos et al., 2018; Cottle et al., 2015a; Hubbard & Harrison, 1989; Kohn et al., 2005; Larson et al., 2015; Montomoli et al., 2013; Yin, 2006). Some segments of the MCT are known to have been reactivated in the late Miocene-Pliocene (e.g., Braden et al., 2018, 2020; Catlos et al., 2001, 2018; Montemagni et al., 2019). The STD is coeval with the main active stage of the MCT and ceased moving in the early Miocene in the western Nepal Himalaya (Cottle et al., 2015b; Godin et al., 2006a; Hodges et al., 1992, 1998; Murphy & Harrison, 1999; Searle & Godin, 2003). Between the STD and MCT, within the GHS, some studies report tectonic or metamorphic discontinuities, which have been interpreted to accommodate in-sequence thrusting before the initiation of the MCT (e.g., Carosi et al., 2018; Larson et al., 2015; Montomoli et al., 2015). Toward the end of the time that the STD-MCT system was active (ca. 19-13 Ma), a series of midcrustal culminations referred to as the North Himalayan antiform developed in the central Himalayan hinterland and exposed the GHS (e.g., Godin et al., 2006a; Larson et al., 2010; Lee & Whitehouse, 2007; Lee et al., 2000; Figure 1). In the western Nepal Himalaya, the Northern Himalayan antiform is characterized by an east-west-trending belt of dome-shaped outcrops of GHS rocks from 81°E to 92°E (Figure 1). The Thakkhola graben is bounded by several steeply dipping north-south striking normal faults (Baltz et al., 2021; Hurtado et al., 2001), and the Gurla Mandhata area is a metamorphic core complex bounded by the Gurla Mandhata-Humla fault system (Murphy & Copeland, 2005; Murphy et al., 2002). They both developed mainly starting from middle-late Miocene and accommodated orogen-parallel extension (Brubacher et al., 2020; Coleman & Hodges, 1995; McCallister et al., 2014; Murphy & Copeland, 2005; Murphy et al., 2002). Fan and Murphy (2021) reconciled the coeval orogen-normal shortening and orogen-parallel extension and the difference in the amount of extension of these two features in a 3D conceptual model of oblique convergence in an arcuate orogen. The LHS consists of lower greenschist-amphibolite-facies to lower-amphibolite-facies metasedimentary rocks and is deformed by a duplex system that formed in the late Miocene after ca. 10 Ma within the outer wedge (e.g., DeCelles et al., 2001; Robinson et al., 2006; Srivastava & Mitra, 1994; Webb, 2013). Growth of the duplex led to the folding of the MCT shear zone structurally above, which is presently exposed in synformal klippen in the outer wedge (DeCelles et al., 2001; Pearson & DeCelles, 2005). The LHS duplex anticlinorium and Northern Himalayan antiform usually make the region between them form synformal half-klippe, e.g., the Dolpo THS synform (Figure 1). The Main Boundary Thrust (MBT) juxtaposes the LHS against the SG. The SG were foreland basin deposits since the middle Miocene and have been incorporated into the thrust wedge through postdepositional deformation (Baral et al., 2016; Bernet et al., 2006; Mugnier et al., 1999; van der Beek et al., 2006). The SG is separated from the undeformed foreland by the Main Frontal Thrust (MFT), the surface trace of the MHT. The MBT and MCT sole into the MHT at depth. In the central-western Himalaya, the surface geology suggests the existence of MHT lateral or oblique ramps that affect forelandward propagation. Between the Thakkhola graben and the Gurla Mandhata area, the trace of the MCT, LHS duplex, and the axis of the folded Almora-Dadeldhura klippe, all shift toward the hinterland (north)

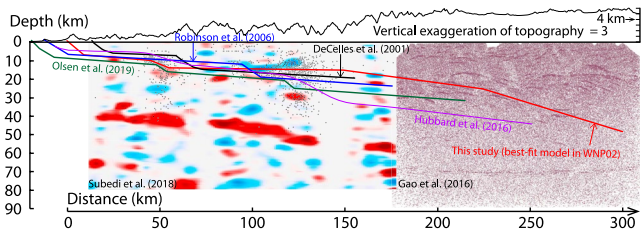

Figure 3. A comparison between different models of the Main Himalayan Thrust (MHT) in the western Nepal Himalaya. The red line shows the geometry of preferred model in this study. Gray dots show the earthquake hypocenters projected to the profile from within 20 km. The data include earthquakes from December 2014 to November 2015 reported by Hoste-Colomer et al. (2018) and earthquakes from 1995 to 1999 recorded by National Seismic Center and relocated by Ader et al. (2012). Image on the left is P-to-S receiver function migration image reported by Subedi et al. (2018) in which the red and blue represent high and low PS/P amplitude, respectively. The seismic-reflection profile image on the right is reported by Gao et al. (2016). For original interpretation of the images, refer to the original papers. Notice the reflector along the upper-crustal flat of the MHT and the duplexes in the hinterland.

in western Nepal. This results in the alignment of antiformal structures, such as LHS duplexes, and synformal structures, such as GHS klippen and THS half-klippen, along their strike (DeCelles et al., 2020; Fan & Murphy, 2021; Figure 1). The Western Nepal Fault System (WNFS) is an active strike-slip fault system that obliquely cuts across the orogen and is interpreted to operate as the eastern boundary of a westward translating continental forearc sliver (Murphy et al., 2014; Silver et al., 2015). It is partially collocated with the transitional positions between the antiformal and synformal structures and is interpreted to have developed by exploiting preexisting old structures and the hypothesized MHT lateral or oblique ramps (Fan & Murphy, 2021).

2.2. Topography and Landscape

The topography of the Himalayan wedge is characterized by a sharp physiographic transition from high slopes between the high-elevation hinterland plateau and the lower slopes that mark the low-elevation frontal wedge (PT2 of Hodges et al., 2001). It is located at the base of a narrow high-slope zone connecting the inner wedge characterized by high-elevation, low-relief plateau landscape, and the outer wedge characterized by a taper-shaped regional slope (Figure 1). PT2 exhibits along-strike variations and is usually collocated with features that define the active-uplift front of the Himalaya (e.g., Duncan et al., 2003; Harvey et al., 2015; Morell et al., 2015). The young cooling ages along this zone suggest rapid exhumation (e.g., Blythe et al., 2007; Copeland et al., 1991; Johnston et al., 2020; Wobus et al., 2003). The above-mentioned bifurcation of the high-slope zone in western Nepal Himalaya obscures the plateau-taper pattern of the topography there (Figure 1). The northern and south branches of PT2 in western Nepal are referred to as PT2-N and PT2-S (Harvey et al., 2015).

2.3. Megathrust Models

Although some MHT models explain the specific location of the active-uplift front of the high Himalaya and supporting data sets in other areas in Himalaya (e.g., Célérier et al., 2009; Coutand et al., 2014; Ghoshal et al., 2020; Landry et al., 2016; Stübner et al., 2018), no such model exists for western Nepal. Based on low-temperature thermochronologic ages and geomorphology, several conceptual models suggest that an upper-crustal flat extends further to the north compared with along-strike adjacent segments (Harvey et al., 2015; van der Beek et al., 2016). Based on a better understanding of the MHT in the area ruptured by the Gorkha earthquake, Hubbard et al. (2016) proposed a three-dimensional model for the MHT across Nepal. Similarly, by integrating various data sets and a thickness model of the Himalayan high-grade core, Fan and Murphy (2021) introduced lateral and oblique ramps to the 2D conceptual model of the MHT in western Nepal and proposed a 3D conceptual model explaining the embayment of the active-uplift front and the along-strike change in the surface geology. Several studies focusing on the fold-and-thrust belt in the outer wedge of the Himalaya propose MHT models based on a structural restoration (DeCelles & DeCelles, 2001; DeCelles et al., 2020; Olsen et al., 2019; Robinson, 2008; Robinson & McQuarrie, 2012; Figure 3). These models can well explain the detailed structures in the outer wedge to the south of the PT2 but cannot resolve the structures in the inner wedge and the midlower crustal ramp in the MHT. They also fail to explain the first-order landscape because the northern MHT ramp in these models is usually located below the area between the PT2-S and PT2-N, where the landscape is relatively flat and of low-relief (Figure 3).

Receiver function analysis of teleseismic waveforms in western Nepal suggests a longer upper-crustal flat in MHT compared to central Nepal. This flat in the MHT connects to a long, gently dipping ramp that extends northward to lower-crustal depths (Subedi et al., 2018; Figure 3). However, using the available data, the geometry of this ramp is not precisely located. Subedi et al. (2018) interpret the ramp geometry based on the change in depth between the upper-crustal reflectors and several short reflectors at the northern end of the profile. The reflectors at the northern end are consistent with lower-crustal reflectors on the other receiver function profile image that extends from the west of the Gurla Mandhata metamorphic core complex to the south of South Tibet (Xu et al., 2017). A deep seismic-reflection profile along a transect close to the profile in Xu et al. (2017) also shows a middle-lower crustal duplex structurally above the midlower-crustal reflector (Gao et al., 2016). The foci

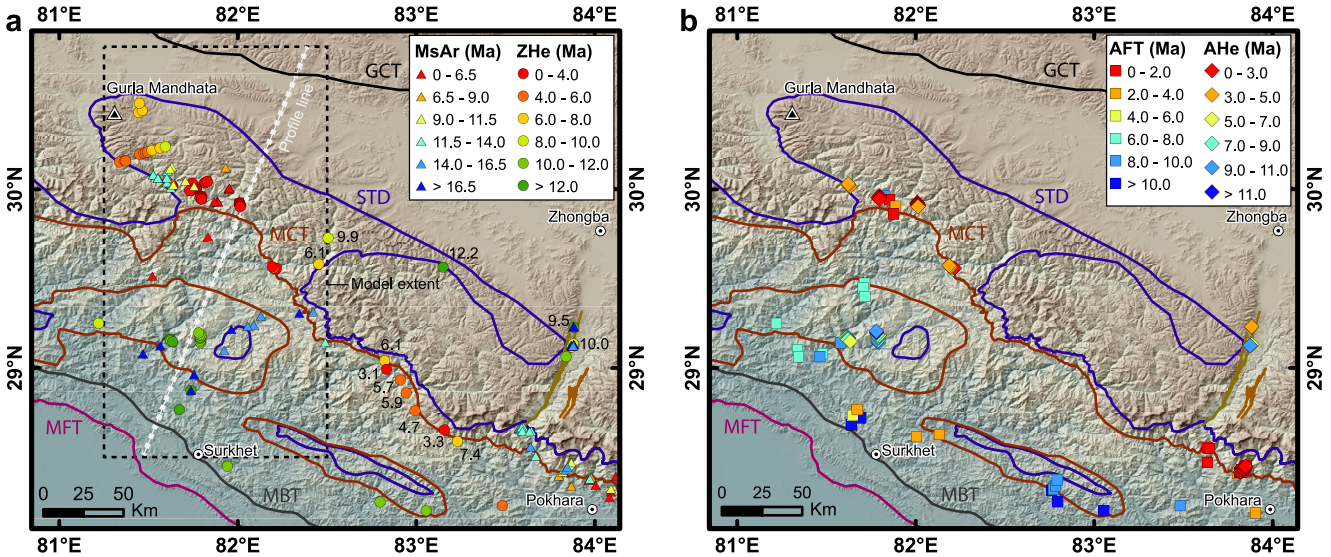

Figure 4. Previously reported and new thermochronologic ages in the western Nepal Himalayan area. The dashed box in (a) shows the extent of the thermokinematic models in this study. The ZHe ages labeled with age values are newly reported ages in this study. Previously published data are from Vannay and Hodges (1996), Godin et al. (2001), Robert et al. (2011), Nadin and Martin (2012), Sakai et al. (2013), Mercier (2014), McCallister et al. (2014), Harvey (2015), Martin et al. (2015), Nagy et al. (2015), Gibson et al. (2016), van der Beek et al. (2016), Soucy La Roche et al. (2018), Braden et al. (2020), Brubacher et al. (2020), and DeCelles et al. (2020). MsAr, muscovite $^{40}Ar/^{39}Ar$ age; ZHe, zircon (U-Th)/He age; AFT, apatite fission track age; AHe, apatite (U-Th)/He age.

of earthquakes in western Nepal also suggest that the seismogenic part of the MHT extends further to the north compared to areas along-strike (Ader et al., 2012; Hoste-Colomer et al., 2018). However, none of these models are based on geophysical data along a complete transect from the lower Himalaya to the higher Himalaya of the embayment in the western Nepal area, and none have been tested with geologic data.

3. Thermochronologic Data

3.1. Sample and Methods

In order to investigate the geometry and kinematics of the MHT in western Nepal and the correlation between the 3D geometry of the MHT (e.g., lateral and oblique ramp locations) with the embayment, we carried out thermokinematic modeling along a transect that extends across the apex of the embayment. We then compare the modeling results with our new thermochronologic data along the eastern limb of the embayment. The data used in the modeling are from published studies and are described later.

Zircon (U-Th)/He (ZHe) dating was carried out because of the sensitivity of ZHe ages to recent exhumation over a time span of several million years in the Himalaya. The closure temperature of the ZHe thermochronometer is affected by several factors, such as the chemical composition of the crystals, concentration of radiation damage, grain size, and cooling rate (Reiners, 2005; Reiners et al., 2004). For typical plutonic cooling rates and crystal sizes, the closure temperature is about 170–190 °C (Reiners et al., 2004). Therefore, it can record the exhumation history through the upper about 5–8 km of the crust. In an active region, such as the Himalaya, where the highest exhumation rate close to the PT2 can reach several mm/yr, the ZHe ages can record cooling history in the past <3 million years.

We analyzed 12 samples. Seven are from the northern branch of PT2 (Figure 4). These data fill a data gap between far-western Nepal along the Karnali River transect and western Nepal. The other samples are from the inner wedge. The samples' locations, lithology, and units are listed in Table S1 in Supporting Information S1.

Samples were processed for ZHe dating at the thermochronology lab at University of Texas, Austin (refer to Text S1 in Supporting Information S1 for analytical procedure). We usually analyzed three grains for each sample, but from DG-10 and DF-3 we analyzed four grains and two grains, respectively. Some aliquots were discarded on the basis of anomalous isotopic values and others because they yielded outlier ages defined as being >30% older or younger than the rest of the grains in their respective samples.

Table 1
Zircon (U-Th)/He Dating Results[a]

Sample	Age (Ma)	Error (Ma)	U (ppm)	Th (ppm)	^{147}Sm (ppm)	He (nmol/g)	Mass (μg)	Ft	ESR	Mean age (Ma)	Error (1σ)
DG-10-2	3.3	0.26	505.5	28.1	0.0	6.3	1.99	0.70	36.31		
DG-10-3	3.3	0.26	309.0	9.2	−3.0	4.1	3.18	0.74	42.97		
DG-10-4	3.4	0.27	703.7	39.8	0.8	10.7	11.07	0.82	65.07		
DG-10-5	3.1	0.25	551.7	10.1	−1.7	7.2	5.67	0.78	52.54	3.27	0.06
DG-38-2	2.9	0.23	124.9	83.6	0.0	1.6	3.16	0.72	41.28		
DG-38-3	3.2	0.26	240.7	105.4	0.0	3.1	2.04	0.68	35.25		
DG-38-4	3.1	0.25	673.9	182.9	0.0	8.3	1.90	0.69	36.24	3.08	0.07
DH-10-1	5.7	0.45	481.3	203.7	2.6	13.4	14.34	0.83	69.80		
DH-10-2	5.5	0.44	300.0	75.5	0.0	6.9	3.83	0.74	43.37		
DH-10-3	7.3	0.58	518.3	85.7	1.4	17.5	13.10	0.83	68.71	6.14	0.46
Dolpo-04-1	*16.3*	*1.30*	*253.9*	*87.0*	*0.8*	*19.7*	*11.78*	*0.82*	*66.09*		
Dolpo-04-2	12.1	0.97	278.5	98.3	0.0	15.2	6.24	0.77	50.57		
Dolpo-04-3	12.2	0.98	171.6	61.7	0.8	10.0	12.01	0.82	64.83	12.20	0.03
DF-3-2	10.0	0.80	1141.8	194.6	0.0	46.4	2.91	0.72	40.72		
DF-3-3	*4.7*	*0.37*	*190.4*	*59.5*	*1.8*	*3.9*	*5.13*	*0.76*	*49.33*	10.0	0.80
DF-4-3	10.5	0.84	1649.4	30.2	1.3	74.1	7.23	0.79	54.31		
DF-4-1	9.7	0.78	1720.5	55.4	1.3	71.2	7.23	0.78	52.79		
DF-4-2	8.4	0.67	1551.4	27.8	0.0	41.8	0.86	0.60	26.03	9.53	0.51
DG-12-1	8.0	0.64	689.6	81.1	0.0	21.4	2.64	0.70	37.73		
DG-12-2	*14.1*	*1.13*	*1937.3*	*46.7*	*0.0*	*93.0*	*1.37*	*0.63*	*28.95*		
DG-12-3	6.8	0.55	342.1	54.0	0.0	7.8	0.94	0.60	26.66	7.40	0.41
DG-22-1	6.2	0.49	321.2	88.3	2.2	9.5	16.75	0.84	72.47		
DG-22-2	4.6	0.36	439.6	34.1	0.0	8.3	4.78	0.76	46.31		
DG-22-3	3.3	0.27	262.8	37.6	0.0	3.4	2.30	0.70	37.83	4.68	0.67
DG-29-1	6.7	0.54	1143.0	35.4	0.0	29.8	2.65	0.71	38.82		
DG-29-2	5.2	0.42	136.1	74.8	1.9	3.6	15.10	0.83	72.20		
DG-29-3	5.8	0.46	514.7	83.8	0.0	13.1	6.78	0.79	55.59	5.91	0.36
DG-30-1	5.5	0.44	281.9	30.1	1.5	7.5	30.41	0.87	91.30		
DG-30-2	6.4	0.51	301.1	44.1	1.2	9.8	136.73	0.92	151.44		
DG-30-3	5.2	0.42	166.8	41.4	1.5	4.2	18.85	0.84	75.56	5.69	0.29
TB10-12-1	5.4	0.43	294.9	97.9	1.9	7.5	14.49	0.82	66.64		
TB10-12-2	6.8	0.54	322.2	75.5	0.0	10.4	17.24	0.84	73.28		
TB10-12-3	*16.5*	*1.32*	*248.9*	*97.5*	*1.0*	*19.3*	*8.97*	*0.80*	*57.83*	6.06	0.50
TB10-9-1	11.7	0.93	1054.0	90.3	21.2	57.8	24.09	0.85	80.46		
TB10-9-2	10.2	0.82	794.7	106.4	10.7	39.7	45.06	0.88	99.95		
TB10-9-3	7.7	0.62	542.8	86.0	5.1	20.2	31.07	0.86	86.76	9.87	0.95

[a]Ft is the alpha ejection correction factor. ESR is equivalent sphere radius. Data in italic indicate outliers that were discarded in mean age calculation. The age error is the standard deviation between aliquots divided by the square root of the number of aliquots.

3.2. Results

Analytical results of our samples are reported in Table 1. Samples from south of the Dolpo synform have ZHe mean ages that range from 3.1 to 7.4 Ma. Two samples among them are 3.1 and 3.3 Ma. These young ages are

consistent with or slightly older than the ages reported at the active-uplift front, though they are closer to the front of the orogen compared with the young cooling ages reported at the apex of the topographic embayment in western Nepal Himalaya (Figure 4). The samples from the inner wedge have ZHe mean ages that range from 9.5 to 12.2 Ma, significantly older than the samples from the southern Dolpo area and from the apex of the topographic embayment, though they approximately align well with the samples of young cooling ages at the apex of the topographic embayment along the strike of the northern Himalayan anticline (Figure 4). These old ages are consistent with recently reported ages close to the northern Himalayan antiform in the inner wedge along the Thakkhola graben (Brubacher et al., 2020).

4. Thermokinematic Modeling

To test the geometric and kinematic models of the MHT, we conducted thermokinematic modeling by using a modified version of the software Pecube (Braun, 2003; Braun et al., 2012). Models are evaluated by comparing the observed ages obtained from sample analyses with ages predicted by the software. To quantitatively do this, the software calculates the misfit using a goodness-of-fit statistic Φ

$$\Phi = \frac{1}{n}\sqrt{\sum_{i=1}^{n} \frac{(PredAge_i - ObsAge_i)^2}{{\sigma_i}^2}}$$

where n is the number of thermochronometer ages, *PredAge* and *ObsAge* are the ages predicted by Pecube and obtained from sample analyses, respectively, and σ is the 1-sigma uncertainty in the observed age.

4.1. Modeling Extent and Inversion Input Data

Conceptual models describe a network of oblique ramps to explain along-strike changes in the geometry of the MHT (Fan & Murphy, 2021; Hubbard et al., 2016). In this study, we focus on explaining the most representative sector of the embayment along the Karnali River transect, where it reaches its largest recession (Figure 4). Because faults in Pecube can only be defined by a constant strike (i.e., no lateral ramp can be incorporated), we use the MHT of the Karnali transect to define the megathrust of the entire model and only use the ages that are representative of the Karnali transect in the model.

Thermochronologic ages used in the modeling are reported from multiple dating systems, including muscovite $^{40}Ar/^{39}Ar$ (MsAr) ages, zircon and apatite (U-Th)/He (ZHe and AHe, respectively) ages, and apatite fission track (AFT) ages (Braden et al., 2020; Harvey, 2015; McCallister et al., 2014; Mercier, 2014; Nagy et al., 2015; Soucy La Roche et al., 2018; van der Beek et al., 2016). We selected the data for modeling from published data sets following criteria as follows: (a) we do not use the data out of the swath of our interested section because those samples might have significantly different thermal histories from the rocks within the swath due to the existence of lateral and oblique ramps of the MHT; (b) we do not use data that may be affected by the upper-crustal ramp of the MHT in the outer wedge close to the PT2-S because this is outside the area of interest; (c) we do not use ages older than 16 Ma because several studies suggest that the dynamics of the Himalayan orogen and thus the exhumation pattern changed significantly during the middle Miocene and resolving the complex evolution history in this transition is not a goal of this study (e.g., DeCelles et al., 2011; Husson et al., 2014; Mugnier & Huyghe, 2006; Webb et al., 2017). Some data are close to the interpreted lateral ramps. We do not use them in the inversion modeling or calculating the misfit values, but we still use the algorithm to estimate their ages in the forward model and incorporate them in the age-comparison plot for discussion. Close to the PT2-N, both ca. 6 and 9–10 Ma MsAr ages are reported along Karnali transect, but MsAr ages reported along the active-uplift front in other sectors in Himalaya are mostly ca. 6 Ma or younger. The reason for the large difference in the MsAr cooling ages over a short distance along the modeled transect is unknown. Therefore, we used all the ages. The distribution of the ages used in the modeling is shown in Figure S1 in Supporting Information S1. Some of the reported MsAr ages have much smaller uncertainties than other dating systems. Because we are focused on the current geometry and kinematics of the MHT and the small uncertainties of the potential outliers of the 9–10 Ma MsAr ages close to the PT2-N may mislead the inversion process, we change the uncertainties of the MsAr ages younger than 9–0.5 Ma and the uncertainties of the MsAr ages older than 9–1.0 Ma when conducting inversion modeling. With these changes, the inversion does not over-value the MsAr ages, which are usually much older

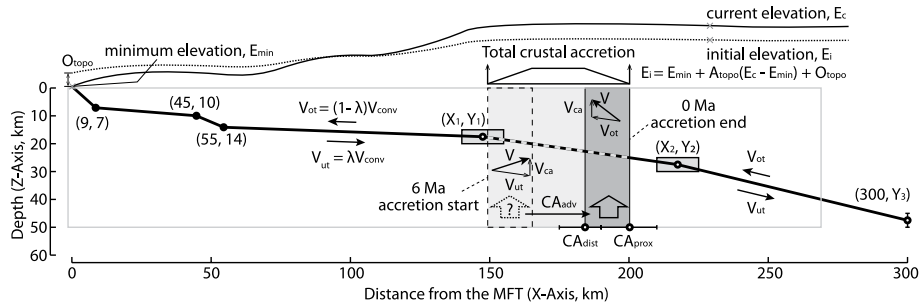

Figure 5. Illustration shows the thermokinematic model boundary conditions and parameters. The kinematic model has the convergence rate (V_{conv}) partitioned on either side of the megathrust into upper plate overthrusting component (V_{ot}) and lower plate underthrusting component (V_{ut}) using a partitioning factor (λ). The geometry of the megathrust is defined using a series of points along its length and the inverted free points, such as (X_1, Y_1), (X_2, Y_2), and (300, Y_3), may occupy any position within each search box or on the error bar. Crustal accretion is carried out by adding a vertical uplift component (V_{ca}) to the velocity field within the range defined by two distance coordinates (CA_{dist} and CA_{prox}). The range can advect from a position represented by dash box hinterland-ward to the present position defined by CA_{dist} and CA_{prox} in the past 6 Ma at an advection velocity of CA_{adv}. The effect of topographic evolution is simulated by assuming a linear evolution from a synthetic initial topography (E_i) to the current topography (E_c). The synthetic initial topography is made by compressing the relief of current topography (E_c-E_{min}) using an amplification factor (A_{topo}) and vertically moving the compressed topography by O_{topo}. For details of the model and other parameters refer to the text and Tables 2 and 3.

than the ages of other dating systems. However, we used true uncertainties for all ages in the forward models. The calculated misfit values of the inversion model and forward model are notated as misfit (Φ) and corrected misfit (Φ_{corr}) later.

4.2. Forward Model in Pecube and Model Parameters

Pecube calculates the location and temperature of points in the model using inputs of fault geometry, fault slip rate, flexural isostasy, radiogenic heat production, frictional heat production, and the boundary temperatures at the surface and the bottom of the model. These calculations are repeated at every time step. The time-temperature history for each point is then used to calculate the expected cooling ages for each thermochronologic system, using known kinetic parameters for the system in question.

In Pecube, for a model without a localized zone of enhanced rock uplift, mass transport is parallel to each fault dip panel, and the fault geometries are defined by coordinate pairs (X, Y) defining the locations of fault dip change in a transect parallel with the mass-transport direction. In this study, the X and Y are the horizontal distance from the MFT fault trace and vertical distances below sea level, respectively (Figure 5). The slip rate along the MHT is defined by the convergence rate (V_{conv}) between the hanging wall and footwall and a partitioning factor (λ) partitioning the convergence into hanging-wall overthrusting, $V_o = (1 - \lambda)V_{conv}$, and footwall underthrusting, $V_u = \lambda V_{conv}$, with respect to the MHT (Figure 5). This modified version of Pecube used in this study is the same as that used in Landry et al. (2016), and it deals with the change in the velocity in the hanging wall between different dip panels using a kink-band style fault kinematics described by Suppe (1983)—the velocity vectors change across the calculated planes bisecting the angle between any two adjacent fault dip panels, rather than using the velocity averaging approach in the original version. The other modification of the software incorporates a localized zone of enhanced rock uplift, similar to the version used in Herman et al. (2010). It simplifies the effect of localized crustal accretion by adding an extra vertical velocity component (V_{CA}) within the region defined by two specified distances (CA_{dist} and CA_{prox} for the southern and northern points, respectively, in this study) from the fault trace, MFT (Figure 5). Rather than using the strategy that applies an enhanced uplift zone at a constant location with respect to the topography in the simulations conducted by Herman et al. (2010) and Landry et al. (2016), we apply a narrower enhanced uplift zone and make it translate hinterland-ward at an advection rate (CA_{adv}) to its present location which is defined by CA_{dist} and CA_{prox} in a certain amount of time (CA_T) to simulate one cycle of accretion (Figure 5). Our strategy is more consistent with the kinematics for the generation of a new horse in a duplex, i.e., a newly generated ramp underthrusts beneath the slice of rock in the hanging wall of the new ramp. The total uplift caused by the enhanced uplift zone in one cycle of crustal accretion on a cross-section is an isosceles trapezoid (Figure 5), which is more consistent with geometry of a horse than the rectangle-shaped

uplift generated by an enhanced uplift zone at a constant location. We only simulate the last cycle of accretion and set $CA_T = 6$ Ma to test the thermal effects since the specific kinematics of the entire multicycle accretion process in the midlower crust is unknown. The time span of one cycle of accretion is also unknown but we consider 6 Ma to be reasonable compared with the balanced cross-section coupled with thermokinematic modeling study in central Nepal Himalaya, the inversion result of the time span of the last accretion below the LHS duplex in northwestern Himalaya, and the geodynamic simulation of the crustal accretion in Himalaya (Ghoshal et al., 2020; Mercier et al., 2017; Stübner et al., 2018). We enable fault translation in all the models to simulate lateral advection of the model topography, such that all samples can translate laterally with respect to the fault but only move vertically relative to the topography.

The dynamic thermal field of the model is calculated using an iterative solution to the finite-element formulation of the 3-D thermal advection-diffusion equation (Braun et al., 2012)

$$\rho c\left(\frac{\partial T}{\partial t} + V\nabla \mathrm{T}\right) = \mathrm{k}\nabla^2\mathrm{T} + \mathrm{H}$$

where ρ is density, c is heat capacity, T is temperature, t is time, V is the velocity, k is thermal conductivity, and H is volumetric radiogenic heat production (for units and symbols, see Table 2). In our models, the temperature at the base of the model is set at 750 °C and does not change over time. Surface temperature decreases with elevation at an atmospheric lapse rate of 6 °C/km from 25 °C at 0 km. Thermal diffusivity is 35.0 km^2/Ma. The bottom of each model is 50 km below the lowest point of the modeled area. Although we only use ages younger than 16 Ma, we run the models from 20 Ma to allow the samples in the model to accumulate enough displacement to be thermally reset at the beginning and to help the model obtain a natural, kinematic-affected thermal field at 16 Ma. The default age of thermally unreset rocks in the model is 20 Ma.

Previous studies dispute whether the Himalayan orogen had a similar topography in the Miocene to the present in high Himalaya (e.g., Carrapa et al., 2016; Gébelin et al., 2013; Masek et al., 1994; McDermott et al., 2013; Wang et al., 2010). Moreover, recent geomorphologic analysis in the Dolpo area suggests that glacial and fluvial erosion along with tectonics have significantly reshaped the extent of the orogenic plateau (Buceta et al., 2020). Therefore, we incorporate the effect of evolving topography in one inversion. Instead of coupling Pecube with a landscape evolution modeling software, as Herman et al. (2010) did, we simply assume an initial topography of the same shape but different relief and minimum elevation than the present topography, and assume a linear evolution from the initial topography over time (Figure 5). To make a synthetic initial topography, the software first keeps the elevation of the lowest point (E_{min}) in the current topography unchanged and linearly compresses the current topography by an amplification factor (A_{topo}). This compression changes the elevation of any point on the surface from the current elevation to $E_{min} + A_{topo}(E_c - E_{min})$. The software then vertically moves the compressed topography by an offset distance (O_{topo}). This results in a synthetic initial topography, in which every point has an initial elevation, $E_i = E_{min} + A_{topo}(E_c - E_{min}) + O_{topo}$.

In models with evolving topography, flexural isostasy is enabled to compute the effect of isostatic adjustment due to evolving topography. The algorithm deals with the subducting plate as a thin elastic plate. We use 25.0 km for the effective elastic thickness of the Indian plate based on the reported Bouguer gravity anomaly data (Berthet et al., 2013; Jordan & Watts, 2005). We use 2,700 and 3,200 kg/m^3 for crustal and upper mantle density, respectively. Young's modulus (E) is 100 GPa and Poisson's ratio (ν) is 0.25 in the models.

We designed three inversions to simulate exhumation: (a) exhumation caused by the flat-ramp geometry of the MHT with a steady-state topography ("ramp model," WNP01); (b) exhumation caused by both the flat-ramp geometry of the MHT and localized enhanced crustal accretion with a steady-state topography ("ramp + duplex model," WNP02); (c) exhumation caused by both the flat-ramp geometry of the MHT and localized enhanced crustal accretion, and affected by the evolving topography ("ramp + duplex + evolving topography model," WNP03). We did not design a model for the out-of-sequence thrusting hypothesis, but discuss it based on our modeling results. All models have a dimension of 255 km × 122 km × 50 km. The topography data are down sampled to a resolution of approximately 900 m. To save computing time, we used varying node spacing at different depths in the models; 0.9 km spacing for the upper 0–5 km, 2.7 km spacing for the 5–15 km part, and 8.1 km spacing for the 15–50 km part. For a list of the model parameters, including their values, units, symbols, and important references, refer to Table 2. We use the inversion algorithm of Pecube to invert for parameters specifically characterizing the three tectonic scenarios. For the MHT geometry in scenarios WNP01 and WNP02,

Table 2
Parameters of Pecube Models[a]

Parameter name	Parameter range	Units	Parameter symbol	Reference
Material properties				
Thermal conductivity	2.5	W/m/K	k	Whipp et al. (2007)
Specific heat capacity	800	J/kg/K	c	Whipp et al. (2007)
Crusal density	2,700	kg/m^3	ρc	
Upper mantle density	3,200	kg/m^3	ρm	
Thermal diffusivity	35.0	km^2/Ma	α	
Volumetric radiogenic heat production	**1.0–1.7**	μW/m^3	H	
Radiogenic heat production	**15–25**	°C/Ma	A	
Effective elastic thickness of the India plate	25.0	km		Jordan and Watts (2005)
				Berthet et al. (2013)
Young's modulus	100.0	GPa	E	
Poisson's ratio	0.3	n/a	ν	
Pecube model parameters				
Mean annual surface temperature in the foreland	25.0	°C	T_s	
Atmospheric lapse rate	6	°C/km	L	Naito et al. (2006)
Basal temperature	750	°C	Tb	
India-Eurasia convergence rate	**Variable**	mm/yr	V_{conv}	Bilham et al. (1997)
				Jouanne et al. (1999)
				Larson et al. (1999)
Convergence partitioning	**0.5–0.7**	n/a	λ	
Model time step	Optimal	years		
Horizontal node spacing	0.9	km		
Vertical node spacing (0–5 km)	0.9	km		
Vertical node spacing (5–15 km)	2.7	km		
Vertical node spacing (15–50 km)	8.1	km		
Model domain	255 × 122 × 50	km		
Fault geometry	**Variable**	km	(X_n, Y_n)	
Crustal accretion (south boundary)	**Variable**	km	CA_{dist}	
Crustal accretion (north boundary)	**Variable**	km	CA_{prox}	
Crustal accretion vertical rate	**Variable**	mm/yr	V_{ca}	
Crustal accretion window advection rate	**Variable**	mm/yr	CA_{adv}	
Amplification factor for evolving topography	**Variable**	n/a	A_{topo}	
Offset factor for evolving topography	**Variable**	km	O_{topo}	

[a]The bold entries indicate the free parameters that were inverted for in the simulations.

because we focus on the exhumation caused by the deep structures in the hinterland of the wedge, we only invert for the coordinates of the northernmost three nodes among the nodes defining the geometry of the MHT, notated as (X_1, Y_1), (X_2, Y_2), and (X_3, Y_3) (Figure 5). For the northernmost dip panel of the MHT, we only invert for Y_3 in the models and set X_3 = 300 km to find a proper dip angle. For all other nodes to the south of these three nodes, primarily defining the upper-crustal flat, the southern small ramp, and the MFT, we set their coordinates based on seismic images, balanced cross-sections, and microseismicity, and do not invert for them. Previous studies suggest that the basal temperature and radiogenic heat production are correlated and can compensate each other to some extent. Because we define the basal temperature at 750 °C, we invert for the radiogenic heat production, A (in °C/Ma). We also inverted for the convergence rate and partitioning factor for several reasons: (a) current

Table 3
Inversion Results[a]

	Inversion name		
	WNP01	WNP02	WNP03
Number of models	22,220	28,820	28,820
Φ/Φ_{corr}	0.26/0.78	0.22/0.55	0.22/0.55
A_{topo}	n/a	n/a	**0.96** (0.5:1.0)
O_{topo} (km)	n/a	n/a	**0.14** (0.0:2.0)
Tb (°C)	750	750	750
A (°C/Ma)	**24.9** (15:25)	**24.9** (15:25)	**24.6** (15:25)
Y_3 (km)	**49.9** (45:50)	**48.5** (45:50)	50
Y_2 (km)	**25.0** (25:30)	**25.4** (25:30)	**25.9** (25:30)
X_2 (km)	**220.3** (215:230)	**224.6** (210:225)	**224.5** (210:225)
Y_1 (km)	**15.2** (15:20)	**15.2** (15:20)	15
X_1 (km)	**167.3** (160:175)	**149.2** (140:155)	**147.2** (140:155)
V_{conv} (mm/yr)	**17.1** (15:20)	**15.5** (14:20)	**14.5** (14:20)
λ	**0.52** (0.5:0.7)	**0.52** (0.5:0.7)	**0.50** (0.5:0.7)
V_{ca} (mm/yr)	n/a	**4.0** (3.0:6.0)	**5.0** (3.0:6.0)
CA_{dist} (km)	n/a	**189.0** (175:190)	**189.3** (175:190)
CA_{prox} (km)	n/a	**203.2** (190:210)	**203.3** (190:210)
CA_{adv} (mm/yr)	n/a	**5.2** (4.0:6.0)	**5.2** (4.0:6.0)

[a]Values in brackets indicate the investigated range of the free parameters and values in bold indicate lowest misfit values for each parameter.

GPS data suggests convergence rate is in a wide range of 14–21 mm/yr; (b) the convergence rate and the partitioning between overthrusting and underthrusting over the past 20 Ma are not well known; (c) internal shortening within the upper plate is not simulated in the simplified models, which may cause inconsistency between the models and the real-world geology even if using the correct values. For scenario WNP02, we also invert for the four parameters defining the crustal accretion (CA_{dist}, CA_{prox}, CA_{adv}, and V_{CA}). The inverted parameters for scenario WNP03 are slightly different from scenario 2: (a) We invert for the two parameters defining the evolving topography, A_{topo} and O_{topo}; (b) to reduce the dimension of the parameter space, we set the Y_1 and Y_3 as constants respectively based on the inversion result of scenario WNP02. Table 3 shows the parameter values and the ranges of the values used in each inversion set.

4.3. Inversion Algorithm: Neighborhood Algorithm

When combined with the Neighborhood Algorithm (NA; Sambridge, 1999a, 1999b; Rickwood & Sambridge, 2006), Pecube can perform inversion modeling that searches for a combination of parameters depicting a forward model that predicts cooling ages consistent with the observed ages. The algorithm searches within the multidimensional parameter space defined by given ranges of free parameters.

The NA deals with the inversion in two stages. In the first stage, the software selects the first set of forward models by randomly selecting parameters from their defined ranges and uses the selected parameters to divide the model parameter space into Voronoi cells (Sambridge, 1999a). The parameters for subsequent forward models are selected from within the subset of Voronoi cells with a low misfit (Φ) to the observed ages. During the inversion, each subsequent forward model is selected from 80% to 85% (resampling ratio, varies with different scenarios) of the current Voronoi cells with the lowest misfits.

The second stage of the NA is an appraisal of the search results to define statistical limits on the ranges of input parameters that provide a good fit to the observed age data (Sambridge, 1999b). Bayesian inference is used to produce posterior probability density functions (PPDFs) for each model parameter using a likelihood function L

$$L = \exp\left(-\frac{n}{2}\sqrt{\sum_{i=1}^{n}\frac{(PredAge_i - ObsAge_i)^2}{{\sigma_i}^2}}\right)$$

The appraisal yields 1D and 2D PPDFs for the model parameters that are presented for each set of model parameters.

5. Modeling Results

For the three inversion sets presented below (Figures 6–8), the parameter ranges are determined based on multiple trials. To evaluate the defined ranges of the inverted parameters in each trial, we use reasonably small ranges of parameters and compute >20,000 forward models in each inversion. If the inversion converges at the end of the defined ranges for many inverted parameters, we change the ranges of the corresponding parameters in the subsequent inversion trial. In each trial, the selection of parameter ranges should agree with our first-order understanding of geology. Therefore, although some best-fit parameters in the presented inversions below are at the end of the selected ranges, we do not further extend the ranges. A summary of the parameter ranges of the presented inversions, parameter values of the best-fit model in each inversion, and the misfit value of the best-fit model for the presented inversion for each scenario is shown in Table 3. Figure S2 in Supporting Information S1 shows the

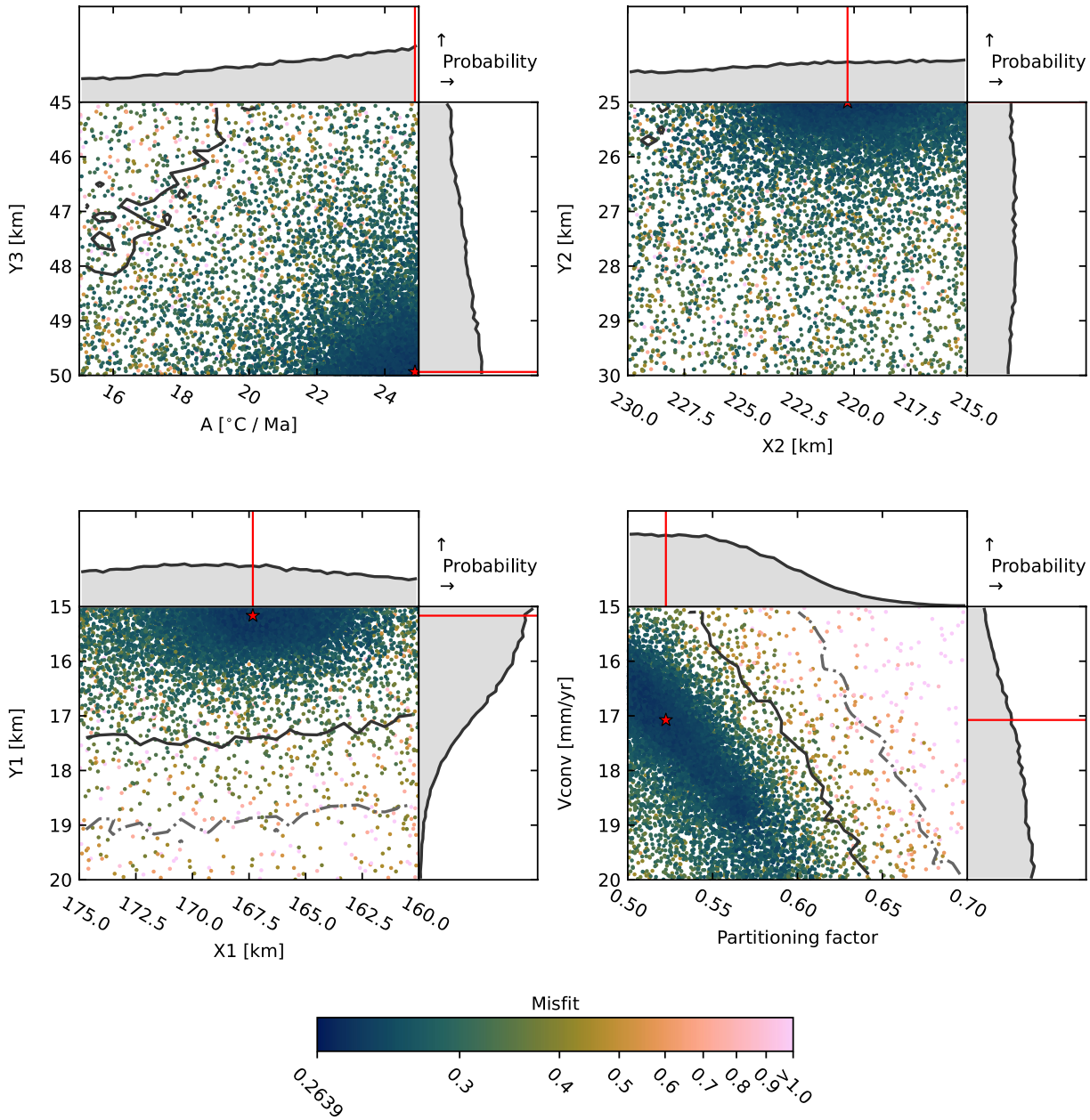

Figure 6. Inversion results of model WNP01 solving for eight free parameters (see Table 3) with Y_3 versus A, Y_2 versus X_2, Y_1 versus X_1, and V_{conv} versus λ. Each dot represents a single forward model, and its color corresponds to the goodness-of-fit to the data. The red star represents the parameter values obtained from the forward model with the lowest misfit. One-dimensional posterior probability density functions (1D PPDFs) derived from the NA appraisal are shown adjacent to the axes for each parameter. The red lines indicate parameter values for the lowest misfit forward model. Two-dimensional PPDFs (2D PPDFs) are represented by lines overlying the scatter diagram where the solid black line is the 1σ confidence interval and the dashed line is the 2σ confidence interval.

correlations between free parameters for the three inversions. As introduced above, we use synthetic errors for some ages in the inversion and calculate the corresponding misfit, Φ. We then select the best model found in each inversion and calculate the corrected misfit, Φ_{corr}, using true errors of all ages.

5.1. Inversion Set WNP01: Slip on the MHT With Steady-State Topography

The models in the inversion set WNP01 simulate a scenario where exhumation is caused only by slip along the MHT with steady topography (ramp model). The inversion set comprises 22,220 forward models. Using a

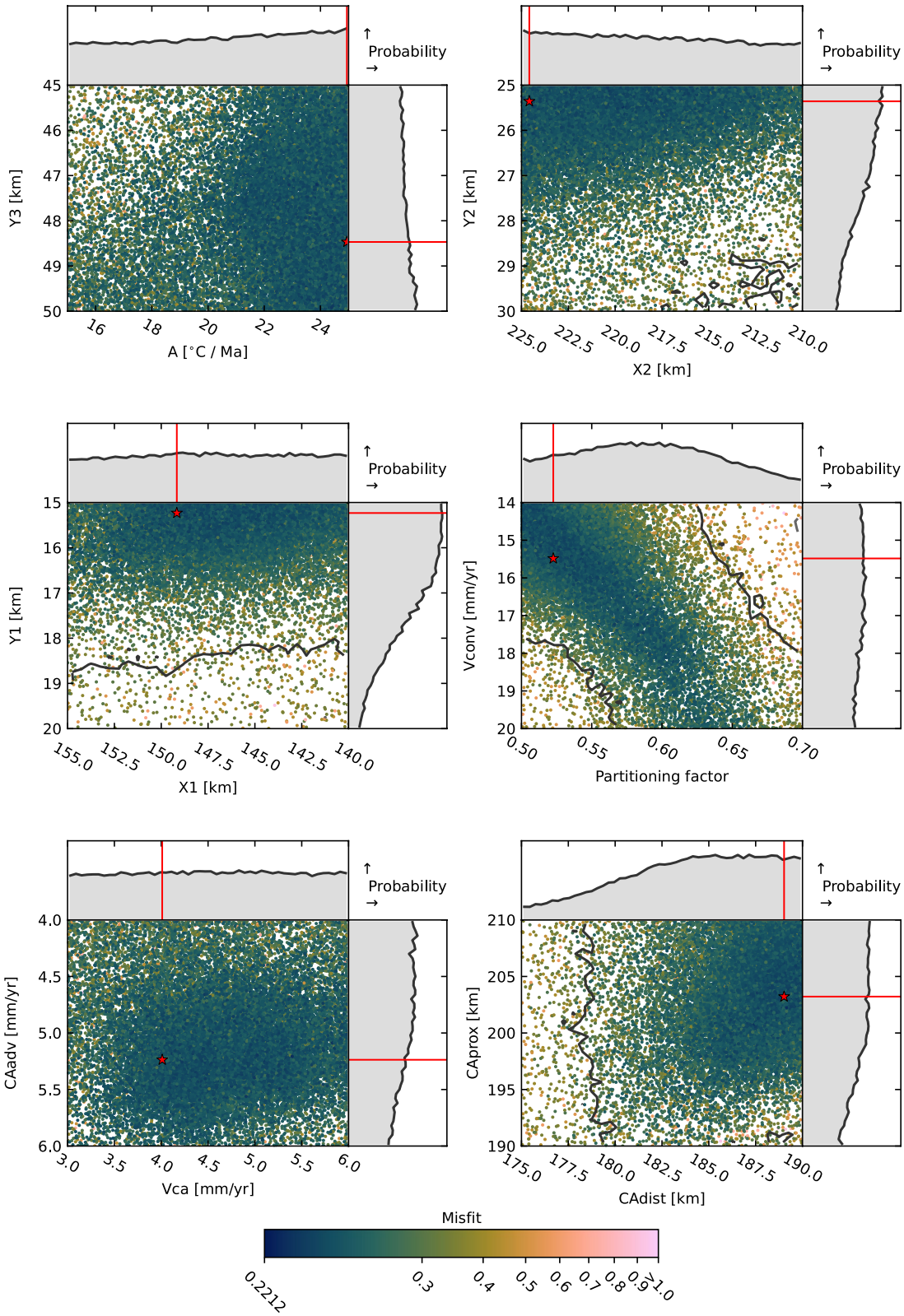

Figure 7. Inversion results for model WNP02 solving for 12 parameters (see Table 3) with Y_3 versus A, Y_2 versus X_2, Y_1 versus X_1, V_{conv} versus λ, CA_{adv} versus V_{ca}, and CA_{prox} versus CA_{dist}. Symbols are the same as for Figure 6.

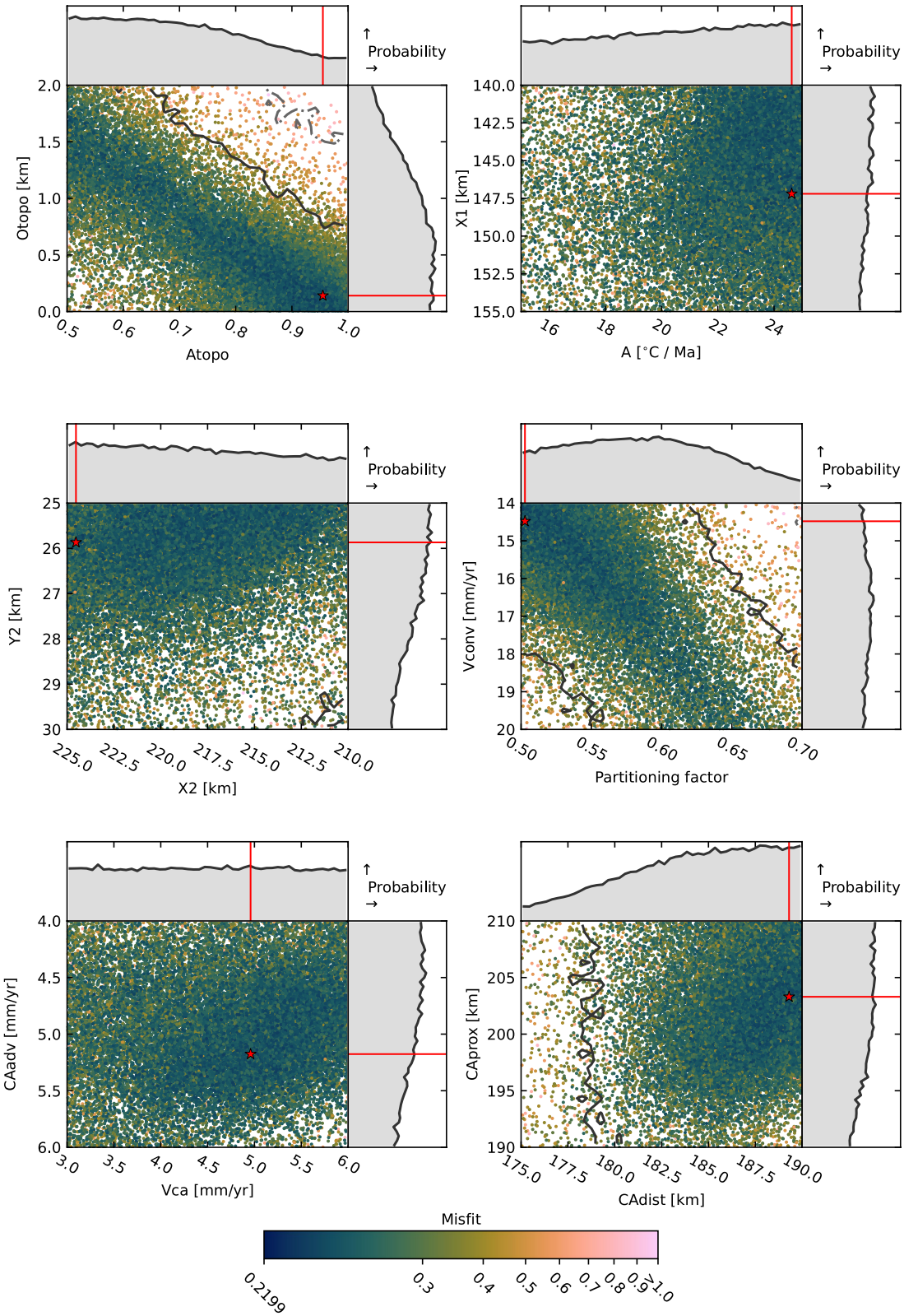

Figure 8. Inversion results for model WNP03 solving for 12 parameters (see Table 3) with O_{topo} versus A_{topo}, X_1 versus A, Y_2 versus X_2, V_{conv} versus λ, CA_{adv} versus V_{ca}, and CA_{prox} versus CA_{dist}. Symbols are the same as for Figure 6.

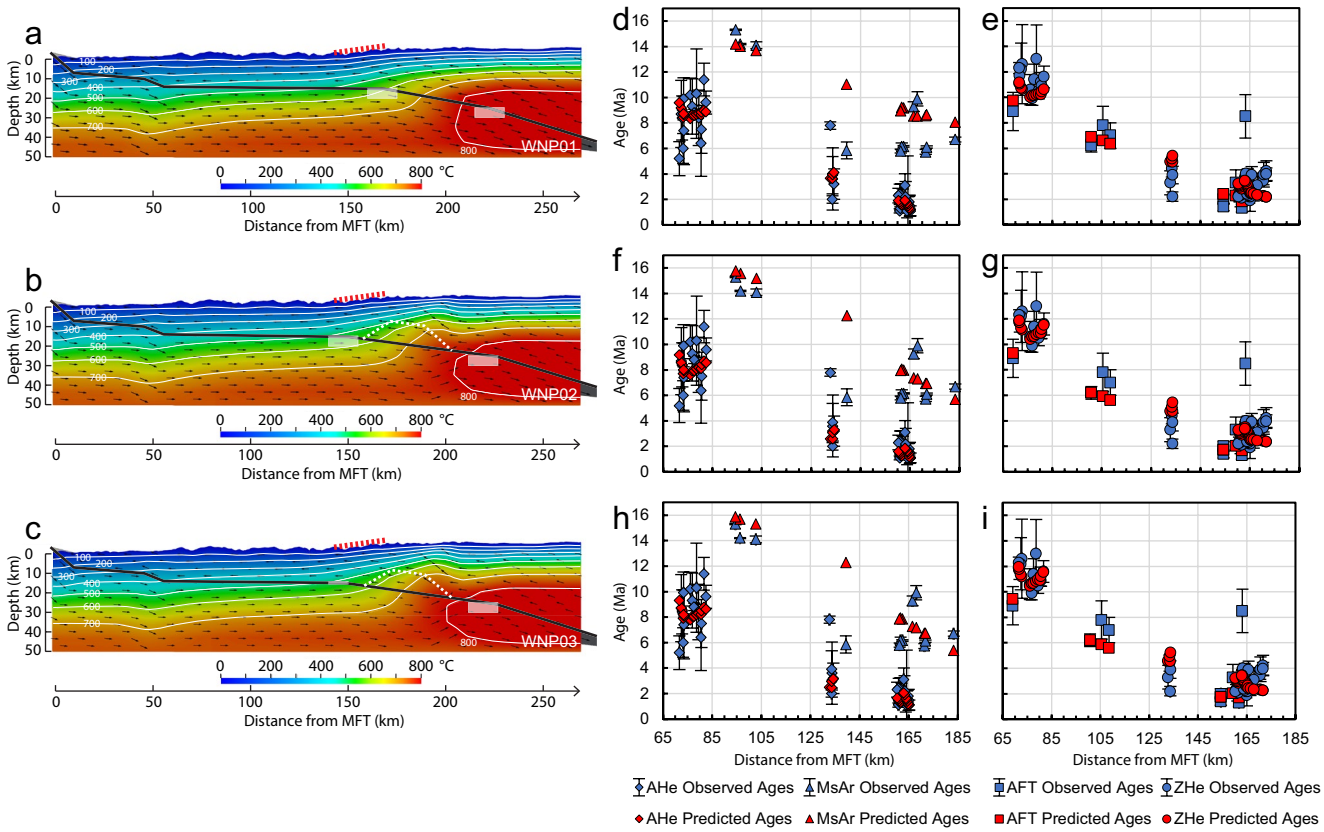

Figure 9. Thermal structures of the best-fit models of the three modeled scenarios (a–c) and comparison between the predicted and observed cooling ages for each model (d–i). White dash lines show the amount and location of the crustal accretion along the megathrust. The red dash lines show the high-slope zone on the topography. Black arrows show a present snapshot of the velocity field for each model. White transparent blocks and bars show the ranges of free parameters for midlower crustal ramp in the inversion models.

resampling ratio of 85%, the inversion reaches a misfit $\Phi < 0.3$ after approximately 8,000 models. For the best-fit model, the misfit is $\Phi = 0.26$ and the corrected misfit $\Phi_{corr} = 0.78$.

The inversion result indicates that the model misfit in this scenario is sensitive to the fault geometry (Figure 6). Parameters for the distance between the midlower crustal ramp and the MFT (X_1 and X_2) have the lowest misfit in the central part of their given ranges. The depths of the inverted nodes of the fault in low-misfit models suggest a shallow midcrustal ramp indicated by the low Y_1 and Y_2 and a steep hinterland sector indicated by the large Y_3 (Figure 9). The best-fit model has a midcrustal ramp starting from 167.3 to 220.3 km from the MFT and dipping at 10.5° (Figure S3 in Supporting Information S1). The hinterland sector of the MHT in the best-fit model has a dip of 17.4°. These three depth parameters have best-fit values at the ends of the given ranges in the inversion, but we did not test new ranges because these parameter ranges are consistent with other geophysical and geologic data. The convergence rate and partitioning factor for low-misfit models are correlated in a narrow zone on the 2D PPDF plot (Figure 6), suggesting that the misfit is very sensitive to the slip rate along the MHT at the first order, but the effect of convergence and the partitioning between the underthrusting and overthrusting can compensate each other to some extent. The best-fit model has a convergence rate of 17.1 mm/yr, with 52% of it accommodated by footwall underthrusting. Both values are reasonable compared with previous studies (Bilham et al., 1997; Coutand et al., 2014; Jouanne et al., 1999; Landry et al., 2016; Larson et al., 1999). Because we used a constant temperature at the bottom of the model, we inverted for the heat production over a wide range, 15–25 °C/Ma, and the inversion finds the best-fit value at the high end of the range.

The comparison between the predicted ages of the best-fit model in this inversion set and the observed ages is shown in Figure 9. Some ages not used in the inversion or misfit calculation are also included in the plot. Generally, for the low-temperature-system ages used in the inversion, including AHe, ZHe, and AFT ages, most

predicted ages match the observed ages within 1 standard uncertainty. Age clusters of AHe and ZHe between 29.5°N and 29.6°N (132–135 km from the MFT) are not used in the inversion; they have a worse match than the ages used in the inversion. Among the four ZHe and four AHe ages in the cluster, only two predicted AHe ages overlap with the observed ages within 1 standard uncertainty, but the discrepancy is usually within 2 standard uncertainties. For the MsAr ages, there is a large discrepancy between the predicted and observed ages for rocks in the hinterland close to the PT2-N. Among the two previously introduced groups of MsAr ages close to the high-slope zone, the predicted ages are closer to the group of 9–10 Ma data than the ca. 6 Ma ages. However, ages of ca. 6 Ma or younger are common along the high-slope zone in other segments of the Himalaya. For example, one MsAr age of 5.85 ± 0.67 Ma is reported at 29.73°N (139 km from the MFT) in this region (Mercier, 2014), close to the high-slope zone to the west of the modeled profile across a proposed lateral ramp in the MHT (Figure 4). Thus, we interpret that this model fails to produce MsAr ages consistent with observation close to the high-slope zone. The predicted MsAr ages of the samples from the southernmost part of the model are consistent with the observed ages (age difference <1 Ma).

5.2. Inversion Set WNP02: Slip on the MHT and Localized Enhanced Rock Uplift at Steady Topography

The models in the inversion set WNP02 simulate a scenario where exhumation is caused by a combination of slip along the MHT and localized enhanced uplift by crustal accretion with steady topography (ramp + duplex model). The inversion set comprises 28,820 forward models (Figure 7). Using a resampling ratio of 80%, most models in the inversion reach a misfit $\Phi < 0.35$ after approximately 2,000 models. For the best-fit model, the misfit is $\Phi = 0.22$ and the corrected misfit $\Phi_{corr} = 0.55$.

Similar to the inversion set WNP01, the misfit values are sensitive to the convergence rate and underthrusting-overthrusting partitioning factor as suggested by the strongly correlated pattern for the low-misfit forward models on the 2D PPDF plot (Figure 7). The best-fit model in this set has a convergence rate of 15.5 mm/yr with 0.52% of it accommodated by underthrusting. Both values are broadly consistent with previous studies (Bilham et al., 1997; Coutand et al., 2014; Jouanne et al., 1999; Landry et al., 2016; Larson et al., 1999). Parameters for the locations of distal and proximal ends of the crustal accretion zone and the rates of localized enhanced uplift and accretion-zone advection have a best-fit combination in the central part of the 2D PPDF plot. But these four parameters for crustal accretion have a complex correlation with each other (Figure S2 in Supporting Information S1), which may result in the flat 1D PPDFs of V_{ca} and V_{adv}. The lack of age constraints in the inversion for the northernmost area may also cause flat PPDFs. The best-fit mode has a localized enhanced uplifting zone translated at a rate of 5.2 mm/yr to its present location at 189.0–203.2 km from the MFT with a vertical crustal accretion rate of 4.01 mm/yr. Due to the existence of an enhanced uplift zone close to the high-slope zone in the model, the dip of the northernmost sector of the MHT, different from the inversion set WNP01, has more freedom in this inversion as suggested by the diffuse distribution of the Y_3 values of low-misfit models (Figure 7). This suggests that the existence and kinematics of a crustal accretion zone play a more determining role than the dip of the hinterland sector of the MHT. In this inversion, the best-fit mode has a midcrustal ramp starting from 149.2 to 224.6 km from the MFT and dipping at 7.6° (Figure 9 and Figure S3 in Supporting Information S1). The hinterland sector of the MHT in the best-fit model has a dip of 17.0°. The inversion of the heat production parameter also finds the best-fit value at the high end of the given range, with a best-fit value of 24.9 °C/Ma.

The comparison between the estimated ages in the best-fit model and the observed ages is shown in Figure 9. Similar to the best-fit model in WNP01 inversion, for the low-temperature systems, the estimated ages also can generally match the observed ages, including the ages not used in the inversion. The large decrease in corrected misfit of the best-fit model compared with the one in WNP01 is mainly contributed by a significantly improved fit for the data cluster close to the high-slope zone (160–185 km). The differences between the observed MsAr ages and predicted ages there are mostly <2 Ma. The estimated MsAr ages are younger than the estimation in the best-fit model of the WNP01 inversion, and therefore are more consistent with the young MsAr ages (as young as <5 Ma) close to the high-slope zone along-strike in other segments (e.g., Copeland et al., 1991; Gibson et al., 2016; Huntington & Hodges, 2006; Martin et al., 2015). The estimated MsAr ages of the samples from the southernmost part of the model also have a good fit with the observed ages (age difference <1.5 Ma). We interpret that this model is overall successful in producing ages consistent with the observed ages for all age systems discussed.

5.3. Inversion Set WNP03: Slip on the MHT, Localized Enhanced Rock Uplift, and Evolving Topography

The models for inversion set WNP03 simulate a scenario similar to WNP02 except that it has a dynamically evolving topography (ramp + duplex + evolving topography model). Because of the introduction of two parameters defining the evolving topography, to keep the number of parameter-space dimensions unchanged, we use constant values for the vertical coordinates of the hinterland most node of the MHT ($Y_3 = 50.0$ km) and the upper end of the ramp ($Y_1 = 15.0$ km). The value of Y_1 is selected based on the consistent Y_1 values of the best models in the inversion sets WNP01 and WNP02. We also change Y_3 to a constant parameter because the inversion result of WNP02 shows, when crustal accretion is incorporated, Y_3 cannot be well-constrained. This inversion set comprises 28,820 forward models. Using a resampling ratio of 80%, the inversion has a worse convergence than the WNP02 inversion set, but it still reaches a misfit $\Phi < 0.35$ after approximately 28,000 models. The lowest misfit is $\Phi = 0.22$, and the corrected misfit $\Phi_{corr} = 0.55$.

The inversion result is similar to WNP02 in relatively less well-constrained fault-bend locations than WNP01 (related parameters X_1, X_2, Y_2), highly correlated convergence rate (V_{conv}) and underthrusting-overthrusting partitioning factor (λ), correlated crustal accretion parameters, including distal and proximal ends of the crustal accretion zone and uplift rate (CA_{dist} and CA_{prox}) and uplift rate and advection velocity of the crustal accretion zone (V_{CA} and CA_{adv}) (Figure 8). The introduction of inversion for evolving topography makes the distribution of good-fit X_1, X_2, and Y_2 more diffuse than the result of WNP02 in their 2D PPDF plots. The best-fit model has a convergence rate of 14.5 mm/yr with 50% of it accommodated by underthrusting Both of these values are broadly consistent with previous studies (Bilham et al., 1997; Coutand et al., 2014; Jouanne et al., 1999; Landry et al., 2016; Larson et al., 1999). The best-fit geometry and kinematics of the MHT, including crustal accretion, are approximately similar to the best model of WNP02. The best-fit MHT has a shallow-dipping middle crustal ramp of an 8.0° dip (Figure S3 in Supporting Information S1), starting from 147.2 to 224.5 km from the MFT (Figure 9), and a hinterland sector of 17.7°. The best-fit mode has a localized enhanced uplift zone translated at a rate of 5.2 mm/yr to its present location at 189.3–203.3 km from the MFT with a vertical crustal accretion rate of 5.00 mm/yr during the last 6 Ma in the model. The best-fit heat production parameter is 24.6 °C/Ma. The parameters defining the initial topography, A_{topo} and O_{topo}, are also well correlated in a narrow zone on the 2D PPDF plot. The best-fit A_{topo} and O_{topo} are 0.96 and 0.14 km, indicating no significant topographic evolution in the best-fit model.

Between the inversion sets WNP02 and WNP03, the parameters of the best-fit models are not significantly different, and they have the same level of observation-prediction fit (Figure 9). The pattern in the estimated ages is similar to that of the best-fit model in WNP02. We conclude that this model is overall successful in producing ages consistent with the observed ages for all age systems discussed and that whether the topography significantly evolved over time cannot be determined with the methods used in this study.

5.4. Limits and Uncertainties of the Models

Our 3D thermokinematic models invoke complex factors for which one-dimensional thermal modeling cannot account. However, the complexity, as reflected by 8 or 12 free parameters in the inversions, also induces uncertainties in the inversion results. The confidence intervals of some parameters are not plotted in the 2D PPDFs because they are comparative to the given parameter ranges, as suggested by their relatively flat 1D PPDFs plots. One reason for those flat 1D PPDFs can be the complex correlations between the large numbers of free parameters (Figure S2 in Supporting Information S1). To investigate the effect of each parameter needs systematical experiments and is beyond the goal of this work. The extent of convergence can also be limited by the number of forward models in each inversion. To reach a certain extent of convergence, an increase in the number of dimensions of the free parameter space requires a significant increase in the number of forward models. However, we do not continue the inversions because each inversion found many low-misfit (misfit <0.3) models. These low-misfit (<0.3) models plot in a large portion of the free parameter spaces in all three inversions, indicating that the selected parameter ranges are reasonable. We used very narrow parameter ranges to speed up the inversion convergence, which may also cause the apparent bad convergence. Moreover, the uneven distribution of the cooling ages used to inform the inversion may also affect the inversion convergence. The lack of data coverage in the northern end of the area (>185 km from the MFT) may lead to bad constraints on the geometry and kinematics of the northern end of the transect. We also point out that the model design simplifies geologic processes, and we cannot preclude that an inversion with a different model design may find models of a lower misfit.

Despite the apparent bad convergence and limits of the inversions, we do not expand our inversions by changing model designs, increasing the number of forward models in each inversion, or expanding free-parameter ranges, mainly for several reasons. Frist, the first-order model design, including parameter-range selection, is based on the conceptual models suggested by various independent studies and data (e.g., Fan & Murphy, 2021; Harvey et al., 2015; Hubbard et al., 2016; van der Beek et al., 2016). The ultimate goal of inversions is to evaluate the conceptual models, which is ultimately based on comparing low-misfit-model predicted ages and observed cooling ages and on assessing existing data from other observations rather than solely on software-reported misfit values. Therefore, we do not intend to use the inversion method to explore baseless model designs and parameter ranges, whatever a low misfit an inversion may reach. Second, the used free-parameter ranges in the inversions are small enough compared with the orogenic-scale models that the apparent large uncertainties within the small parameter ranges do not essentially disprove the first-order conceptual models. The similarity between the best-fit models of inversions WNP02 and WNP03 also indicates the reliability of the inversion.

6. Discussion

6.1. Midlower Crustal Duplex Causing Hinterland Exhumation

Comparing the results of the models with and without the involvement of crustal accretion shows that midlower crustal accretion is required in a model that can produce observation-fitting cooling ages. While each of the three best-fit models can produce good-fit cooling ages of low-temperature systems, only the two best-fit models involving crustal accretion can produce the predicted MsAr ages that fit observations.

Thermokinematic modeling has been used in many studies to test the crustal-accretion model of the exhumation, tectonics, and metamorphism in the Himalayan wedge. Similar work in the central Nepal Himalaya also suggests that a model with crustal accretion along a midcrustal ramp in the MHT can produce good-fit cooling ages of MsAr, ZHe, and AFT (Herman et al., 2010). The other study in the central Nepal Himalaya used a different version of Pecube which can be coupled with detailed kinematics based on balanced cross-sections to assess different structural reconstructions (Ghoshal et al., 2020). They also found that only models involving hinterland-dipping duplexing and the thrusting of the duplex over a midcrustal ramp can produce sufficiently rapid exhumation to produce the observed young MsAr ages as well as low-temperature cooling ages. An equivalent study in Sikkim Himalaya by Landry et al. (2016) did not investigate MsAr ages, but by comparing the model-produced and observed ZHe and AHe ages, they also favor a model with crustal accretion. Equivalent studies in Eastern Bhutan, Kumaun, and Garwhal Himalaya did not test competing kinematic models, but confirmed that models involving crustal accretion can produce observation-fitting cooling ages of various geochronometers including MsAr, ZHe, and AFT (Célérier et al., 2009; Grujic et al., 2020). Similar thermokinematic models also invoked duplexing or complex kinematics requiring matter accretion from the subducting plate to the hanging wall of the MCT to produce both the inverted metamorphic gradient recorded in the rocks across the MCT and the exhumation of the LHS (Bollinger et al., 2004; Grujic et al., 2020; Harrison et al., 1997).

Some studies using other approaches also suggest that crustal accretion is a main mechanism accommodating midlower crustal strain. Within the GHS, thrust-sense tectonic or metamorphic discontinuities have been documented (e.g., Carosi et al., 2016, 2018; Larson et al., 2015; Montomoli et al., 2013, 2015). These discontinuities approximately mimic the PT2 on the map and usually correspond to the areas on the foreland limb of the antiformal crustal accretion in the thermokinematic models discussed above, indicating midlower crustal strain accumulation. Underplating of the material from the Indian plate to the upper plate is supported by isotopic signatures of the high-grade crystalline rocks in the Gurla Mandhata area along the Northern Himalayan antiform (Godin et al., 2021; Murphy, 2007). Direct observation of a crustal-scale duplex structure on seismic-reflection profiles across the Yarlung-Zangbo suture was documented (Gao et al., 2016; Guo et al., 2018) or reinterpreted (Laskowski et al., 2018). The similar inclinations recorded in the GHS and LHS indicated by the secondary remnant magnetization formed during metamorphism contradict MCT ramping and favor the interpretation of duplex structures (Schill et al., 2004). Landscape evolution simulations in the Bhutan and central Nepal Himalaya suggest that crustal accretion at depth can facilitate the in-situ formation of the low-relief landscape and a physiographic transition at the front of it (Adams et al., 2016; Herman et al., 2010). Similarly, Fan and Murphy (2021) proposed that strain accumulation in the midlower crust through duplexing is a mechanism of plateau outward growth based on the observation that the thick high-grade metamorphic core of the orogen correlates well with the high-elevation, low-relief landscape to the north of the present active-uplift front. Grandin et al. (2012)

addressed that the interseismic transient-uplift peak indicated by interferometric synthetic aperture radar data spatially matches the long-term uplift peak indicated by the study on river incision in central Nepal. This pattern requires formation of a new crustal ramp via footwall-to-hanging-wall accretion as the old ramp translated toward the hinterland. Similarly, a steady position of the active uplift with respect to the PT2 since ca. 1.5 Ma in northwestern Himalaya is suggested by the spatial similarity of the long-term (Ma) and short-term (ka) erosion rates, which lead Morell et al. (2017) to draw the same conclusion.

There are two main groups of studies invoking the ramp model without the involvement of crustal accretion to explain observations from a variety of disciplines, but their data usually cannot represent long-term orogen-building processes. The first group used mechanical modeling methods to simulate the deformation depicted by geodetic data within the time span of seismic cycles, but these data record deformation no older than decades (e.g., Berger et al., 2004; Bilham et al., 1997; Cattin & Avouac, 2000; Elliott et al., 2016; Godard et al., 2004; Jackson & Bilham, 1994; Jouanne et al., 1999; Larson et al., 1999). Some of these studies also considered the effects of rheology change and erosion in their models and compared the model predictions with results of erosion and denudation studies which usually do not account for processes older than Quaternary (Cattin & Avouac, 2000; Godard et al., 2004, 2009; Lavé & Avouac, 2001). The other group of studies that support the ramp model conducted thermokinematic modeling similar to this study, but they usually did not test the effect of crustal accretion (Coutand et al., 2014; Robert et al., 2009, 2011). They also used only ages of low-temperature chronometers to test the models which may not be able to determine the feasibility of continuous crustal accretion (this study; Ghoshal et al., 2020; Whipp et al., 2007). Some other studies invoked the ramp model to conceptually explain some geological observations without quantitative test, and therefore do not conflict with the models invoking crustal accretion (e.g., Beaumont, 2004; Molnar, 1984; Ni & Barazangi, 1984; Seeber et al., 1981; van der Beek et al., 2016).

The other competing kinematic model to explain the PT2 and the rapid exhumation along it is the out-of-sequence model (Harrison et al., 1997; Hodges et al., 2004; Thiede et al., 2004, 2005; Whipple et al., 2016; Wobus et al., 2003, 2005, 2006). We did not directly test this model in this study because this model contradicts several independent lines of observations. If an active thrust fault accommodates the hinterland active uplift and maintains the PT2 and rapid exhumation, there should be an abrupt change in the cooling ages across the active fault. However, age profiles along most of the investigated transects do not show an abrupt change, especially for the ages of low-temperature dating systems (e.g., Coutand et al., 2014; Ghoshal et al., 2020; Landry et al., 2016; McQuarrie et al., 2019; Stübner et al., 2018; Thiede & Ehlers, 2013). Although several lines of evidence for active out-of-sequence thrusting or reactivation of the MCT have been reported at several places (e.g., Braden et al., 2018; Catlos et al., 2001; Harrison et al., 1997; Hodges et al., 2004; Thiede et al., 2017; Whipple et al., 2016; Wobus et al., 2003, 2005, 2006), no continuous active thrust fault along the generally orogen-wide continuous (>1,500-km long) PT2 has yet been mapped. Finally, thermokinematic modeling in central Nepal shows that an out-of-sequence model producing observation-fitting exhumation pattern requires either unrealistic fast movement along the thrust fault and the STD or mechanically unfeasible high-dip angle of the thrust fault (Herman et al., 2010).

6.2. 3D Megathrust Ramps

Many studies suggest that the MHT has complex along-strike heterogeneity regarding the dip, location, and number of the fault ramps (Fan & Murphy, 2021; Hauck et al., 1998; Larson et al., 1999; Mugnier et al., 2017; Robert et al., 2011). For the western Nepal Himalaya, different MHT geometries from the central Nepal Himalaya have been proposed based on observations from a variety of disciplines, including structural geology (DeCelles et al., 2020; Hubbard et al., 2016; Robinson et al., 2001), thermochronology (Gibson et al., 2016; van der Beek et al., 2016), metamorphism (Soucy La Roche & Godin, 2019), seismicity (Hoste-Colomer et al., 2018), and landscape analysis (Harvey et al., 2015). However, most of these models are conceptual and are not quantitatively constrained. Some models based on balanced cross-sections focus on the structures primarily to the south of the PT2 and do not deal with the midlower crustal structures or MHT crustal ramps (e.g., DeCelles et al., 2001; Olsen et al., 2019; Robinson, 2008; Robinson et al., 2006; Figure 3). Geophysical data used in interpreting the MHT geometry are usually of poor quality for deep structures in the hinterland (e.g., Caldwell et al., 2013; Subedi et al., 2018). The numerical models in this study provide the first assessment of the MHT hinterland geometry in western Nepal Himalaya based on thermokinematics.

The best models of inversion sets WNP02 and WNP03 are very similar, and we consider both to be the preferred models based on their successful prediction of the calculated cooling ages (Figure 9). The upper-crustal portion of the MHT (shallower than 14 km) are not investigated in this study, and in our model the geometry of this part is adopted from the two-ramp model based on geomorphology, thermochronology, microseismicity, and balanced cross-sections (DeCelles et al., 2001; Harvey et al., 2015; Hoste-Colomer et al., 2018; Olsen et al., 2019; van der Beek et al., 2016). In our preferred models, the upper-crustal ramp connects to a long flat at approximately 14–15-km deep. This flat is imaged as a midcrustal low-velocity zone from receiver function analysis on teleseismic waveforms (Subedi et al., 2018), and its southern extent is consistent with the distribution of microseismicity (Ader et al., 2012; Hoste-Colomer et al., 2018). At about 149 km to the north of the MFT, this midcrustal flat connects to a not-well-expressed midlower crustal ramp, consistent with the northward lack of intense microseismicity as the ramp extends beneath seismogenic depths (Figures 3 and 9). A sector of the low-velocity zone to the north but discontinuous from the midcrustal flat on the receiver function image also agrees with the gently dipping midlower crustal ramp geometry in our preferred models (Figure 3). The crustal accretion in our preferred models is on this midlower crustal ramp, indicating that PT2-N in western Nepal Himalaya represents the active-uplift front of the high Himalaya plateau, which is consistent with previous interpretations (e.g., Cannon & Murphy, 2014; Fan & Murphy, 2021) (will be discussed in the next section) (Figure 9). In our preferred models, the midlower crustal ramp connects to a steeper hinterland ramp at ca. 25-km depth. However, this hinterland ramp should be interpreted cautiously because no data, including cooling ages, is available to test it. It may be a trade-off product of the inversion caused by the limitation of the model design: The northern Himalaya anticline is thought to start its thickening process as early as early-middle Miocene (e.g., Fan & Murphy, 2021; Godin et al., 2006a; Murphy & Copeland, 2005; Murphy et al., 2002) and thus should have thickened via multiple cycles of crustal accretion. However, in the numerical models, we only simulate one accretion cycle. Therefore, the thermal effect of a hot hinterland due to multiple cycles of accretion prior to the simulated last accretion cycle can be compensated by fast exhumation along a steep hinterland ramp in the simulation.

Our preferred models are different from the MHT geometry in the central Nepal Himalaya, which is characterized by one large midlower crustal ramp at approximately 100 km from the MFT. The differences in the number and location of MHT ramps between the western and central Nepal Himalaya require lateral or oblique ramps in the MHT. A 3D conceptual model with a lateral ramp has been invoked to explain the different P-T-t paths of metamorphic rocks from approximately the same structural position but different along-strike segments in western Nepal Himalaya (Soucy La Roche & Godin, 2019). Based on a balanced cross-section in western Nepal and the assumption of an along-strike constant amount of shortening, DeCelles et al. (2020) discussed the 3D evolution of the upper-crustal structures in midwestern Nepal area, but the model does not address the deeper structures in the hinterland. Based on the finding that a balanced cross-section with LHS duplex on a midcrustal ramp can fit well with the MHT geometry revealed by seismic observations from the 2015 M_w 7.8 Gorkha earthquake, Hubbard et al. (2016) assumed the constant kinematics along-strike and proposed a 3D MHT model for the Nepal Himalaya using the axis of the LHS anticlinorium as a proxy of the top of the midlower crustal ramp. Fan and Murphy (2021) synthesized different data sets to propose a 3D evolution model of the MHT in the midwestern Nepal Himalaya and discussed the mechanism of orogenic-wedge growth. Their results support the idea that the inner wedge or the orogenic plateau grows outward through crustal accretion at the bottom of the brittle-ductile transition zone, the location of which is mainly controlled by the geometry, especially the midlower crustal ramp, of the MHT. This hypothesis predicts that the along-strike variation in the location of active-uplift front of the plateau or the high-slope zone is the surface expression of the along-strike variation in MHT geometry.

To assess the conceptual 3D MHT model for the midwestern Nepal Himalaya proposed by Fan and Murphy (2021), we need to discuss three questions: First, is it true that the midlower crustal ramp always controls where the active-uplift front location along the Himalaya? Second, can the high-slope zone represent the active-uplift front of the orogen? Third, which high-slope zone among the two branches in western Nepal Himalaya represents the active-uplift front of that segment?

The northern branch of the high-slope zone where the young cooling ages cluster along the modeled transect is above the upper part of the midlower crustal ramp and the southern limb of the antiformal crustal accretion in our preferred models (Figure 9). Along a transect across the Kathmandu and Annapurna areas, the cooling ages have a similar spatial pattern showing that the youngest age cluster located in the high-slope zone is associated with the rapid exhumation caused by crustal accretion on a midlower crustal ramp in good-fit thermokinematic

models (Ghoshal et al., 2020; Herman et al., 2010). This pattern is not affected by the ca. 60–70 km difference in the distance between the MFT and the ramp or the active-uplift front between the western and central Nepal Himalaya (e.g., Elliott et al., 2016; Ghoshal et al., 2020; Herman et al., 2010; Hubbard et al., 2016; Whipple et al., 2016, and this study). This pattern is also found valid in Kumaun, Annapurna, Sikkim, and Bhutan Himalaya (Célérier et al., 2009; Grujic et al., 2020; Landry et al., 2016; Singer et al., 2017; Whipp et al., 2007). These observations support that the same mechanism may be controlling the tectonomorphology of the whole orogen; the along-strike variation in the active-uplift front location can therefore be interpreted as an indicator of the along-strike heterogeneity in the location of the MHT midlower crustal ramp (Fan & Murphy, 2021). The newly reported ages along the northern Himalaya antiform and the hinge of the Dolpo synform in western Nepal (9.5–12.2 Ma) are older than those along-strike correspondent ages close to the modeled transect. In contrast, the ages to the south of the Dolpo synform, generally along the eastern limb of the topographic embayment in midwestern Nepal, are much younger (3.1–7.4 Ma) and are consistent with the ZHe ages reported along the high-slope zone in other sectors of the orogen (Figure 4). In the Thakkhola graben, published ages also show that the youngest cooling ages are at the high-slope zone, and the ages to the north in the inner wedge are relatively old (Figure 4). Although the southward younging trend of the cooling ages along the footwall of the graben-bounding fault is previously attributed to the southward development of the graben (Brubacher et al., 2020), we here think it is still mainly caused by the southward propagation of the crustal thickening for the following reasons. The cooling ages reported from the footwall of the graben-bounding fault by Brubacher et al. (2020) are very consistent with our new data from the northern Himalaya antiform and the hinge of the Dolpo syncline, far away from the fault. The graben-bounding fault is steep and has only accommodated 2.2 km of wedge-parallel extension (Baltz et al., 2021). Therefore, the graben structure is unlikely to affect the thermal structure of our sampling area. These data support that the active-uplift front of the transitional area along the embayment from far-western Nepal to central Nepal is represented by the northern branch of the high-slope zone (Fan & Murphy, 2021).

The details of the conceptual 3D kinematic evolution of the MHT geometry, including how the MHT coevolved with the orogen morphology, are described in Fan and Murphy (2021). The 3D kinematics of the fold-thrust-belt in the upper-crustal part in this region is also discussed in DeCelles et al. (2020). Below we integrate these discussions with the surface geology and our modeling results to briefly introduce the main along-strike variations in the MHT ramp geometry of our model for the western Nepal Himalaya (Figure 10). Along the transect through the embayment apex, the MHT is characterized by two ramps, among which the midlower crustal ramp is further hinterland-ward than the adjacent segments. The two ramps correlate with PT2-S and PT2-N. In the along-strike adjacent segments, the MHT is characterized by one midcrustal ramp closer to the MFT, and it connects up-dip to a deeper flat than the flat in our modeled transect. Oblique or lateral ramps in the midlower crust accommodate the along-strike changes in the location of the midlower crustal ramps. These oblique or lateral ramps correlate with the abrupt forelandward shift of the MCT and the active-uplift front from the embayment sector to adjacent sectors and with the along-strike transition between antiformal structures (duplex) and synformal structures (klippe or half-klippe). If these lateral ramps started to develop as an older midlower crustal ramp below the northern Himalaya anticline propagated forelandward differently along-strike (Fan & Murphy, 2021), it may have happened at ca. 10 Ma, as suggested by the cooling ages along the northern Himalayan anticline (this study and Brubacher et al., 2020). To the east of the town of Juphal, a small lateral ramp may accommodate the further southward shift of the midlower crustal ramp. This lateral ramp, though is not expressed in the klippe structure to the south, can be correlated with the shift of the LHS-duplex crest, the MCT, the STD, and the active-uplift front. The general trend and major step-overs of the WNFS can be correlated well with the general shape of the midlower crustal ramps and the lateral and oblique ramps in this model, supporting that the WNFS might have developed partly by exploiting the structures at depth (Fan & Murphy, 2021). The present midlower crustal ramp in this model also has a similar pattern to the reconstructed initial upper-crustal frontal ramp producing the LHS duplex reported in DeCelles et al. (2020), supporting that this upper-crustal ramp may initially bifurcate from a once longer midlower crustal ramp (Fan & Murphy, 2021).

6.3. Implications for Orogenic-Wedge Growth

Our thermokinematic models employed a different strategy from previous similar studies in adjacent areas to simulate crustal accretion (e.g., Grujic et al., 2020; Herman et al., 2010; Landry et al., 2016). These previous studies used a wide window of crustal accretion at a constant location in the coordinate of the upper plate. However, the location of crustal accretion may change as the orogenic wedge grows. Crustal accretion or

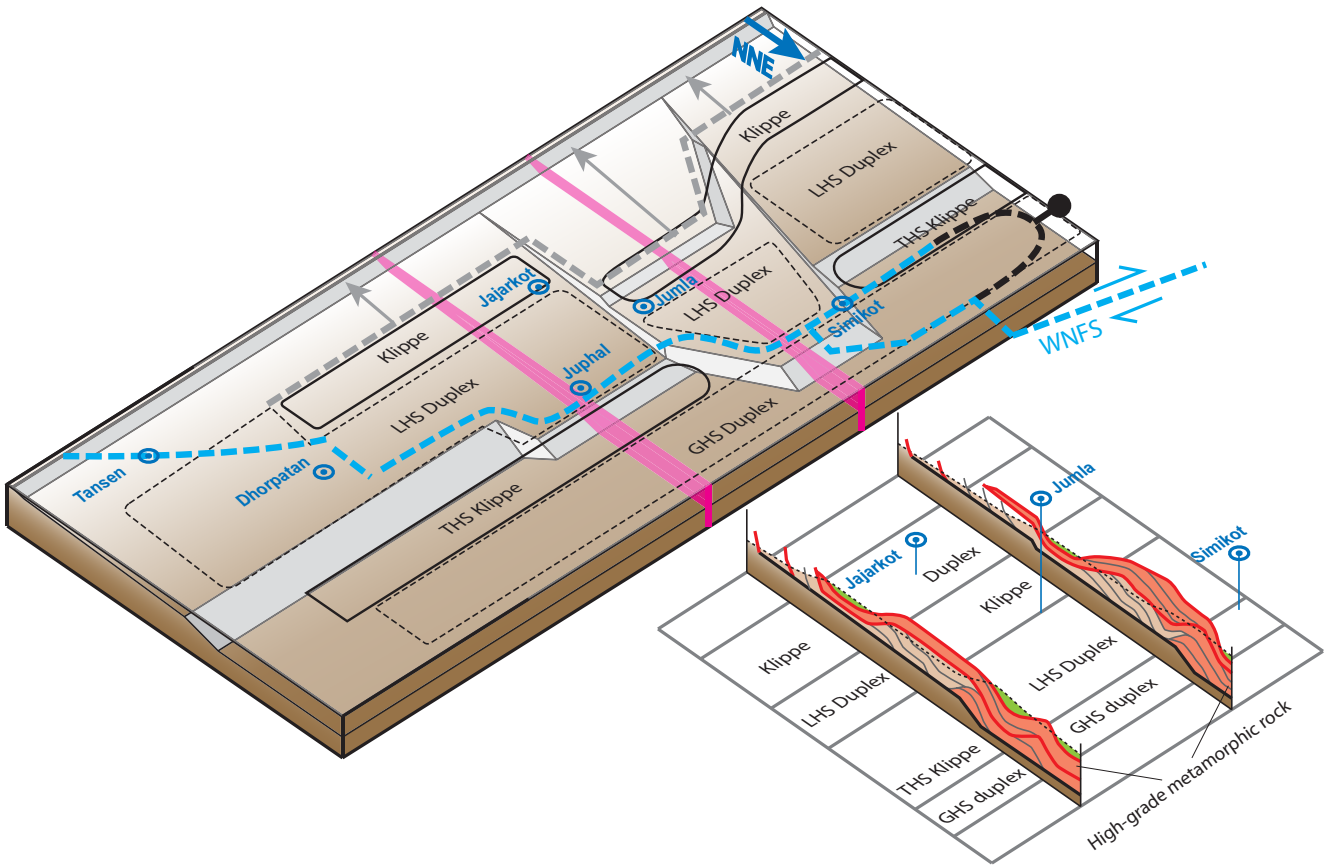

Figure 10. Three-dimensional conceptual model of the Main Himalayan Thrust (MHT) in the western Nepal Himalaya with two simplified cross-sections that show the along-strike variation in first-order structures. Refer to the text for the description and the correlation with main geological features.

duplexing kinematically requires the formation of new crustal slices and their advection to the base of the orogen in the hinterland over successive cycles. Thermomechanical models show that each accretion cycle generates transient topographic growth above the crustal ramp, which translates with the crustal ramp to the hinterland after their generation, resulting in a permanent increase in the orogen width (Mercier et al., 2017). Considering these kinematics we used a narrower window of accretion than previous studies but let it advect to the hinterland in a cycle. In this design, the total one-cycle accretion, if plotted in an uplift profile along the transect, has an isosceles trapezoid shape, consistent with the common antiformal shape of a duplex (Figure 5).

The crustal accretion process in the two accretion-involved best-fit models is also consistent with many other observations. First, the total crustal accretion is in the hinterland above the present midlower crustal ramp, and it corresponds well with the northern Himalayan anticline, which is consistent with the conceptual model proposed by Fan and Murphy (2021). Second, the hinterland-ward advection of the instantaneous accretion window relative to the matter in the upper plate is consistent with the finding that to produce the observation-fitting ages in central Nepal Himalaya, a thermokinematic model requires the recent up-dip advection of a duplex structure over a ramp (Ghoshal et al., 2020). Third, the high-slope zone is on the southern flank of antiformal crustal accretion, which is consistent with the geomorphological modeling results that the enhanced uplift caused by duplexing or advection over a ramp can cause the highest river steepness in the forelimb of the uplift zone (Adams et al., 2016; Eizenhöfer et al., 2019). Lastly, the uplift rates caused by the crustal accretion and rock advection over the midlower crustal ramp in the preferred models are broadly consistent with previous exhumation-rate studies at different locations in the Himalaya. The preferred models have an accretion velocity of ~5.2 mm/yr, adding the uplift caused by advection over midlower crustal ramp resulting in a total uplift rate of ~6.1 mm/yr. The instantaneous velocity is consistent with the observed short-term deformation or erosion, such as geodetic observations at various locations (Bilham et al., 1997; Grandin et al., 2012; Jackson & Bilham, 1994; Jackson et al., 1992); fluvial incision rates estimated from the modern channel geometries (Lavé & Avouac, 2001); and erosion rates

estimated from petrographic and mineralogical data of modern river sediments (Garzanti et al., 2007). If considering the time span of one accretion cycle (6 Ma), the average uplift rate can be determined by the accretion rate, width of the accretion window, and advection rate of the accretion window in the model: In our preferred models, the temporally average uplift rates of the crest part of the antiformal accretion are about 1.81 mm/yr (WNP02) and 2.24 mm/yr (WNP03), which, adding the uplift component caused by advection over the midlower crustal ramp, results in 2.73 and 3.17 mm/yr for total average uplift rates respectively. They are broadly consistent with studies on long-term erosion rates, including the results from bedrock thermochronology (Adams et al., 2009; Blythe et al., 2007; Burbank et al., 1996, 2003; Huntington et al., 2006; Thiede & Ehlers, 2013; Thiede et al., 2009), from bedrock thermochronology with thermokinematic modeling (Adams et al., 2015; Herman et al., 2010; Landry et al., 2016; McCallister et al., 2014; Stübner et al., 2018), and from detrital thermochronology (Brewer et al., 2006; Copeland et al., 2015; Huntington & Hodges, 2006; Szulc et al., 2006). They are also broadly consistent with studies on the current average erosion rate in catchment-scale determined by cosmogenic nuclides in quartz from river sediments (Ojha et al., 2019; Scherler et al., 2014; Vance et al., 2003) and on geochemical mass-balance of erosion fluxes of modern rivers (Galy & France-Lanord, 2001).

Our models also highlight the important role of ductile accretion in or below the brittle-ductile transition zone along the MHT in determining the most active-uplift front and thus the edge of the plateau. Many previous thermokinematic models that highlight the role of crustal accretion in other Himalayan regions correlate the accretion in their models with the LHS duplex in the footwall of the MCT. Unlike these models, our models of the western Nepal Himalaya suggest the midlower crustal accretion causes the thickening of the northern Himalayan anticline (Figure 9), where high-grade metamorphic rocks with protolith from both the GHS and LHS are exposed (Godin et al., 2021; Murphy, 2007). Modified from the original critical taper model that considers only friction material (Dahlen, 1990; Dahlen et al., 1984; Davis et al., 1983), a brittle-ductile taper model has predicted that a wedge with brittle-ductile transition in both the wedge and decollement parts can maintain a high-slope zone connecting a taper-like outer wedge and a plateau-like inner wedge at a critical state (Williams et al., 1994). A recent numerical simulation incorporating temperature-controlled rheological transitions also predicts the high-slope topography and concentrated ductile strain associated with the brittle-ductile transition in an accretionary prism (Pajang et al., 2022). While crustal accretion associated with rheological change determines the location of the high-slope zone of a wedge, the duplexing structures found at other structural depths indicate that material accretion from the lower plate to the upper plate may be an important mechanism of self-similar wedge growth and thus requires a complex multiramp megathrust geometry. For example, to the south of the high-slope zone or the active crustal accretion zone above the midlower crustal MHT ramp, the LHS duplex is also well-developed and is interpreted to develop by the southward propagation of crustal accretion on an upper-crustal flat (e.g., DeCelles et al., 2001, 2020; Figure 10). Recently, the LHS duplex has been interpreted as active in central Nepal based on the seismicity data (Mendoza et al., 2019). Further to the foreland, between the MBT and MFT, the older foreland basin strata group (SG) also exhibits duplex structure (e.g., Mugnier et al., 1999). A recent study on the rear side of the wedge suggests that thrust duplexing at depth is also active in South Tibet (Taylor et al., 2021).

Crustal thickening via multilayer duplexing is observed or proposed not only in Tibet-Himalayan orogenic system, such as the Kunlun range (Wang et al., 2011), Qilian Shan (Zuza et al., 2018), northern Indo-Burma range (Haproff et al., 2020), Yarlung suture (Laskowski et al., 2018), Lhasa terrane (Shi et al., 2020), but also in many other convergent wedges, such as the Cascadia Subduction Zone (Brandon & Vance, 1992; Calvert et al., 2006), the Appalachian (Ando et al., 1984), and Alaska (Fuis et al., 1997, 2008; Moore et al., 1997; Sample & Fisher, 1986; Wissinger et al., 1997). However, how rheologic change and material accretion affect the formation and evolution of a midlower crustal ramp and the duplexes above it remains unclear. Numerical and analogue simulations designed for investigating the kinematics of deformation and the evolution of megathrust ramps usually ignore the rheology change along the megathrust and the lower-plate deformation as it subducts (e.g., Dal Zilio et al., 2020b; Ghosh et al., 2020; Malavieille, 2010; Mugnier et al., 1997; Shen et al., 2020). These models usually require the preexistence of weak layers in the lower plate to generate duplexes, and the weak layers usually behave as décollements after being involved in the wedge deformation. In these models, once a ramp forms, it can only underthrust to the hinterland without deformation in the footwall until a new ramp forms in the foreland. This kinematics may be consistent with the upper-crustal structures but are not valid for the evolution of the midlower crustal ramps. The formation and sustaining of a midlower crustal ramp have been conceptually explained by flexural depression of the lower plate driven by gravity load of the orogen or plateau

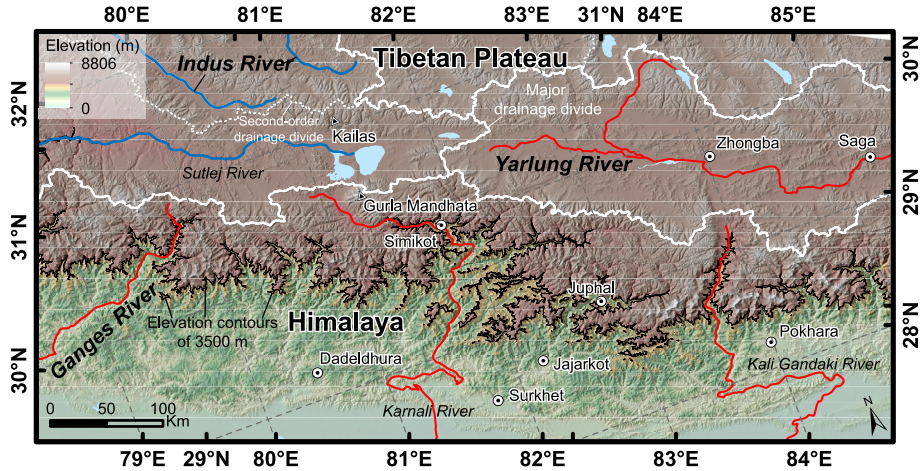

Figure 11. Map shows the topography, landform, and drainage systems of the central-western Nepal Himalayan and adjacent areas. The blue and red lines represent rivers that flow to Indus fan and Bengal fan, respectively. Notice the along-strike change in the width of the orogenic plateau landscape, approximately the area between the 3,500 m elevation contours and the southern divides of Indus and Yarlung River systems, and that the major drainage divide between the Indus River system and Yarlung River system is to the north of the topographic embayment in Simikot segment.

(Coward, 1983), and mechanical models suggest the strength of the underthrusting lithosphere affects the geometry of the fault (Lyon-Caen & Molnar, 1985; Molnar & Lyon-Caen, 1988). Therefore, temperature-dependent rheology and lower-plate deformation may need to be considered in future modeling on the evolution of the midlower crustal ramp in an orogen.

6.4. Effects of Crustal Accretion on the Landscape of the Himalayan Orogen

The growth of the inner wedge caused by midlower crustal accretion may have significantly affected the drainage systems and landscape of the southern edge of the Tibetan plateau. The present landscape of the Himalaya, from north to south, is characterized by the longitudinal Indus and Yarlung River systems, a plateau of high-elevation and low-relief, and an outer wedge of high-relief landscape, and the extent of these features varies along-strike (Figure 11). The Indus and Yarlung drainage systems are separated from drainage systems within the Tibetan plateau to the north and the outer Himalayan wedge to the south by drainage divides (Figure 11). However, in the late Oligocene-early Miocene, the landscape between the Gangdese range in south Tibet and the Himalaya to the south was characterized by extensive lakes rather than longitudinal river systems (e.g., DeCelles et al., 2018). If trans-Himalaya rivers existed in the central Himalaya, this stage might also be approximately the end of their lifespan (discussed below).

On the northern side of the Himalaya range, the formation of the longitudinal Indus and Yarlung drainage systems may be caused by the uplift of the northern Himalaya and shortening on both sides of the present drainage system. On the northern side of the Himalaya along the Indus-Yarlung suture zone, low-altitude warm-water great lakes existed during Oligocene-Miocene time (26-21 Ma; DeCelles et al., 2018). Early deposition of the Kailas Formation during this period is interpreted to be caused by regional extension as the subducting slab rolls back (Carrapa et al., 2014; DeCelles et al., 2011), and the detrital sources are mostly the Gangdese range to its north. Late stages of the deposition recorded the addition of the THS source from its south. The change in source is interpreted to be caused by the activation of the north-directed Great Counter Thrust (GCT) at the rear of the Himalaya range (DeCelles et al., 2011). Along the suture and the Gangdese, studies also suggest crustal duplex at depth developed from ca. 23 Ma (Laskowski et al., 2018). Before the source change in the Kailas basin, during Oligocene, the Himalaya was thickening in the THS and GHS (e.g., Carosi et al., 2010; Murphy & Yin, 2003; Ratschbacher et al., 1994; Searle et al., 1987) and an Oligocene unconformity developed in the foreland (Najman & Garzanti, 2000). The unconformity represents changes in the foreland sedimentary environment from marine to continental and in detritus source from the THS and the Yarulung suture zone to the THS and GHS (Baral et al., 2016, 2017, 2022; Bernet et al., 2006; DeCelles et al., 1998a, 1998b, 2004; Najman & Garzanti, 2000; Najman et al., 2005; Szulc et al., 2006). Therefore, if trans-Himalaya rivers existed, as suggested

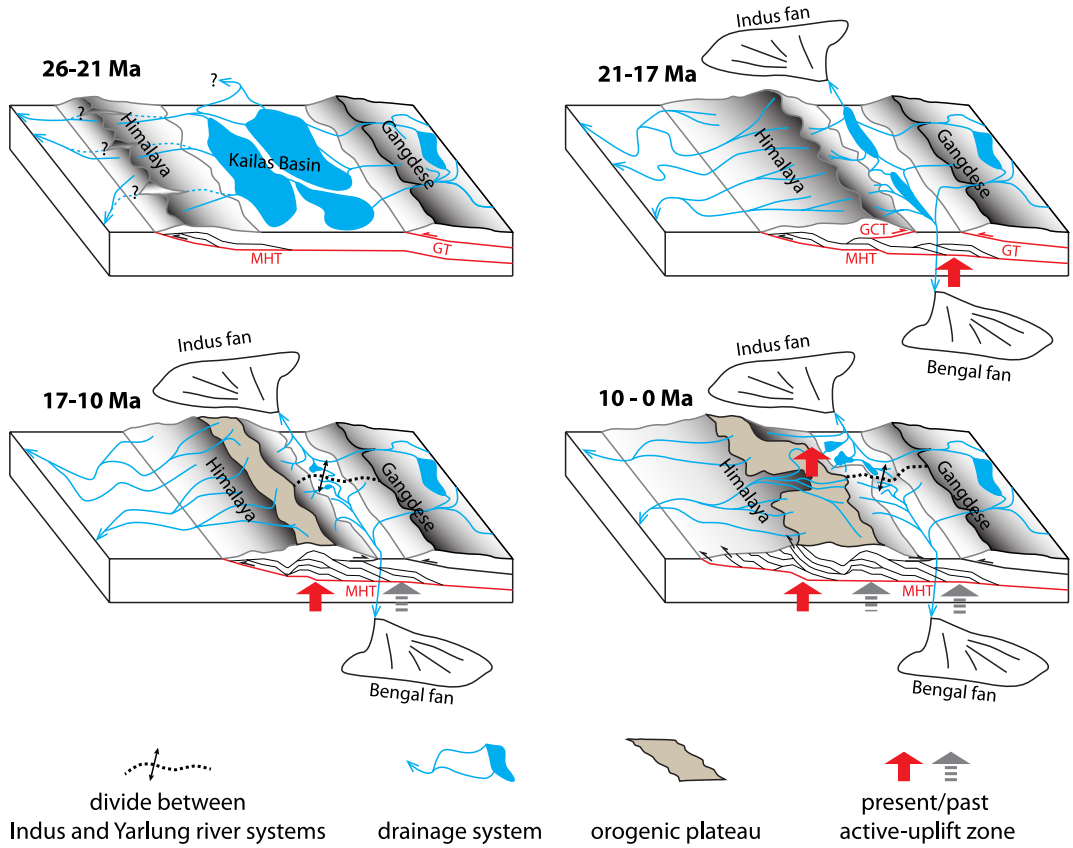

Figure 12. Conceptual evolution model of the drainage system and landscape of the area across the western Nepal Himalaya and adjacent areas.

by Cina et al. (2009) and Tremblay et al. (2015) in the eastern Himalaya and by Yin (2006) in a conceptual model, in the central Himalaya, they might be ceasing during the Oligocene and the drainage divide between the outer Himalayan wedge and the Kailas Basin might be forming. The divide should have established before the postunconformity deposition in the early-middle Miocene to explain the lack of material from south Tibet in the foreland basin, which is an important difference from the foreland basin record in the eastern Himalaya. A recent study in Indus Basin in Central Ladakh suggests the basin started to receive Gangdese detritus transported by a west-flowing Indus River from south Tibet in the late Oligocene (Bhattacharya et al., 2021). If this is true, it might result from the drainage reorganization in response to the cession of trans-Himalaya rivers. Cooling ages of the Kailas basin suggest postdepositional exhumation at around 17 ± 1 Ma (Carrapa et al., 2014), and are interpreted to reflect the initial rapid incision of the longitudinal river systems. The Indus basin also experienced postdepositional exhumation starting from ca. 20 Ma and throughout the Miocene (Bhattacharya et al., 2020). A model with a well-established longitudinal river system in this stage is also consistent with the coeval fast exhumation rate documented in south Tibet along the eastern downstream part of the Yarlung River drainage system during the middle Miocene (Dai et al., 2021; Li et al., 2016, 2017; Tremblay et al., 2015). We suggested above that the northern Himalaya anticline may have developed coevally due to midlower crustal accretion and ceased due to a forelandward propagation in some segments at ca. 10 Ma. The continuous and overall forelandward propagating deformation within the Himalayan wedge may have been contributing to the maintaining of the divide between the outer Himalaya range and the longitudinal river systems to its north. Therefore, we posit that the crustal accretion may have facilitated the development of the river systems (Figure 12). North-south shortening along the GCT and the Gangdese thrust made the area between the Gangdese range and Himalaya range narrow (Harrison et al., 2000; Orme, 2019; Quidelleur et al., 1997; Ratschbacher et al., 1994; Searle et al., 1987; Yin et al., 1994, 1999). This together with the preceding thickening of the THS and GHS and the possible cessation of trans-Himalaya rivers therefore facilitated localization of the drainage systems. Subsequent crustal accretion along the suture and the Gangdese (ca. 23-15 Ma; Copeland et al., 1987; Laskowski et al., 2018; Quidelleur et al., 1997;

Searle et al., 1987; Taylor et al., 2021; Yin et al., 1994) and later the Northern Himalaya anticline (ca. 15-10 Ma; this study), and probably also slab detachment of the subducting plate (ca. 17 Ma; Carrapa et al., 2014; Chemenda et al., 2000; Husson et al., 2014; Mugnier & Huyghe, 2006; Shen et al., 2016; Webb et al., 2017), caused elevation gain in the area (Ding et al., 2017) and rapid incision of the Indus and Yarlung River systems. This process may have further facilitated the localization of the longitudinal river systems as suggested by wind gaps along the drainage divides on both sides of the longitudinal rivers (e.g., Buceta et al., 2020; Murphy & Burgess, 2006). At the rear of the eastern Himalaya, along the eastern Gangdese, previous studies invoke alternative models, such as intensification of Asian monsoon and advection of more moisture through Miocene trans-Himalaya river valleys, to explain the fast exhumation rate during the middle Miocene (Dai et al., 2021; Tremblay et al., 2015). However, as we suggested above, in the central Himalaya, a divide between the outer Himalaya and the river systems to the north should have developed in the early Miocene. Therefore, these models are unlikely to be true for the central Himalaya. We cannot preclude the possibility that trans-Himalaya rivers never existed in the central Himalaya because no direct depositional record has been reported. In the eastern Himalaya, alternative river capture models that do not involve trans-Himalaya rivers are also proposed to explain the appearance of Gangdese detritus in the foreland (e.g., Govin et al., 2018; Lang & Huntington, 2014). It is not clear if the Oligocene unconformity in the foreland is created by nondeposition or erosion. Detailed provenance studies of the units directly below and above the unconformity or, if can be discovered, the unit filling the sedimentary gap represented by the foreland unconformity may reveal the history of trans-Himalaya rivers.

The Indus and Yarlung River systems extend approximately parallel with the Himalaya at the rear. The Indus River system drains the western part westward to the Indus fan, and the Yarlung River system drains the central-eastern segment eastward to the Bengal fan. The divide between the two river-system catchments is to the north of the topographic embayment in western Nepal (Figure 11). This spatial coincidence raises two questions; how did this divide form and when did it evolve to its present location? Yin (2006) originally proposed that this drainage divide may have been controlled by subduction of basement ridges in the Indian plate and that it might have shifted from ridge to ridge to its current position by headwater erosion. Given that the topographic embayment developed on a structurally high MHT segment which might have pushed the hinterland midlower crustal accretion further to the north compared along-strike (this study and Fan & Murphy, 2021), we propose an alternative basement-ridge-control model; the divide may be controlled by this structurally high MHT segment rather than the large basement ridges. If this is correct, the divide should have established its present location by ca. 10 Ma, when the midlower crustal lateral ramps of the MHT in the embayment area developed. If the drainage systems were affected by the wedge-parallel extension that initiated at ca. 15 Ma in the Gurla Mandhata and Xiao Gurla areas (McCallister et al., 2014), the divide may start to develop at its present location as early as then. This model suggests that the divide between the Indus River system and the Yarlung River system may have established its present location approximately as soon as the river systems formed or localized (Figure 12). Our model calls on detailed studies on the paleoflow of Neogene strata and the existence of trans-Himalaya rivers directly to the east of the present divide. If the present divide developed very late, as suggested by the conceptual model presented by Yin (2006), the strata to the east of the divide should record local flow reversal. However, our preferred early-divide model predicts continuous east flow. If the eastern part of the Yarlung River once flew to the west (Cina et al., 2009; Taylor et al., 2021; Zhang et al., 2012), our model further requires the existence of trans-Himalaya rivers to drain the basin to the foreland of the Himalaya.

To the south of the Indus and Yarlung drainage systems across a drainage divide, the growth of the Himalayan-plateau landscape might be controlled by the evolution of midlower crustal accretion. In western Nepal, the drainage divide between Yarlung drainage system and the Himalayan orogenic plateau follows the northern Himalaya anticline; the southern edge of the plateau landscape approximately follows the northern limit of the high-slope zone, which varies in its location along-strike (Figure 11). Therefore, the width of the inner wedge also varies along the strike. In far-western Nepal, along the apex of the topographic embayment, the plateau part is narrow, while in the segment from Dolpo area to the Thakkhola graben, approximately corresponding to the Dolpo THS syncline, the plateau landscape is relatively wide (Figure 11). If the active-uplift front caused by midlower crustal accretion migrated from the northern Himalaya anticline to its present location as lateral or oblique ramps in MHT at midlower-crustal depth developed (this study and Fan & Murphy, 2021), the inner wedge or the plateau landscape might have expanded at the same time with along-strike variation. Two factors could contribute to this process: (a) the southward migration of the midlower crustal accretion contributed to building the topography; (b) due to the orographic precipitation effect (Bookhagen & Burbank, 2006; Ding et al., 2017), the aridification

to the north of the active-uplift front could facilitate the preservation of the plateau landscape built by earlier midlower crustal accretion. The coevolution of the midlower crustal accretion and plateau expansion is similar to the well-studied forming process of intermontane basins or piggyback basins that resulted from the forelandward propagation of deformation in fold-and-thrust belts (e.g., Coutand et al., 2006; Hilley & Strecker, 2005; Pingel et al., 2020; Ruetenik et al., 2018; Sobel et al., 2003). This proposed process is also consistent with the landscape evolution modeling of the forming process of high-elevation, low-relief landscape patches in the lower Himalaya area via duplex deformation at depth (Adams et al., 2016) and in the southeast Tibetan Plateau via propagating uplift (Yuan et al., 2021).

7. Conclusion

Our thermokinematic models suggest that the MHT along the Karnali River transect is characterized by two ramps connected by a long upper-crustal flat and a midlower crustal ramp in the hinterland farther to the north with a gentler slope compared with the midlower crustal ramps in adjacent segments. The models that can successfully produce observed cooling ages of MsAr, AFT, ZHe, and AHe dating systems should invoke crustal accretion. The youngest cluster of the cooling ages and the high-slope zone of the orogenic wedge are above the forelimb of the antiformal crustal accretion, which spatially overlaps the northern Himalaya anticline in far-western Nepal in our model. These findings suggest that the crustal accretion along the midlower crustal ramp controls the location of the active-uplift front of the orogenic wedge and the migration of the location controls the outward growth of an orogenic plateau. The coexistence of the duplex structures in the upper-crustal depth with the midlower crustal accretion we modeled suggests that crustal accretion at different depths or multilayer duplexing is an important mechanism for maintaining the wedge shape predicted by the critical taper theory.

The ZHe ages reported here from the western Nepal Himalaya support that the northern branch of the high-slope zone or the PT2-N is the active-uplift front of the plateau in the area and that the along-strike change in the location of the active-uplift front is an expression of the along-strike change in MHT geometry. The midlower crustal lateral and oblique ramps of a 3-D MHT geometric model for the western Nepal Himalaya on the base of the along-strike variations in active-uplift front location can be correlated well with the surficial geological features. Cooling ages in this region also suggest that the midlower crustal lateral and oblique ramps in MHT started to develop at least by ca. 10 Ma, when the crustal accretion building the northern Himalaya anticline ceased in the segment between the modeled transect and the Thakkhola graben and started to migrate southward to its present location. Integrating other geologic data across the Himalaya, we propose that the deep tectonic process may have controlled the first-order evolution of the landscape and drainage systems. Our tectonic-landscape evolution model includes the processes of the transition from the landscape featured by low-elevation big lakes to the localized river systems, the cessation of the trans-Himalaya rivers if they once existed, the development of the drainage divide between the Indus River system and the Yarlung River system, the southward growth of the inner-wedge plateau landscape with along-strike variations, and the formation of the topographic embayment in western Nepal.

Data Availability Statement

The reported zircon (U-Th)/He ages (Table 1) and the sample information (Table S1 in Supporting Information S1) are stored in the Texas Data Repository (Fan, 2022; https://doi.org/10.18738/T8/UU1YN1).

Acknowledgments
This study is funded by National Science Foundation to Michael Murphy (1827863) and Michael Taylor (1827866). We acknowledge the use of the Sabine Cluster and the advanced support from the Research Computing Data Core at the University of Houston to carry out the research presented here. We appreciate logistical support provided by Bhim Chand with Earth's Paradise Treks and Expeditions. Comments by Peter van der Beek, Matthew Fox and the Associate Editor, Djordje Grujic greatly helped to improve our manuscript. We acknowledge editorial handling by the Editor, Laurent Jolivet.

References

Adams, B., Dietsch, C., Owen, L. A., Caffee, M. W., Spotila, J., & Haneberg, W. C. (2009). Exhumation and incision history of the Lahul Himalaya, northern India, based on (U-Th)/He thermochronometry and terrestrial cosmogenic nuclide methods. *Geomorphology*, *107*(3), 285–299. https://doi.org/10.1016/j.geomorph.2008.12.017

Adams, B. A., Hodges, K. V., Whipple, K. X., Ehlers, T. A., van Soest, M. C., & Wartho, J. (2015). Constraints on the tectonic and landscape evolution of the Bhutan Himalaya from thermochronometry. *Tectonics*, *34*, 1329–1347. https://doi.org/10.1002/2015TC003853

Adams, B. A., Whipple, K. X., Hodges, K. V., & Heimsath, A. M. (2016). In situ development of high-elevation, low-relief landscapes via duplex deformation in the Eastern Himalayan hinterland, Bhutan. *Journal of Geophysical Research: Earth Surface*, *121*, 294–319. https://doi.org/10.1002/2015JF003508

Ader, T., Avouac, J.-P., Liu-Zeng, J., Lyon-Caen, H., Bollinger, L., Galetzka, J., et al. (2012). Convergence rate across the Nepal Himalaya and interseismic coupling on the Main Himalayan Thrust: Implications for seismic hazard. *Journal of Geophysical Research*, *117*, B04403. https://doi.org/10.1029/2011JB009071

Ando, C. J., Czuchra, B. L., Klemperer, S. L., Brown, L. D., Cheadle, M. J., Cook, F. A., et al. (1984). Crustal profile of mountain belt: COCORP deep seismic reflection profiling in New England Appalachians and implications for architecture of convergent mountain Chains1. *AAPG Bulletin*, *68*(7), 819–837. https://doi.org/10.1306/ad461430-16f7-11d7-8645000102c1865d

Avouac, J.-P. (2003). Mountain building, erosion, and the seismic cycle in the Nepal Himalaya. *Advances in Geophysics*, *46*, 1–80.

Bai, L., Klemperer, S. L., Mori, J., Karplus, M. S., Ding, L., Liu, H., et al. (2019). Lateral variation of the Main Himalayan Thrust controls the rupture length of the 2015 Gorkha earthquake in Nepal. *Science Advances*, *5*(6), eaav0723. https://doi.org/10.1126/sciadv.aav0723

Baltz, T., Murphy, M., Fan, S., & Chamlagain, D. (2021). Geometry, kinematics, and magnitude of extension across the Thakkhola graben, central Nepal Himalaya. *Journal of Nepal Geological Society*, *62*, 1–17. https://doi.org/10.3126/jngs.v62i0.38691

Baral, U., Ding, L., & Chamlagain, D. (2016). Detrital zircon U-Pb geochronology of the Siwalik Group of the Nepal Himalaya: Implications for provenance analysis. *International Journal of Earth Sciences*, *105*(3), 921–939. https://doi.org/10.1007/s00531-015-1198-7

Baral, U., Ding, L., & Chamlagain, D. (2017). Detrital zircon ages and provenance of Neogene foreland basin sediments of the Karnali River section, western Nepal Himalaya. *Journal of Asian Earth Sciences*, *138*, 98–109. https://doi.org/10.1016/j.jseaes.2017.02.003

Baral, U., Ding, L., Dhital, M. R., Kumar, K. C., & Li, S. (2022). Paleozoic-Mesozoic dispersal of Gondwana: Insights from detrital zircon geochronology of Lesser Himalaya strata, eastern Nepal. *GSA Bulletin*. https://doi.org/10.1130/B36216.1

Beaumont, C. (2004). Crustal channel flows: 1. Numerical models with applications to the tectonics of the Himalayan-Tibetan orogen. *Journal of Geophysical Research*, *109*, B06406. https://doi.org/10.1029/2003JB002809

Bendick, R., & Bilham, R. (2001). How perfect is the Himalayan arc? *Geology*, *29*(9), 791–794. https://doi.org/10.1130/0091-7613(2001)029<0791:Hpitha>2.0.Co;2

Berger, A., Jouanne, F., Hassani, R., & Mugnier, J. L. (2004). Modelling the spatial distribution of present-day deformation in Nepal: How cylindrical is the Main Himalayan Thrust in Nepal? *Geophysical Journal International*, *156*(1), 94–114. https://doi.org/10.1111/j.1365-246X.2004.02038.x

Bernet, M., van der Beek, P., Pik, R., Huyghe, P., Mugnier, J.-L., Labrin, E., & Szulc, A. (2006). Miocene to Recent exhumation of the central Himalaya determined from combined detrital zircon fission-track and U/Pb analysis of Siwalik sediments, western Nepal. *Basin Research*, *18*(4), 393–412. https://doi.org/10.1111/j.1365-2117.2006.00303.x

Berthet, T., Hetényi, G., Cattin, R., Sapkota, S. N., Champollion, C., Kandel, T., et al. (2013). Lateral uniformity of India Plate strength over central and eastern Nepal. *Geophysical Journal International*, *195*(3), 1481–1493. https://doi.org/10.1093/gji/ggt357

Bhattacharya, G., Robinson, D. M., Orme, D. A., Najman, Y., & Carter, A. (2020). Low-temperature thermochronology of the Indus Basin in Central Ladakh, Northwest India: Implications of Miocene-Pliocene cooling in the India-Asia Collision Zone. *Tectonics*, *39*, e2020TC006333. https://doi.org/10.1029/2020TC006333

Bhattacharya, G., Robinson, D. M., & Wielicki, M. M. (2021). Detrital zircon provenance of the Indus Group, Ladakh, NW India: Implications for the timing of the India-Asia collision and other syn-orogenic processes. *GSA Bulletin*, *133*(5–6), 1007–1020. https://doi.org/10.1130/B35624.1

Bilham, R., Larson, K., Freymueller, J., Jouanne, F., LeFort, P., Leturmy, P., et al. (1997). GPS measurements of present-day convergence across the Nepal Himalaya. *Nature*, *386*(6620), 61–64. https://doi.org/10.1038/386061a0

Blythe, A. E., Burbank, D. W., Carter, A., Schmidt, K., & Putkonen, J. (2007). Plio-Quaternary exhumation history of the central Nepalese Himalaya: 1. Apatite and zircon fission track and apatite [U-Th]/He analyses. *Tectonics*, *26*, TC3002. https://doi.org/10.1029/2006TC001990

Bollinger, L., Avouac, J. P., Beyssac, O., Catlos, E. J., Harrison, T. M., Grove, M., et al. (2004). Thermal structure and exhumation history of the Lesser Himalaya in central Nepal. *Tectonics*, *23*, TC5015. https://doi.org/10.1029/2003TC001564

Bollinger, L., Henry, P., & Avouac, J. (2006). Mountain building in the Nepal Himalaya: Thermal and kinematic model. *Earth and Planetary Science Letters*, *244*(1–2), 58–71. https://doi.org/10.1016/j.epsl.2006.01.045

Bollinger, L., Tapponnier, P., Sapkota, S. N., & Klinger, Y. (2016). Slip deficit in central Nepal: Omen for a repeat of the 1344 AD earthquake? *Earth Planets and Space*, *68*(1), 1–12. https://doi.org/10.1186/s40623-016-0389-1

Bookhagen, B., & Burbank, D. W. (2006). Topography, relief, and TRMM-derived rainfall variations along the Himalaya. *Geophysical Research Letters*, *33*, L08405. https://doi.org/10.1029/2006GL026037

Braden, Z., Godin, L., Cottle, J., & Yakymchuk, C. (2018). Renewed late Miocene (<8 Ma) hinterland ductile thrusting, western Nepal Himalaya. *Geology*, *46*(6), 503–506. https://doi.org/10.1130/g40097.1

Braden, Z., Godin, L., Kellett, D. A., & Yakymchuk, C. (2020). Spatio-temporal challenges in dating orogen-scale shear zones: The case of the Himalayan Main Central Thrust. *Tectonophysics*, *774*, 228246. https://doi.org/10.1016/j.tecto.2019.228246

Brandon, M. T., & Vance, J. A. (1992). Tectonic evolution of the Cenozoic Olympic subduction complex, Washington State, as deduced from fission track ages for detrital zircons. *American Journal of Science*, *292*(8), 565–636. https://doi.org/10.2475/ajs.292.8.565

Braun, J. (2003). Pecube: A new finite-element code to solve the 3D heat transport equation including the effects of a time-varying, finite amplitude surface topography. *Computers & Geosciences*, *29*(6), 787–794. https://doi.org/10.1016/S0098-3004(03)00052-9

Braun, J., van der Beek, P., Valla, P., Robert, X., Herman, F., Glotzbach, C., et al. (2012). Quantifying rates of landscape evolution and tectonic processes by thermochronology and numerical modeling of crustal heat transport using PECUBE. *Tectonophysics*, *524–525*, 1–28. https://doi.org/10.1016/j.tecto.2011.12.035

Brewer, I. D., Burbank, D. W., & Hodges, K. V. (2006). Downstream development of a detrital cooling-age signal: Insights from $^{40}Ar/^{39}Ar$ muscovite thermochronology in the Nepalese Himalaya. *Geological Society of America Special Papers*, *398*, 321–338. https://doi.org/10.1130/2006.2398(20)

Brubacher, A. D., Larson, K. P., Cottle, J. M., Matthews, W., & Camacho, A. (2020). Progressive development of E-W extension across the Tibetan plateau: A case study of the Thakkhola graben, west-central Nepal. *International Geology Review*, *63*, 1900–1919. https://doi.org/10.1080/00206814.2020.1808860

Brunel, M. (1986). Ductile thrusting in the Himalayas: Shear sense criteria and stretching lineations. *Tectonics*, *5*(2), 247–265. https://doi.org/10.1029/TC005i002p00247

Buceta, R. E., Schoenbohm, L. M., & DeCelles, P. G. (2020). Glacial and fluvial erosion in the Dolpo Basin, Western Nepal. *Geomorphology*, *354*, 107033. https://doi.org/10.1016/j.geomorph.2020.107033

Burbank, D. W., Blythe, A. E., Putkonen, J., Pratt-Sitaula, B., Gabet, E., Oskin, M., et al. (2003). Decoupling of erosion and precipitation in the Himalayas. *Nature*, *426*(6967), 652–655. https://doi.org/10.1038/nature02187

Burbank, D. W., Leland, J., Fielding, E., Anderson, R. S., Brozovic, N., Reid, M. R., & Duncan, C. (1996). Bedrock incision, rock uplift and threshold hillslopes in the northwestern Himalayas. *Nature*, *379*(6565), 505–510. https://doi.org/10.1038/379505a0

Burchfiel, B. C., Zhiliang, C., Hodges, K. V., Yuping, L., Royden, L. H., Changrong, D., & Jiene, X. (1992). The South Tibetan Detachment System, Himalayan orogen: Extension contemporaneous with and parallel to shortening in a collisional mountain belt. *Geological Society of America Special Papers*, *269*, 1–41. https://doi.org/10.1130/SPE269-p1

Burg, J. P., Brunel, M., Gapais, D., Chen, G. M., & Liu, G. H. (1984). Deformation of leucogranites of the crystalline Main Central Sheet in southern Tibet (China). *Journal of Structural Geology*, *6*(5), 535–542. https://doi.org/10.1016/0191-8141(84)90063-4

Burg, J. P., & Chen, G. M. (1984). Tectonics and structural zonation of Southern Tibet, China. *Nature*, *311*(5983), 219–223. https://doi.org/10.1038/311219a0

Caldwell, W. B., Klemperer, S. L., Lawrence, J. F., Rai, S. S., & Ashish (2013). Characterizing the Main Himalayan Thrust in the Garhwal Himalaya, India with receiver function CCP stacking. *Earth and Planetary Science Letters*, *367*, 15–27. https://doi.org/10.1016/j.epsl.2013.02.009

Calvert, A. J., Ramachandran, K., Kao, H., & Fisher, M. A. (2006). Local thickening of the Cascadia forearc crust and the origin of seismic reflectors in the uppermost mantle. *Tectonophysics*, *420*(1–2), 175–188. https://doi.org/10.1016/j.tecto.2006.01.021

Cannon, J. M., & Murphy, M. A. (2014). Active lower crustal deformation and Himalayan seismic hazard revealed by stream channels and regional geology. *Tectonophysics*, *633*, 34–42. https://doi.org/10.1016/j.tecto.2014.06.031

Cannon, J. M., Murphy, M. A., & Taylor, M. (2018). Segmented strain accumulation in the high Himalaya expressed in river channel steepness. *Geosphere*, *14*(3), 1131–1149. https://doi.org/10.1130/GES01508.1

Carosi, R., Lombardo, B., Molli, G., Musumeci, G., & Pertusati, P. C. (1998). The south Tibetan detachment system in the Rongbuk valley, Everest region. Deformation features and geological implications. *Journal of Asian Earth Sciences*, *16*(2), 299–311. https://doi.org/10.1016/S0743-9547(98)00014-2

Carosi, R., Montomoli, C., & Iaccarino, S. (2018). 20 years of geological mapping of the metamorphic core across Central and Eastern Himalayas. *Earth-Science Reviews*, *177*(Suppl. C), 124–138. https://doi.org/10.1016/j.earscirev.2017.11.006

Carosi, R., Montomoli, C., Iaccarino, S., Massonne, H. J., Rubatto, D., Langone, A., et al. (2016). Middle to late Eocene exhumation of the Greater Himalayan Sequence in the Central Himalayas: Progressive accretion from the Indian plate. *Geological Society of America Bulletin*, *128*(11–12), 1571–1592. https://doi.org/10.1130/B31471.1

Carosi, R., Montomoli, C., Rubatto, D., & Visona, D. (2010). Late Oligocene high-temperature shear zones in the core of the Higher Himalayan Crystallines (Lower Dolpo, western Nepal). *Tectonics*, *29*, TC4029. https://doi.org/10.1029/2008TC002400

Carrapa, B., Orme, D. A., DeCelles, P. G., Kapp, P., Cosca, M. A., & Waldrip, R. (2014). Miocene burial and exhumation of the India-Asia collision zone in southern Tibet: Response to slab dynamics and erosion. *Geology*, *42*(5), 443–446. https://doi.org/10.1130/G35350.1

Carrapa, B., Robert, X., DeCelles, P. G., Orme, D. A., Thomson, S. N., & Schoenbohm, L. M. (2016). Asymmetric exhumation of the Mount Everest region: Implications for the tectono-topographic evolution of the Himalaya. *Geology*, *44*, 611–614. https://doi.org/10.1130/G37756.1

Catlos, E. J., Harrison, T. M., Kohn, M. J., Grove, M., Ryerson, F. J., Manning, C. E., & Upreti, B. N. (2001). Geochronologic and thermobarometric constraints on the evolution of the Main Central Thrust, central Nepal Himalaya. *Journal of Geophysical Research*, *106*(B8), 16177–16204. https://doi.org/10.1029/2000JB900375

Catlos, E. J., Lovera, O. M., Kelly, E. D., Ashley, K. T., Harrison, T. M., & Etzel, T. (2018). Modeling high-resolution pressure-temperature paths across the Himalayan Main Central Thrust (Central Nepal): Implications for the dynamics of collision. *Tectonics*, *37*, 2363–2388. https://doi.org/10.1029/2018TC005144

Cattin, R., & Avouac, J. P. (2000). Modeling mountain building and the seismic cycle in the Himalaya of Nepal. *Journal of Geophysical Research*, *105*(B6), 13389–13407. https://doi.org/10.1029/2000JB900032

Célérier, J., Harrison, T. M., Beyssac, O., Herman, F., Dunlap, W. J., & Webb, A. A. G. (2009). The Kumaun and Garwhal Lesser Himalaya, India: Part 2. Thermal and deformation histories. *Geological Society of America Bulletin*, *121*(9–10), 1281–1297. https://doi.org/10.1130/B26343.1

Chemenda, A. I., Burg, J.-P., & Mattauer, M. (2000). Evolutionary model of the Himalaya-Tibet system: Geopoem: Based on new modelling, geological and geophysical data. *Earth and Planetary Science Letters*, *174*(3), 397–409.

Cina, S. E., Yin, A., Grove, M., Dubey, C. S., Shukla, D. P., Lovera, O. M., et al. (2009). Gangdese arc detritus within the eastern Himalayan Neogene foreland basin: Implications for the Neogene evolution of the Yalu-Brahmaputra River system. *Earth and Planetary Science Letters*, *285*(1), 150–162. https://doi.org/10.1016/j.epsl.2009.06.005

Coleman, M., & Hodges, K. (1995). Evidence for Tibetan Plateau uplift before 14-Myr ago from a new minimum age for east-west extension. *Nature*, *374*(6517), 49–52. https://doi.org/10.1038/374049a0

Coleman, M. E. (1996). Orogen-parallel and orogen-perpendicular extension in the central Nepalese Himalayas. *GSA Bulletin*, *108*(12), 1594–1607. https://doi.org/10.1130/0016-7606(1996)108<1594:OPAOPE>2.3.CO;2

Copeland, P., Bertrand, G., France-Lanord, C., & Sundell, K. (2015). $^{40}Ar/^{39}Ar$ ages of muscovites from modern Himalayan rivers: Himalayan evolution and the relative contribution of tectonics and climate. *Geosphere*, *11*, 1837–1858. https://doi.org/10.1130/GES01154.1

Copeland, P., Harrison, T. M., Hodges, K. V., Maruéjol, P., Le Fort, P., & Pecher, A. (1991). An early Pliocene thermal disturbance of the main central thrust, central Nepal: Implications for Himalayan tectonics. *Journal of Geophysical Research*, *96*(B5), 8475–8500. https://doi.org/10.1029/91JB00178

Copeland, P., Mark Harrison, T., Kidd, W. S. F., Ronghua, X., & Yuquan, Z. (1987). Rapid early Miocene acceleration of uplift in the Gangdese Belt, Xizang (southern Tibet), and its bearing on accommodation mechanisms of the India-Asia collision. *Earth and Planetary Science Letters*, *86*(2), 240–252.

Cottle, J. M., Larson, K. P., & Kellett, D. A. (2015a). How does the mid-crust accommodate deformation in large, hot collisional orogens? A review of recent research in the Himalayan orogen. *Journal of Structural Geology*, *78*, 119–133. https://doi.org/10.1016/j.jsg.2015.06.008

Cottle, J. M., Searle, M. P., Jessup, M. J., Crowley, J. L., & Law, R. D. (2015b). Rongbuk re-visited: Geochronology of leucogranites in the footwall of the South Tibetan Detachment System, Everest Region, Southern Tibet. *Lithos*, *227*, 94–106. https://doi.org/10.1016/j.lithos.2015.03.019

Coutand, I., Carrapa, B., Deeken, A., Schmitt, A. K., Sobel, E. R., & Strecker, M. R. (2006). Propagation of orographic barriers along an active range front: Insights from sandstone petrography and detrital apatite fission-track thermochronology in the intramontane Angastaco basin, NW Argentina. *Basin Research*, *18*(1), 1–26. https://doi.org/10.1111/j.1365-2117.2006.00283.x

Coutand, I., Whipp, D. M., Grujic, D., Bernet, M., Fellin, M. G., Bookhagen, B., et al. (2014). Geometry and kinematics of the Main Himalayan Thrust and Neogene crustal exhumation in the Bhutanese Himalaya derived from inversion of multithermochronologic data. *Journal of Geophysical Research: Solid Earth*, *119*, 1446–1481. https://doi.org/10.1002/2013JB010891

Coward, M. P. (1983). Thrust tectonics, thin skinned or thick skinned, and the continuation of thrusts to deep in the crust. *Journal of Structural Geology*, *5*(2), 113–123. https://doi.org/10.1016/0191-8141(83)90037-8

Dahlen, F. A. (1990). Critical taper model of fold-and-thrust belts and accretionary wedges. *Annual Review of Earth and Planetary Sciences*, *18*(1), 55–99. https://doi.org/10.1146/annurev.ea.18.050190.000415

Dahlen, F. A., Suppe, J., & Davis, D. (1984). Mechanics of fold-and-thrust belts and accretionary wedges: Cohesive Coulomb Theory. *Journal of Geophysical Research*, *89*(B12), 10087–10101. https://doi.org/10.1029/JB089iB12p10087

Dai, J.-G., Fox, M., Han, X., Tremblay, M. M., Xu, S.-Y., Shuster, D. L., et al. (2021). Two stages of accelerated exhumation in the middle reach of the Yarlung River, Southern Tibet since the mid-Miocene. *Tectonics*, *40*,e2020TC006618. https://doi.org/10.1029/2020TC006618

Dal Zilio, L., Jolivet, R., & van Dinther, Y. (2020a). Segmentation of the Main Himalayan Thrust illuminated by Bayesian inference of interseismic coupling. *Geophysical Research Letters*, *47*, e2019GL086424. https://doi.org/10.1029/2019GL086424

Dal Zilio, L., Ruh, J., & Avouac, J.-P. (2020b). Structural evolution of Orogenic Wedges: Interplay between erosion and weak décollements. *Tectonics*, *39*, e2020TC006210. https://doi.org/10.1029/2020TC006210

Davis, D., Suppe, J., & Dahlen, F. A. (1983). Mechanics of fold-and-thrust belts and accretionary wedges. *Journal of Geophysical Research*, *88*(B2), 1153–1172. https://doi.org/10.1029/JB088iB02p01153

DeCelles, P. G., Carrapa, B., Ojha, T. P., Gehrels, G. E., & Collins, D. (2020). Structural and thermal evolution of the Himalayan Thrust Belt in Midwestern Nepal. In P. G. DeCelles, B. Carrapa, T. P. Ojha, G. E. Gehrels, & D. Collins (Eds.), *Structural and thermal evolution of the Himalayan Thrust Belt in Midwestern Nepal* (pp. 1–79). https://doi.org/10.1130/2020.2547(01

DeCelles, P. G., Castañeda, I. S., Carrapa, B., Liu, J., Quade, J., Leary, R., & Zhang, L. (2018). Oligocene-Miocene Great Lakes in the India-Asia Collision Zone. *Basin Research*, *30*, 228–247. https://doi.org/10.1111/bre.12217

DeCelles, P. G., & DeCelles, P. C. (2001). Rates of shortening, propagation, underthrusting, and flexural wave migration in continental orogenic systems. *Geology*, *29*(2), 135–138. https://doi.org/10.1130/0091-7613(2001)029<0135:Rospua>2.0.Co;2

DeCelles, P. G., Gehrels, G. E., Najman, Y., Martin, A. J., Carter, A., & Garzanti, E. (2004). Detrital geochronology and geochemistry of Cretaceous-early Miocene strata of Nepal: Implications for timing and diachroneity of initial Himalayan orogenesis. *Earth and Planetary Science Letters*, *227*(3–4), 313–330. https://doi.org/10.1016/j.epsl.2004.08.019

DeCelles, P. G., Gehrels, G. E., Quade, J., & Ojha, T. P. (1998a). Eocene-early Miocene foreland basin development and the history of Himalayan thrusting, western and central Nepal. *Tectonics*, *17*(5), 741–765. https://doi.org/10.1029/98TC02598

DeCelles, P. G., Gehrels, G. E., Quade, J., Ojha, T. P., Kapp, P. A., & Upreti, B. N. (1998b). Neogene foreland basin deposits, erosional unroofing, and the kinematic history of the Himalayan fold-thrust belt, western Nepal. *GSA Bulletin*, *110*(1), 2–21. https://doi.org/10.1130/0016-7606(1998)110<0002:Nfbdeu>2.3.Co;2

DeCelles, P. G., Kapp, P., Quade, J., & Gehrels, G. E. (2011). Oligocene-Miocene Kailas basin, southwestern Tibet: Record of postcollisional upper-plate extension in the Indus-Yarlung suture zone. *GSA Bulletin*, *123*(7–8), 1337–1362. https://doi.org/10.1130/B30258.1

DeCelles, P. G., Robinson, D. M., Quade, J., Ojha, T. P., Garzione, C. N., Copeland, P., & Upreti, B. N. (2001). Stratigraphy, structure, and tectonic evolution of the Himalayan fold-thrust belt in western Nepal. *Tectonics*, *20*(4), 487–509. https://doi.org/10.1029/2000TC001226

Ding, L., Spicer, R. A., Yang, J., Xu, Q., Cai, F., Li, S., et al. (2017). Quantifying the rise of the Himalaya orogen and implications for the South Asian monsoon. *Geology*, *45*, 215–218. https://doi.org/10.1130/G38583.1

Duncan, C., Masek, J., & Fielding, E. (2003). How steep are the Himalaya? Characteristics and implications of along-strike topographic variations. *Geology*, *31*(1), 75–78. https://doi.org/10.1130/0091-7613(2003)031<0075:HSATHC>2.0.CO;2

Duputel, Z., Vergne, J., Rivera, L., Wittlinger, G., Farra, V., & Hetényi, G. (2016). The 2015 Gorkha earthquake: A large event illuminating the Main Himalayan Thrust fault. *Geophysical Research Letters*, *43*, 2517–2525. https://doi.org/10.1002/2016GL068083

Edwards, M. A., Kidd, W. S. F., Li, J., Yue, Y., & Clark, M. (1996). Multi-stage development of the southern Tibet detachment system near Khula Kangri. New data from Gonto La. *Tectonophysics*, *260*(1), 1–19. https://doi.org/10.1016/0040-1951(96)00073-X

Eizenhöfer, P. R., McQuarrie, N., Shelef, E., & Ehlers, T. A. (2019). Landscape response to lateral advection in convergent orogens over geologic time scales. *Journal of Geophysical Research: Earth Surface*, *124*, 2056–2078. https://doi.org/10.1029/2019JF005100

Elliott, J. R., Jolivet, R., González, P. J., Avouac, J. P., Hollingsworth, J., Searle, M. P., & Stevens, V. L. (2016). Himalayan megathrust geometry and relation to topography revealed by the Gorkha earthquake. *Nature Geoscience*, *9*(2), 174–180. https://doi.org/10.1038/ngeo2623

England, P., & Molnar, P. (1990). Surface uplift, uplift of rocks, and exhumation of rocks. *Geology*, *18*(12), 1173–1177. https://doi.org/10.1130/0091-7613(1990)018<1173:Suuora>2.3.Co;2

Eugster, P., Thiede, R. C., Scherler, D., Stübner, K., Sobel, E. R., & Strecker, M. R. (2018). Segmentation of the Main Himalayan Thrust revealed by low-temperature thermochronometry in the Western Indian Himalaya. *Tectonics*, *37*, 2710–2726. https://doi.org/10.1029/2017TC004752

Fan, S. (2022). *Megathrust heterogeneity, crustal accretion, and a topographic embayment in the western Nepal Himalaya: Insights from the inversion of thermochronological data*. Texas Data Repository. https://doi.org/10.18738/T8/UU1YN1

Fan, S., & Murphy, M. A. (2021). Three-dimensional strain accumulation and partitioning in an arcuate orogenic wedge: An example from the Himalaya. *GSA Bulletin*, *133*(1–2), 3–18. https://doi.org/10.1130/B35528.1

Fuis, G. S., Moore, T. E., Plafker, G., Brocher, T. M., Fisher, M. A., Mooney, W. D., et al. (2008). Trans-Alaska Crustal transect and continental evolution involving subduction underplating and synchronous foreland thrusting. *Geology*, *36*(3), 267–270. https://doi.org/10.1130/G24257A.1

Fuis, G. S., Murphy, J. M., Lutter, W. J., Moore, T. E., Bird, K. J., & Christensen, N. I. (1997). Deep seismic structure and tectonics of northern Alaska: Crustal-scale duplexing with deformation extending into the upper mantle. *Journal of Geophysical Research*, *102*(B9), 20873–20896. https://doi.org/10.1029/96JB03959

Gaetani, M., & Garzanti, E. (1991). Multicyclic history of the Northern India Continental Margin (Northwestern Himalaya) (1). *AAPG Bulletin*, *75*(9), 1427–1446.

Galy, A., & France-Lanord, C. (2001). Higher erosion rates in the Himalaya: Geochemical constraints on riverine fluxes. *Geology*, *29*(1), 23–26. https://doi.org/10.1130/0091-7613(2001)029<0023:HERITH>2.0.CO;2

Gansser, A. (1964). *Geology of the Himalayas* (p. 289). New York, NY: Wiley Interscience.

Gao, R., Lu, Z., Klemperer, S. L., Wang, H., Dong, S., Li, W., & Li, H. (2016). Crustal-scale duplexing beneath the Yarlung Zangbo suture in the western Himalaya. *Nature Geoscience*, *9*(7), 555–560. https://doi.org/10.1038/ngeo2730

Garzanti, E., Vezzoli, G., Andò, S., Lavé, J., Attal, M., France-Lanord, C., & DeCelles, P. (2007). Quantifying sand provenance and erosion (Marsyandi River, Nepal Himalaya). *Earth and Planetary Science Letters*, *258*(3–4), 500–515. https://doi.org/10.1016/j.epsl.2007.04.010

Gébelin, A., Mulch, A., Teyssier, C., Jessup, M. J., Law, R. D., & Brunel, M. (2013). The Miocene elevation of Mount Everest. *Geology*, *41*(7), 799–802. https://doi.org/10.1130/G34331.1

Ghazoui, Z., Bertrand, S., Vanneste, K., Yokoyama, Y., Nomade, J., Gajurel, A. P., & van der Beek, P. A. (2019). Potentially large post-1505 AD earthquakes in western Nepal revealed by a lake sediment record. *Nature Communications*, *10*(1), 2258. https://doi.org/10.1038/s41467-019-10093-4

Ghosh, S., Bose, S., Mandal, N., & Laik, A. (2020). Mid-crustal ramping of the Main Himalayan Thrust in Nepal to Bhutan Himalaya: New insights from analogue and numerical experiments. *Tectonophysics*, *782–783*, 228425. https://doi.org/10.1016/j.tecto.2020.228425

Ghoshal, S., McQuarrie, N., Robinson, D. M., Adhikari, D. P., Morgan, L. E., & Ehlers, T. A. (2020). Constraining central Himalayan (Nepal) fault geometry through integrated thermochronology and thermokinematic modeling. *Tectonics*, *39*, e2020TC006399. https://doi.org/10.1029/2020YTC006399

Gibson, R., Godin, L., Kellett, D. A., Cottle, J. M., & Archibald, D. (2016). Diachronous deformation along the base of the Himalayan metamorphic core, west-central Nepal. *Geological Society of America Bulletin*, *128*(5–6), 860–878. https://doi.org/10.1130/B31328.1

Godard, V., Cattin, R., & Lavé, J. (2004). Numerical modeling of mountain building: Interplay between erosion law and crustal rheology. *Geophysical Research Letters*, *31*, L23607. https://doi.org/10.1029/2004GL021006

Godard, V., Cattin, R., & Lavé, J. (2009). Erosional control on the dynamics of low-convergence rate continental plateau margins. *Geophysical Journal International*, *179*(2), 763–777. https://doi.org/10.1111/j.1365-246X.2009.04324.x

Godin, L., Ahenda, M., Grujic, D., Stevenson, R., & Cottle, J. (2021). Protolith affiliation and tectonometamorphic evolution of the Gurla Mandhata core complex, NW Nepal Himalaya. *Geosphere*, *17*(2), 626–646. https://doi.org/10.1130/GES02326.1

Godin, L., Gleeson, T. P., Searle, M. P., Ullrich, T. D., & Parrish, R. R. (2006a). Locking of southward extrusion in favour of rapid crustal-scale buckling of the Greater Himalayan Sequence, Nar valley, central Nepal. *Geological Society, London, Special Publications*, *268*(1), 269–292. https://doi.org/10.1144/Gsl.Sp.2006.268.01.13

Godin, L., Grujic, D., Law, R. D., & Searle, M. P. (2006b). Channel flow, ductile extrusion and exhumation in continental collision zones: An introduction. *Geological Society, London, Special Publications*, *268*(1), 1–23. https://doi.org/10.1144/gsl.sp.2006.268.01.01

Godin, L., Parrish, R. R., Brown, R. L., & Hodges, K. V. (2001). Crustal thickening leading to exhumation of the Himalayan metamorphic core of central Nepal: Insight from U-Pb geochronology and $^{40}Ar/^{39}Ar$ thermochronology. *Tectonics*, *20*(5), 729–747. https://doi.org/10.1029/2000TC001204

Govin, G., Najman, Y., Dupont-Nivet, G., Millar, I., van der Beek, P., Huyghe, P., et al. (2018). The tectonics and paleo-drainage of the easternmost Himalaya (Arunachal Pradesh, India) recorded in the Siwalik rocks of the foreland basin. *American Journal of Science*, *318*(7), 764–798. https://doi.org/10.2475/07.2018.02

Grandin, R., Doin, M. P., Bollinger, L., Pinel-Puyssegur, B., Ducret, G., Jolivet, R., & Sapkota, S. N. (2012). Long-term growth of the Himalaya inferred from interseismic InSAR measurement. *Geology*, *40*(12), 1059–1062. https://doi.org/10.1130/G33154.1

Grujic, D., Ashley, K. T., Coble, M. A., Coutand, I., Kellett, D. A., Larson, K. P., et al. (2020). Deformational temperatures across the Lesser Himalayan Sequence in Eastern Bhutan and their implications for the deformation history of the main central thrust. *Tectonics*, *39*, e2019TC005914. https://doi.org/10.1029/2019TC005914

Grujic, D., Hollister, L. S., & Parrish, R. R. (2002). Himalayan metamorphic sequence as an orogenic channel: Insight from Bhutan. *Earth and Planetary Science Letters*, *198*(1–2), 177–191. https://doi.org/10.1016/S0012-821X(02)00482-X

Guo, X., Gao, R., Zhao, J., Xu, X., Lu, Z., Klemperer, S. L., & Liu, H. (2018). Deep-seated lithospheric geometry in revealing collapse of the Tibetan Plateau. *Earth-Science Reviews*, *185*, 751–762. https://doi.org/10.1016/j.earscirev.2018.07.013

Haproff, P. J., Odlum, M. L., Zuza, A. V., Yin, A., & Stockli, D. F. (2020). Structural and thermochronologic constraints on the Cenozoic tectonic development of the Northern Indo-Burma Ranges. *Tectonics*, *39*, e2020TC006231. https://doi.org/10.1029/2020TC006231

Harrison, T. M., Ryerson, F., Le Fort, P., Yin, A., Lovera, O. M., & Catlos, E. (1997). A late Miocene-Pliocene origin for the central Himalayan inverted metamorphism. *Earth and Planetary Science Letters*, *146*(1), E1–E7.

Harrison, T. M., Yin, A., Grove, M., Lovera, O. M., Ryerson, F., & Zhou, X. (2000). The Zedong Window: A record of superposed tertiary convergence in southeastern Tibet. *Journal of Geophysical Research*, *105*(B8), 19211–19230. https://doi.org/10.1029/2000JB900078

Harvey, J. E. (2015). *Along-strike tectonic variability in the central Himalaya (Ph.D.)*. Santa Barbara: University of California.

Harvey, J. E., Burbank, D. W., & Bookhagen, B. (2015). Along-strike changes in Himalayan thrust geometry: Topographic and tectonic discontinuities in western Nepal. *Lithosphere*, *7*, 511–518. https://doi.org/10.1130/L444.1

Hauck, M. L., Nelson, K. D., Brown, L. D., Zhao, W., & Ross, A. R. (1998). Crustal structure of the Himalayan orogen at ~90° east longitude from Project INDEPTH deep reflection profiles. *Tectonics*, *17*(4), 481–500. https://doi.org/10.1029/98TC01314

Heim, A., & Gansser, A. (1939). Geological observations of the Swiss Expedition (Vol. *73*, pp. 245).

Herman, F., Copeland, P., Avouac, J. P., Bollinger, L., Maheo, G., Le Fort, P., et al. (2010). Exhumation, crustal deformation, and thermal structure of the Nepal Himalaya derived from the inversion of thermochronological and thermobarometric data and modeling of the topography. *Journal of Geophysical Research: Solid Earth*, *115*, B06407. https://doi.org/10.1029/2008JB006126

Hetényi, G., Cattin, R., Berthet, T., Le Moigne, N., Chophel, J., Lechmann, S., et al. (2016). Segmentation of the Himalayas as revealed by arc-parallel gravity anomalies. *Scientific Reports*, *6*, 33866. https://doi.org/10.1038/srep33866

Hilley, G. E., & Strecker, M. R. (2005). Processes of oscillatory basin filling and excavation in a tectonically active orogen: Quebrada del Toro Basin, NW Argentina. *GSA Bulletin*, *117*(7–8), 887–901. https://doi.org/10.1130/B25602.1

Hodges, K., Bowring, S., Davidek, K., Hawkins, D., & Krol, M. (1998). Evidence for rapid displacement on Himalayan normal faults and the importance of tectonic denudation in the evolution of mountain ranges. *Geology*, *26*(6), 483–486. https://doi.org/10.1130/0091-7613(1998)026<0483:efrdoh>2.3.co;2

Hodges, K. V., Hurtado, J. M., & Whipple, K. X. (2001). Southward extrusion of Tibetan crust and its effect on Himalayan tectonics. *Tectonics*, *20*(6), 799–809. https://doi.org/10.1029/2001TC001281

Hodges, K. V., Parrish, R. R., Housh, T. B., Lux, D. R., Burchfiel, B. C., Royden, L. H., & Chen, Z. (1992). Simultaneous Miocene extension and shortening in the Himalayan Orogen. *Science*, *258*(5087), 1466–1470. https://doi.org/10.1126/science.258.5087.1466

Hodges, K. V., Wobus, C., Ruhl, K., Schildgen, T., & Whipple, K. (2004). Quaternary deformation, river steepening, and heavy precipitation at the front of the Higher Himalayan ranges. *Earth and Planetary Science Letters*, *220*(3–4), 379–389. https://doi.org/10.1016/s0012-821x(04)00063-9

Hossler, T., Bollinger, L., Sapkota, S. N., Lavé, J., Gupta, R. M., & Kandel, T. P. (2016). Surface ruptures of large Himalayan earthquakes in Western Nepal: Evidence along a reactivated strand of the Main Boundary Thrust. *Earth and Planetary Science Letters*, *434*, 187–196. https://doi.org/10.1016/j.epsl.2015.11.042

Hoste-Colomer, R., Bollinger, L., Lyon-Caen, H., Adhikari, L. B., Baillard, C., Benoit, A., et al. (2018). Lateral variations of the midcrustal seismicity in western Nepal: Seismotectonic implications. *Earth and Planetary Science Letters*, *504*, 115–125. https://doi.org/10.1016/j.epsl.2018.09.041

Hubbard, J., Almeida, R., Foster, A., Sapkota, S. N., Bürgi, P., & Tapponnier, P. (2016). Structural segmentation controlled the 2015 Mw7.8 Gorkha earthquake rupture in Nepal. *Geology*, *44*(8), 639–642. https://doi.org/10.1130/G38077.1

Hubbard, M. S., & Harrison, T. M. (1989). $^{40}Ar/^{39}Ar$ age constraints on deformation and metamorphism in the main central thrust zone and Tibetan slab, eastern Nepal Himalaya. *Tectonics*, *8*(4), 865–880. https://doi.org/10.1029/TC008i004p00865

Huntington, K. W., Blythe, A. E., & Hodges, K. V. (2006). Climate change and late Pliocene acceleration of erosion in the Himalaya. *Earth and Planetary Science Letters*, *252*(1–2), 107–118. https://doi.org/10.1016/j.epsl.2006.09.031

Huntington, K. W., & Hodges, K. V. (2006). A comparative study of detrital mineral and bedrock age-elevation methods for estimating erosion rates. *Journal of Geophysical Research*, *111*, F03011. https://doi.org/10.1029/2005JF000454

Hurtado, J. M., Hodges, K. V., & Whipple, K. X. (2001). Neotectonics of the Thakkhola graben and implications for recent activity on the South Tibetan fault system in the central Nepal Himalaya. *GSA Bulletin*, *113*(2), 222–240. https://doi.org/10.1130/0016-7606(2001)113<0222:NOTTGA>2.0.CO;2

Husson, L., Bernet, M., Guillot, S., Huyghe, P., Mugnier, J.-L., Replumaz, A., et al. (2014). Dynamic ups and downs of the Himalaya. *Geology*, *42*(10), 839–842. https://doi.org/10.1130/G36049.1

Hyndman, R. D., Yamano, M., & Oleskevich, D. A. (1997). The seismogenic zone of subduction thrust faults. *Island Arc*, *6*(3), 244–260. https://doi.org/10.1111/j.1440-1738.1997.tb00175.x

Iaccarino, S., Montomoli, C., Carosi, R., Massonne, H. J., & Visona, D. (2017). Geology and tectono-metamorphic evolution of the Himalayan metamorphic core: Insights from the Mugu Karnali transect, Western Nepal (Central Himalaya). *Journal of Metamorphic Geology*, *35*(3), 301–325. https://doi.org/10.1111/jmg.12233

Jackson, M., Barrientos, S., Bilham, R., Kyestha, D., & Shrestha, B. (1992). Uplift in the Nepal Himalaya revealed by spirit leveling. *Geophysical Research Letters*, *19*(15), 1539–1542. https://doi.org/10.1029/92GL01638

Jackson, M., & Bilham, R. (1994). Constraints on Himalayan deformation inferred from vertical velocity fields in Nepal and Tibet. *Journal of Geophysical Research*, *99*(B7), 13897–13912. https://doi.org/10.1029/94JB00714

Johnston, S. N., Cannon, J. M., & Copeland, P. (2020). Post-Miocene Erosion in central Nepal controlled by midcrustal ramp position, duplex growth, and dynamically maintained elastic strain. *Tectonics*, *39*, e2020TC006291. https://doi.org/10.1029/2020TC006291

Jordan, T. A., & Watts, A. B. (2005). Gravity anomalies, flexure and the elastic thickness structure of the India-Eurasia collisional system. *Earth and Planetary Science Letters*, *236*(3), 732–750. https://doi.org/10.1016/j.epsl.2005.05.036

Jouanne, F., Mugnier, J. L., Pandey, M. R., Gamond, J. F., Le Fort, P., Serrurier, L., et al. (1999). Oblique convergence in the Himalayas of western Nepal deduced from preliminary results of GPS measurements. *Geophysical Research Letters*, *26*(13), 1933–1936. https://doi.org/10.1029/1999GL900416

Jouanne, F., Mugnier, J. L., Sapkota, S. N., Bascou, P., & Pecher, A. (2017). Estimation of coupling along the Main Himalayan Thrust in the central Himalaya. *Journal of Asian Earth Sciences*, *133*, 62–71. https://doi.org/10.1016/j.jseaes.2016.05.028

Kellett, D. A., & Grujic, D. (2012). New insight into the South Tibetan detachment system: Not a single progressive deformation. *Tectonics*, *31*, TC2007. https://doi.org/10.1029/2011TC002957

Kellett, D. A., Grujic, D., Warren, C., Cottle, J., Jamieson, R., & Tenzin, T. (2010). Metamorphic history of a syn-convergent orogen-parallel detachment: The South Tibetan detachment system, Bhutan Himalaya. *Journal of Metamorphic Geology*, *28*(8), 785–808. https://doi.org/10.1111/j.1525-1314.2010.00893.x

Kohn, M. J. (2014). Himalayan metamorphism and its tectonic implications. *Annual Review of Earth and Planetary Sciences*, *42*(1), 381–419. https://doi.org/10.1146/annurev-earth-060313-055005

Kohn, M. J., Wieland, M. S., Parkinson, C. D., & Upreti, B. N. (2005). Five generations of monazite in Langtang gneisses: Implications for chronology of the Himalayan metamorphic core. *Journal of Metamorphic Geology*, *23*(5), 399–406. https://doi.org/10.1111/j.1525-1314.2005.00584.x

Kumar, A., Singh, S. K., Mitra, S., Priestley, K. F., & Dayal, S. (2017). The 2015 April 25 Gorkha (Nepal) earthquake and its aftershocks: Implications for lateral heterogeneity on the Main Himalayan Thrust. *Geophysical Journal International*, *208*(2), 992–1008. https://doi.org/10.1093/gji/ggw438

Landry, K. R., Coutand, I., Whipp, D. M., Grujic, D., & Hourigan, J. K. (2016). Late Neogene tectonically driven crustal exhumation of the Sikkim Himalaya: Insights from inversion of multithermochronologic data. *Tectonics*, *35*, 833–859. https://doi.org/10.1002/2015TC004102

Lang, K. A., & Huntington, K. W. (2014). Antecedence of the Yarlung-Siang-Brahmaputra River, eastern Himalaya. *Earth and Planetary Science Letters*, *397*, 145–158. https://doi.org/10.1016/j.epsl.2014.04.026

Larson, K. M., Bürgmann, R., Bilham, R., & Freymueller, J. T. (1999). Kinematics of the India-Eurasia collision zone from GPS measurements. *Journal of Geophysical Research*, *104*(B1), 1077–1093. https://doi.org/10.1029/1998JB900043

Larson, K. P., Ambrose, T. K., Webb, A. A. G., Cottle, J. M., & Shrestha, S. (2015). Reconciling Himalayan midcrustal discontinuities: The Main Central thrust system. *Earth and Planetary Science Letters*, *429*, 139–146. https://doi.org/10.1016/j.epsl.2015.07.070

Larson, K. P., Godin, L., & Price, R. A. (2010). Relationships between displacement and distortion in orogens: Linking the Himalayan foreland and hinterland in central Nepal. *Geological Society of America Bulletin*, *122*(7–8), 1116–1134. https://doi.org/10.1130/B30073.1

Laskowski, A. K., Kapp, P., & Cai, F. (2018). Gangdese culmination model: Oligocene-Miocene duplexing along the India-Asia suture zone, Lazi region, southern Tibet. *GSA Bulletin*, *130*(7–8), 1355–1376. https://doi.org/10.1130/B31834.1

Lavé, J., & Avouac, J. P. (2001). Fluvial incision and tectonic uplift across the Himalayas of central Nepal. *Journal of Geophysical Research*, *106*(B11), 26561. https://doi.org/10.1029/2001JB000359

Lee, J., Hacker, B. R., Dinklage, W. S., Wang, Y., Gans, P., Calvert, A., et al. (2000). Evolution of the Kangmar Dome, southern Tibet: Structural, petrologic, and thermochronologic constraints. *Tectonics*, *19*(5), 872–895. https://doi.org/10.1029/1999TC001147

Lee, J., & Whitehouse, M. J. (2007). Onset of mid-crustal extensional flow in southern Tibet: Evidence from U/Pb zircon ages. *Geology*, *35*(1), 45–48. https://doi.org/10.1130/G22842a.1

Le Fort, P. (1975). Himalayas: The collided range. Present knowledge of the continental arc. *American Journal of Science*, *275*(1), 1–44.

Li, G., Kohn, B., Sandiford, M., & Xu, Z. (2017). India-Asia convergence: Insights from burial and exhumation of the Xigaze fore-arc basin, south Tibet. *Journal of Geophysical Research: Solid Earth*, *122*, 3430–3449. https://doi.org/10.1002/2017JB014080

Li, G., Kohn, B., Sandiford, M., Xu, Z., Tian, Y., & Seiler, C. (2016). Synorogenic morphotectonic evolution of the Gangdese batholith, South Tibet: Insights from low-temperature thermochronology. *Geochemistry, Geophysics, Geosystems*, *17*, 101–112. https://doi.org/10.1002/2015GC006047

Li, S., Wang, Q., Yang, S., Qiao, X., Nie, Z., Zou, R., et al. (2018). Geodetic imaging mega-thrust coupling beneath the Himalaya. *Tectonophysics*, *747–748*, 225–238. https://doi.org/10.1016/j.tecto.2018.08.014

Liu, G., & Einsele, G. (1994). Sedimentary history of the Tethyan basin in the Tibetan Himalayas. *Geologische Rundschau*, *83*(1), 32–61. https://doi.org/10.1007/BF00211893

Lyon-Caen, H., & Molnar, P. (1985). Gravity anomalies, flexure of the Indian Plate, and the structure, support and evolution of the Himalaya and Ganga Basin. *Tectonics*, *4*(6), 513–538. https://doi.org/10.1029/TC004i006p00513

Malavieille, J. (2010). Impact of erosion, sedimentation, and structural heritage on the structure and kinematics of orogenic wedges: Analog models and case studies. *GSA Today*, 4–10. https://doi.org/10.1130/gsatg48a.1

Marechal, A., Mazzotti, S., Cattin, R., Cazes, G., Vernant, P., Drukpa, D., et al. (2016). Evidence of interseismic coupling variations along the Bhutan Himalayan arc from new GPS data. *Geophysical Research Letters*, *43*, 12399–12406. https://doi.org/10.1002/2016GL071163

Martin, A. J., Copeland, P., & Benowitz, J. A. (2015). Muscovite $^{40}Ar/^{39}Ar$ ages help reveal the Neogene tectonic evolution of the southern Annapurna Range, central Nepal. *Geological Society, London, Special Publications*, *412*(1), 199–220. https://doi.org/10.1144/sp412.5

Martin, A. J., Ganguly, J., & DeCelles, P. G. (2009). Metamorphism of Greater and Lesser Himalayan rocks exposed in the Modi Khola valley, central Nepal. *Contributions to Mineralogy and Petrology*, *159*(2), 203–223. https://doi.org/10.1007/s00410-009-0424-3

Masek, J. G., Isacks, B. L., Gubbels, T. L., & Fielding, E. J. (1994). Erosion and tectonics at the margins of continental plateaus. *Journal of Geophysical Research*, *99*(B7), 13941–13956. https://doi.org/10.1029/94JB00461

McCallister, A. T., Taylor, M. H., Murphy, M. A., Styron, R. H., & Stockli, D. F. (2014). Thermochronologic constraints on the late Cenozoic exhumation history of the Gurla Mandhata metamorphic core complex, Southwestern Tibet. *Tectonics*, *33*, 27–52. https://doi.org/10.1002/2013TC003302

McDermott, J. A., Whipple, K. X., Hodges, K. V., & van Soest, M. C. (2013). Evidence for Plio-Pleistocene north-south extension at the southern margin of the Tibetan Plateau, Nyalam region. *Tectonics*, *32*(3), 317–333. https://doi.org/10.1002/tect.20018

McQuarrie, N., Eizenhöfer, P. R., Long, S. P., Tobgay, T., Ehlers, T. A., Blythe, A. E., et al. (2019). The influence of foreland structures on hinterland cooling: Evaluating the drivers of exhumation in the Eastern Bhutan Himalaya. *Tectonics*, *38*, 3282–3310. https://doi.org/10.1029/2018TC005340

Mendoza, M. M., Ghosh, A., Karplus, M. S., Klemperer, S. L., Sapkota, S. N., Adhikari, L. B., & Velasco, A. (2019). Duplex in the Main Himalayan Thrust illuminated by aftershocks of the 2015 Mw 7.8 Gorkha earthquake. *Nature Geoscience*, *12*, 1018–1022. https://doi.org/10.1038/s41561-019-0474-8

Mercier, J. (2014). *Structure and evolution of orogenic wedges: A multidisciplinary study on the Himalayan case (Ph.D.)*. Université de Grenoble.

Mercier, J., Braun, J., & van der Beek, P. (2017). Do along-strike tectonic variations in the Nepal Himalaya reflect different stages in the accretion cycle? Insights from numerical modeling. *Earth and Planetary Science Letters*, *472*, 299–308. https://doi.org/10.1016/j.epsl.2017.04.041

Molnar, P. (1984). Structure and tectonics of the Himalaya: Constraints and implications of geophysical data. *Annual Review of Earth and Planetary Sciences*, *12*(1), 489–516.

Molnar, P., & Lyon-Caen, H. (1988). Some simple physical aspects of the support, structure, and evolution of mountain belts. In J. S. P. Clark, B. C. Burchfiel, & J. Suppe (Eds.), *Processes in continental lithospheric deformation*. Geological Society of America.

Montemagni, C., Montomoli, C., Iaccarino, S., Carosi, R., Jain, A. K., Massonne, H.-J., & Villa, I. M. (2019). Dating protracted fault activities: Microstructures, microchemistry and geochronology of the Vaikrita Thrust, Main Central Thrust zone, Garhwal Himalaya, NW India. *Geological Society, London, Special Publications*, *481*(1), 127–146. https://doi.org/10.1144/sp481.3

Montomoli, C., Carosi, R., & Iaccarino, S. (2015). *Tectonometamorphic discontinuities in the Greater Himalayan Sequence: A local or a regional feature?* (Vol. 412). Geological Society, London, Special Publications. https://doi.org/10.1144/sp412.3

Montomoli, C., Iaccarino, S., Carosi, R., Langone, A., & Visona, D. (2013). Tectonometamorphic discontinuities within the Greater Himalayan Sequence in Western Nepal (Central Himalaya): Insights on the exhumation of crystalline rocks. *Tectonophysics*, *608*, 1349–1370. https://doi.org/10.1016/j.tecto.2013.06.006

Moore, T. E., Wallace, W. K., Mull, C. G., Adams, K. E., Plafker, G., & Nokleberg, W. J. (1997). Crustal implications of bedrock geology along the Trans-Alaska Crustal Transect (TACT) in the Brooks Range, northern Alaska. *Journal of Geophysical Research*, *102*(B9), 20645–20684. https://doi.org/10.1029/96JB03733

Morell, K. D., Sandiford, M., Kohn, B., Codilean, A., Fulop, R. H., & Ahmad, T. (2017). Current strain accumulation in the hinterland of the northwest Himalaya constrained by landscape analyses, basin-wide denudation rates, and low temperature thermochronology. *Tectonophysics*, *721*, 70–89. https://doi.org/10.1016/j.tecto.2017.09.007

Morell, K. D., Sandiford, M., Rajendran, C. P., Rajendran, K., Alimanovic, A., Fink, D., & Sanwal, J. (2015). Geomorphology reveals active décollement geometry in the central Himalayan seismic gap. *Lithosphere*, *7*(3), 247–256. https://doi.org/10.1130/L407.1

Mugnier, J. L., Baby, P., Colletta, B., Vinour, P., Bale, P., & Leturmy, P. (1997). Thrust geometry controlled by erosion and sedimentation: A view from analogue models. *Geology*, *25*(5), 427–430. https://doi.org/10.1130/0091-7613(1997)025<0427:tgcbea>2.3.co;2

Mugnier, J.-L., & Huyghe, P. (2006). Ganges basin geometry records a pre-15 Ma isostatic rebound of Himalaya. *Geology*, *34*(6), 445–448. https://doi.org/10.1130/g22089.1

Mugnier, J. L., Jouanne, F., Bhattarai, R., Cortes-Aranda, J., Gajurel, A., Leturmy, P., et al. (2017). Segmentation of the Himalayan megathrust around the Gorkha earthquake (25 April 2015) in Nepal. *Journal of Asian Earth Sciences*, *141*, 236–252. https://doi.org/10.1016/j.jseaes.2017.01.015

Mugnier, J. L., Leturmy, P., Mascle, G., Huyghe, P., Chalaron, E., Vidal, G., et al. (1999). The Siwaliks of western Nepal: I. Geometry and kinematics. *Journal of Asian Earth Sciences*, *17*(5–6), 629–642. https://doi.org/10.1016/S1367-9120(99)00038-3

Murphy, M. A. (2007). Isotopic characteristics of the Gurla Mandhata metamorphic core complex: Implications for the architecture of the Himalayan orogen. *Geology*, *35*(11), 983–986. https://doi.org/10.1130/g23774a.1

Murphy, M. A., & Burgess, W. P. (2006). Geometry, kinematics, and landscape characteristics of an active transtension zone, Karakoram fault system, Southwest Tibet. *Journal of Structural Geology*, *28*(2), 268–283. https://doi.org/10.1016/j.jsg.2005.10.009

Murphy, M. A., & Copeland, P. (2005). Transtensional deformation in the central Himalaya and its role in accommodating growth of the Himalayan orogen. *Tectonics*, *24*, TC4012. https://doi.org/10.1029/2004TC001659

Murphy, M. A., & Harrison, M. T. (1999). Relationship between leucogranites and the Qomolangma detachment in the Rongbuk Valley, south Tibet. *Geology*, *27*(9), 831–834. https://doi.org/10.1130/0091-7613(1999)027<0831:rblatq>2.3.co;2

Murphy, M. A., Taylor, M. H., Gosse, J., Silver, C. R. P., Whipp, D. M., & Beaumont, C. (2014). Limit of strain partitioning in the Himalaya marked by large earthquakes in western Nepal. *Nature Geoscience*, *7*(1), 38–42. https://doi.org/10.1038/Ngeo2017

Murphy, M. A., & Yin, A. (2003). Structural evolution and sequence of thrusting in the Tethyan fold-thrust belt and Indus-Yalu suture zone, southwest Tibet. *Geological Society of America Bulletin*, *115*(1), 21–34. https://doi.org/10.1130/0016-7606(2003)115<0021:Seasot>2.0.Co;2

Murphy, M. A., Yin, A., Kapp, P., Harrison, T. M., Manning, C. E., Ryerson, F. J., et al. (2002). Structural evolution of the Gurla Mandhata detachment system, southwest Tibet: Implications for the eastward extent of the Karakoram fault system. *Geological Society of America Bulletin*, *114*(4), 428–447. https://doi.org/10.1130/0016-7606(2002)114<0428:Seotgm>2.0.Co;2

Myrow, P. M., Hughes, N. C., Searle, M. P., Fanning, C. M., Peng, S. C., & Parcha, S. K. (2009). Stratigraphic correlation of Cambrian-Ordovician deposits along the Himalaya: Implications for the age and nature of rocks in the Mount Everest region. *Geological Society of America Bulletin*, *121*(3–4), 323–332. https://doi.org/10.1130/B26384.1

Nábělek, J., Hetényi, G., Vergne, J., Sapkota, S., Kafle, B., Jiang, M., et al. (2009). Underplating in the Himalaya-Tibet Collision Zone revealed by the Hi-CLIMB experiment. *Science*, *325*(5946), 1371–1374. https://doi.org/10.1126/science.1167719

Nadin, E. S., & Martin, A. J. (2012). Apatite thermochronometry within a knickzone near the higher Himalaya front, central Nepal: No resolvable fault motion in the past one million years. *Tectonics*, *31*, TC2010. https://doi.org/10.1029/2011TC003000

Nagy, C., Godin, L., Antolín, B., Cottle, J., & Archibald, D. (2015). Mid-Miocene initiation of orogen-parallel extension, NW Nepal Himalaya. *Lithosphere*, *7*(5), 483–502. https://doi.org/10.1130/L425.1

Naito, N., Ageta, Y., Iwata, S., Matsuda, Y., Suzuki, R., & Karma, Y. (2006). Glacier shrinkages and climate conditions around Jichu Dramo Glacier in the Bhutan Himalayas from 1998 to 2003. *Bulletin of Glaciological Research*, *23*, 51–61.

Najman, Y., Carter, A., Oliver, G., & Garzanti, E. (2005). Provenance of Eocene foreland basin sediments, Nepal: Constraints to the timing and diachroneity of early. Himalayan orogenesis. *Geology*, *33*(4), 309–312. https://doi.org/10.1130/G21161.1

Najman, Y., & Garzanti, E. (2000). Reconstructing early Himalayan tectonic evolution and paleogeography from Tertiary foreland basin sedimentary rocks, northern India. *Geological Society of America Bulletin*, *112*(3), 435–449.
Ni, J., & Barazangi, M. (1984). Seismotectonics of the Himalayan Collision Zone: Geometry of the underthrusting Indian Plate beneath the Himalaya. *Journal of Geophysical Research*, *89*(B2), 1147–1163. https://doi.org/10.1029/JB089iB02p01147
Ojha, L., Ferrier, K. L., & Ojha, T. (2019). Millennial-scale denudation rates in the Himalaya of far western Nepal. *Earth Surface Dynamics*, *7*(4), 969–987. https://doi.org/10.5194/esurf-7-969-2019
Olsen, J. E. S., McQuarrie, N., & Robinson, D. M. (2019). Determining kinematic order and relative age of faulting via flexural-kinematic restoration: A case study in far western Nepal. *Basin Research*, *31*, 1153–1177. https://doi.org/10.1111/bre.12362
Orme, D. A. (2019). Burial and exhumation history of the Xigaze forearc basin, Yarlung suture zone, Tibet. *Geoscience Frontiers*, *10*(3), 895–908. https://doi.org/10.1016/j.gsf.2017.11.011
Pajang, S., Le Pourhiet, L., & Cubas, N. (2022). The topographic signature of temperature-controlled rheological transitions in an accretionary prism. *Solid Earth*, *13*(3), 535–551. https://doi.org/10.5194/se-13-535-2022
Pearson, O. N., & DeCelles, P. G. (2005). Structural geology and regional tectonic significance of the Ramgarh thrust, Himalayan fold-thrust belt of Nepal. *Tectonics*, *24*, TC4008. https://doi.org/10.1029/2003TC001617
Pêcher, A. (1989). The metamorphism in the Central Himalaya. *Journal of Metamorphic Geology*, *7*(1), 31–41. https://doi.org/10.1111/j.1525-1314.1989.tb00573.x
Pingel, H., Strecker, M. R., Mulch, A., Alonso, R. N., Cottle, J., & Rohrmann, A. (2020). Late Cenozoic topographic evolution of the Eastern Cordillera and Puna Plateau margin in the southern Central Andes (NW Argentina). *Earth and Planetary Science Letters*, *535*, 116112. https://doi.org/10.1016/j.epsl.2020.116112
Quidelleur, X., Grove, M., Lovera, O. M., Harrison, T. M., Yin, A., & Ryerson, F. J. (1997). Thermal evolution and slip history of the Renbu Zedong Thrust, southeastern Tibet. *Journal of Geophysical Research*, *102*(B2), 2659–2679. https://doi.org/10.1029/96JB02483
Ratschbacher, L., Frisch, W., Liu, G., & Chen, C. (1994). Distributed deformation in southern and western Tibet during and after the India-Asia collision. *Journal of Geophysical Research*, *99*(B10), 19917–19945. https://doi.org/10.1029/94JB00932
Reiners, P. W. (2005). Zircon (U-Th)/He thermochronometry. *Reviews in Mineralogy and Geochemistry*, *58*(1), 151–179. https://doi.org/10.2138/rmg.2005.58.6
Reiners, P. W., Spell, T. L., Nicolescu, S., & Zanetti, K. A. (2004). Zircon (U-Th)/He thermochronometry: He diffusion and comparisons with $^{40}Ar/^{39}Ar$ dating. *Geochimica et Cosmochimica Acta*, *68*(8), 1857–1887. https://doi.org/10.1016/j.gca.2003.10.021
Rickwood, P., & Sambridge, M. (2006). Efficient parallel inversion using the Neighbourhood Algorithm. *Geochemistry, Geophysics, Geosystems*, *7*, Q11001. https://doi.org/10.1029/2006GC001246
Robert, X., van der Beek, P., Braun, J., Perry, C., Dubille, M., & Mugnier, J. L. (2009). Assessing Quaternary reactivation of the Main Central thrust zone (central Nepal Himalaya): New thermochronologic data and numerical modeling. *Geology*, *37*(8), 731–734. https://doi.org/10.1130/G25736a.1
Robert, X., van der Beek, P., Braun, J., Perry, C., & Mugnier, J. L. (2011). Control of detachment geometry on lateral variations in exhumation rates in the Himalaya: Insights from low-temperature thermochronology and numerical modeling. *Journal of Geophysical Research: Solid Earth*, *116*, B05202. https://doi.org/10.1029/2010JB007893
Robinson, D. M. (2008). Forward modeling the kinematic sequence of the central Himalayan thrust belt, western Nepal. *Geosphere*, *4*(5), 785. https://doi.org/10.1130/GES00163.1
Robinson, D. M., DeCelles, P. G., & Copeland, P. (2006). Tectonic evolution of the Himalayan thrust belt in western Nepal: Implications for channel flow models. *Geological Society of America Bulletin*, *118*(7–8), 865–885. https://doi.org/10.1130/B25911.1
Robinson, D. M., DeCelles, P. G., Garzione, C. N., Pearson, O. N., Harrison, T. M., & Catlos, E. J. (2003). Kinematic model for the Main Central thrust in Nepal. *Geology*, *31*(4), 359–362. https://doi.org/10.1130/0091-7613(2003)031<0359:kmftmc>2.0.co;2
Robinson, D. M., DeCelles, P. G., Patchett, P. J., & Garzione, C. N. (2001). The kinematic evolution of the Nepalese Himalaya interpreted from Nd isotopes. *Earth and Planetary Science Letters*, *192*(4), 507–521. https://doi.org/10.1016/S0012-821X(01)00451-4
Robinson, D. M., & McQuarrie, N. (2012). Pulsed deformation and variable slip rates within the central Himalayan thrust belt. *Lithosphere*, *4*(5), 449–464. https://doi.org/10.1130/L204.1
Ruetenik, G. A., Hoke, G. D., Moucha, R., & Val, P. (2018). Regional landscape response to thrust belt dynamics: The Iglesia basin, Argentina. *Basin Research*, *30*(6), 1141–1154. https://doi.org/10.1111/bre.12295
Sakai, H., Iwano, H., Danhara, T., Hirata, T., & Takigami, Y. (2013). Emplacement of hot Lesser Himalayan nappes from 15 to 10 Ma in the Jumla-Surkhet region, western Nepal, and their thermal imprint on the underlying early Miocene fluvial Dumri Formation. *Island Arc*, *22*(3), 361–381. https://doi.org/10.1111/iar.12030
Sambridge, M. (1999a). Geophysical inversion with a neighbourhood algorithm—I. Searching a parameter space. *Geophysical Journal International*, *138*(2), 479–494. https://doi.org/10.1046/j.1365-246X.1999.00876.x
Sambridge, M. (1999b). Geophysical inversion with a neighbourhood algorithm—II. Appraising the ensemble. *Geophysical Journal International*, *138*(3), 727–746. https://doi.org/10.1046/j.1365-246x.1999.00900.x
Sample, J. C., & Fisher, D. M. (1986). Duplex accretion and underplating in an ancient accretionary complex, Kodiak Islands, Alaska. *Geology*, *14*(2), 160–163. https://doi.org/10.1130/0091-7613(1986)14<160:Daauia>2.0.Co;2
Schelling, D. (1992). The tectonostratigraphy and structure of the Eastern Nepal Himalaya. *Tectonics*, *11*(5), 925–943. https://doi.org/10.1029/92TC00213
Scherler, D., Bookhagen, B., & Strecker, M. R. (2014). Tectonic control on ^{10}Be-derived erosion rates in the Garhwal Himalaya, India. *Journal of Geophysical Research: Earth Surface*, *119*, 83–105. https://doi.org/10.1002/2013JF002955
Schill, E., Appel, E., Crouzet, C., Gautam, P., Wehland, F., & Staiger, M. (2004). Oroclinal bending versus regional significant clockwise rotations in the Himalayan arc—Constraints from secondary pyrrhotite remanences. *Geological Society of America Special Papers*, *383*, 73–85. https://doi.org/10.1130/0-8137-2383-3(2004)383[73:obvrsc]2.0.co;2
Searle, M., Windley, B., Coward, M., Cooper, D., Rex, A., Rex, D., et al. (1987). The closing of Tethys and the tectonics of the Himalaya. *Geological Society of America Bulletin*, *98*(6), 678–701.
Searle, M. P. (2010). Low-angle normal faults in the compressional Himalayan orogen: Evidence from the Annapurna-Dhaulagiri Himalaya, Nepal. *Geosphere*, *6*(4), 296–315. https://doi.org/10.1130/GES00549.1
Searle, M. P., & Godin, L. (2003). The South Tibetan Detachment and the Manaslu Leucogranite: A structural reinterpretation and restoration of the Annapurna-Manaslu Himalaya, Nepal. *The Journal of Geology*, *111*(5), 505–523. https://doi.org/10.1086/376763
Seeber, L., Armbruster, J. G., & Quittmeyer, R. C. (1981). Seismicity and continental subduction in the Himalayan arc. In *Zagros Hindu Kush, Himalaya Geodynamic Evolution* (pp. 215–242). https://doi.org/10.1029/GD003p0215

Seeber, L., & Gornitz, V. (1983). River profiles along the Himalayan arc as indicators of active tectonics. *Tectonophysics*, *92*(4), 335–367. https://doi.org/10.1016/0040-1951(83)90201-9

Shen, L., Jia, D., Zhang, Z., Chen, Z., Yin, H., Wu, X., et al. (2020). Tectonic underplating versus out-of-sequence thrusting beneath the Lesser Himalaya: Insights from the analogue modeling of the Nepal Himalaya fold-and-thrust belt. *Journal of Asian Earth Sciences*, *198*, 104167. https://doi.org/10.1016/j.jseaes.2019.104167

Shen, T., Wang, G., Leloup, P. H., van der Beek, P., Bernet, M., Cao, K., et al. (2016). Controls on Cenozoic exhumation of the Tethyan Himalaya from fission-track thermochronology and detrital zircon U-Pb geochronology in the Gyirong basin area, southern Tibet. *Tectonics*, *35*, 1713–1734. https://doi.org/10.1002/2016TC004149

Shi, Z., Gao, R., Li, W., Lu, Z., & Li, H. (2020). Cenozoic crustal-scale duplexing and flat Moho in southern Tibet: Evidence from reflection seismology. *Tectonophysics*, *790*, 228562. https://doi.org/10.1016/j.tecto.2020.228562

Silver, C. R. P., Murphy, M. A., Taylor, M. H., Gosse, J., & Baltz, T. (2015). Neotectonics of the Western Nepal Fault System: Implications for Himalayan strain partitioning. *Tectonics*, *34*, 2494–2513. https://doi.org/10.1002/2014TC003730

Singer, J., Obermann, A., Kissling, E., Fang, H. J., Hetenyi, G., & Grujic, D. (2017). Along-strike variations in the Himalayan orogenic wedge structure in Bhutan from ambient seismic noise tomography. *Geochemistry, Geophysics, Geosystems*, *18*, 1483–1498. https://doi.org/10.1002/2016GC006742

Sobel, E. R., Hilley, G. E., & Strecker, M. R. (2003). Formation of internally drained contractional basins by aridity-limited bedrock incision. *Journal of Geophysical Research*, *108*(B7), 2344. https://doi.org/10.1029/2002JB001883

Soucy La Roche, R., & Godin, L. (2019). Inherited cross-strike faults and Oligocene-early Miocene segmentation of the Main Himalayan Thrust, West Nepal. *Journal of Geophysical Research: Solid Earth*, *124*, 7429–7444. https://doi.org/10.1029/2019JB017467

Soucy La Roche, R., Godin, L., Cottle, J. M., & Kellett, D. A. (2018). Preservation of the early evolution of the Himalayan middle crust in foreland klippen: Insights from the Karnali klippe, west Nepal. *Tectonics*, *37*, 1161–1193. https://doi.org/10.1002/2017TC004847

Sreejith, K. M., Sunil, P. S., Agrawal, R., Saji, A. P., Rajawat, A. S., & Ramesh, D. S. (2018). Audit of stored strain energy and extent of future earthquake rupture in central Himalaya. *Scientific Reports*, *8*(1), 16697. https://doi.org/10.1038/s41598-018-35025-y

Srivastava, P., & Mitra, G. (1994). Thrust geometries and deep structure of the outer and lesser Himalaya, Kumaon and Garhwal (India): Implications for evolution of the Himalayan fold-and-thrust belt. *Tectonics*, *13*(1), 89–109. https://doi.org/10.1029/93TC01130

Stevens, V. L., & Avouac, J. P. (2015). Interseismic coupling on the main Himalayan thrust. *Geophysical Research Letters*, *42*, 5828–5837. https://doi.org/10.1002/2015GL064845

Stübner, K., Grujic, D., Dunkl, I., Thiede, R., & Eugster, P. (2018). Pliocene episodic exhumation and the significance of the Munsiari thrust in the northwestern Himalaya. *Earth and Planetary Science Letters*, *481*, 273–283. https://doi.org/10.1016/j.epsl.2017.10.036

Subedi, S., Hetényi, G., Vergne, J., Bollinger, L., Lyon-Caen, H., Farra, V., et al. (2018). Imaging the Moho and the Main Himalayan Thrust in Western Nepal with receiver functions. *Geophysical Research Letters*, *45*, 13222–13230. https://doi.org/10.1029/2018GL080911

Suppe, J. (1983). Geometry and kinematics of fault-bend folding. *American Journal of Science*, *283*(7), 684–721. https://doi.org/10.2475/ajs.283.7.684

Szulc, A. G., Najman, Y., Sinclair, H. D., Pringle, M., Bickle, M., Chapman, H., et al. (2006). Tectonic evolution of the Himalaya constrained by detrital ^{40}Ar-^{39}Ar, Sm-Nd and petrographic data from the Siwalik foreland basin succession, SW Nepal. *Basin Research*, *18*(4), 375–391. https://doi.org/10.1111/j.1365-2117.2006.00307.x

Taylor, M., Forte, A., Laskowski, A., & Ding, L. (2021). Active uplift of southern Tibet revealed. *Geological Society of America Today*, *31*(8), 4–10. https://doi.org/10.1130/gsatg487a.1

Thiede, R., Robert, X., Stubner, K., Dey, S., & Faruhn, J. (2017). Sustained out-of-sequence shortening along a tectonically active segment of the Main Boundary thrust: The Dhauladhar Range in the northwestern Himalaya. *Lithosphere*, *9*(5), 715–725. https://doi.org/10.1130/L630.1

Thiede, R. C., Arrowsmith, J. R., Bookhagen, B., McWilliams, M. O., Sobel, E. R., & Strecker, M. R. (2005). From tectonically to erosionally controlled development of the Himalayan orogen. *Geology*, *33*(8), 689–692. https://doi.org/10.1130/G21483.1

Thiede, R. C., Bookhagen, B., Arrowsmith, J. R., Sobel, E. R., & Strecker, M. R. (2004). Climatic control on rapid exhumation along the Southern Himalayan Front. *Earth and Planetary Science Letters*, *222*(3–4), 791–806. https://doi.org/10.1016/j.epsl.2004.03.015

Thiede, R. C., & Ehlers, T. A. (2013). Large spatial and temporal variations in Himalayan denudation. *Earth and Planetary Science Letters*, *371–372*, 278–293. https://doi.org/10.1016/j.epsl.2013.03.004

Thiede, R. C., Ehlers, T. A., Bookhagen, B., & Strecker, M. R. (2009). Erosional variability along the northwest Himalaya. *Journal of Geophysical Research*, *114*, F01015. https://doi.org/10.1029/2008JF001010

Tremblay, M. M., Fox, M., Schmidt, J. L., Tripathy-Lang, A., Wielicki, M. M., Harrison, T. M., et al. (2015). Erosion in southern Tibet shut down at approximately 10 Ma due to enhanced rock uplift within the Himalaya. *Proceedings of the National Academy of Sciences of the United States of America*, *112*(39), 12030–12035. https://doi.org/10.1073/pnas.1515652112

van der Beek, P., Litty, C., Baudin, M., Mercier, J., Robert, X., & Hardwick, E. (2016). Contrasting tectonically driven exhumation and incision patterns, western versus central Nepal Himalaya. *Geology*, *44*(4), 327–330. https://doi.org/10.1130/G37579.1

van der Beek, P., Robert, X., Mugnier, J.-L., Bernet, M., Huyghe, P., & Labrin, E. (2006). Late Miocene—Recent exhumation of the central Himalaya and recycling in the foreland basin assessed by apatite fission-track thermochronology of Siwalik sediments, Nepal. *Basin Research*, *18*(4), 413–434. https://doi.org/10.1111/j.1365-2117.2006.00305.x

Vance, D., Bickle, M., Ivy-Ochs, S., & Kubik, P. W. (2003). Erosion and exhumation in the Himalaya from cosmogenic isotope inventories of river sediments. *Earth and Planetary Science Letters*, *206*(3–4), 273–288. https://doi.org/10.1016/s0012-821x(02)01102-0

Vannay, J. C., & Hodges, K. V. (1996). Tectonometamorphic evolution of the Himalayan metamorphic core between the Annapurna and Dhaulagiri, central Nepal. *Journal of Metamorphic Geology*, *14*(5), 635–656. https://doi.org/10.1046/j.1525-1314.1996.00426.x

Wang, A., Garver, J. I., Wang, G., Smith, J. A., & Zhang, K. (2010). Episodic exhumation of the Greater Himalayan Sequence since the Miocene constrained by fission track thermochronology in Nyalam, central Himalaya. *Tectonophysics*, *495*(3–4), 315–323. https://doi.org/10.1016/j.tecto.2010.09.037

Wang, C., Gao, R., Yin, A., Wang, H., Zhang, Y., Guo, T., et al. (2011). A mid-crustal strain-transfer model for continental deformation: A new perspective from high-resolution deep seismic-reflection profiling across NE Tibet. *Earth and Planetary Science Letters*, *306*(3), 279–288. https://doi.org/10.1016/j.epsl.2011.04.010

Wang, X., Wei, S., & Wu, W. (2017). Double-ramp on the Main Himalayan Thrust revealed by broadband waveform modeling of the 2015 Gorkha earthquake sequence. *Earth and Planetary Science Letters*, *473*(Suppl. C), 83–93. https://doi.org/10.1016/j.epsl.2017.05.032

Wang, Y., Day, S. M., & Denolle, M. A. (2019). Geometric controls on pulse-like rupture in a dynamic model of the 2015 Gorkha Earthquake. *Journal of Geophysical Research: Solid Earth*, *124*, 1544–1568. https://doi.org/10.1029/2018JB016602

Webb, A. A. G. (2013). Preliminary balanced palinspastic reconstruction of Cenozoic deformation across the Himachal Himalaya (northwestern India). *Geosphere*, *9*(3), 572–587. https://doi.org/10.1130/GES00787.1

Webb, A. A. G., Guo, H., Clift, P. D., Husson, L., Müller, T., Costantino, D., et al. (2017). The Himalaya in 3D: Slab dynamics controlled mountain building and monsoon intensification. *Lithosphere*, *9*(4), 637–651. https://doi.org/10.1130/L636.1

Webb, A. A. G., Yin, A., Harrison, T. M., Célérier, J., & Burgess, W. P. (2007). The leading edge of the Greater Himalayan crystalline complex revealed in the NW Indian Himalaya: Implications for the evolution of the Himalayan orogen. *Geology*, *35*(10), 955. https://doi.org/10.1130/G23931a.1

Whipp, D. M., Ehlers, T. A., Blythe, A. E., Huntington, K. W., Hodges, K. V., & Burbank, D. W. (2007). Plio-Quaternary exhumation history of the central Nepalese Himalaya: 2. Thermokinematic and thermochronometer age prediction model. *Tectonics*, *26*, TC3003. https://doi.org/10.1029/2006TC001991

Whipple, K. X., Shirzaei, M., Hodges, K. V., & Ramon Arrowsmith, J. (2016). Active shortening within the Himalayan orogenic wedge implied by the 2015 Gorkha earthquake. *Nature Geoscience*, *9*(9), 711–716. https://doi.org/10.1038/ngeo2797

Williams, C. A., Connors, C., Dahlen, F. A., Price, E. J., & Suppe, J. (1994). Effect of the brittle-ductile transition on the topography of compressive mountain belts on Earth and Venus. *Journal of Geophysical Research*, *99*(B10), 19947–19974. https://doi.org/10.1029/94JB01407

Wissinger, E. S., Levander, A., & Christensen, N. I. (1997). Seismic images of crustal duplexing and continental subduction in the Brooks Range. *Journal of Geophysical Research*, *102*(B9), 20847–20871. https://doi.org/10.1029/96JB03662

Wobus, C., Heimsath, A., Whipple, K., & Hodges, K. (2005). Active out-of-sequence thrust faulting in the central Nepalese Himalaya. *Nature*, *434*(7036), 1008–1011.

Wobus, C. W., Hodges, K. V., & Whipple, K. X. (2003). Has focused denudation sustained active thrusting at the Himalayan topographic front? *Geology*, *31*(10), 861–864. https://doi.org/10.1130/G19730.1

Wobus, C. W., Whipple, K. X., & Hodges, K. V. (2006). Neotectonics of the central Nepalese Himalaya: Constraints from geomorphology, detrital $^{40}Ar/^{39}Ar$ thermochronology, and thermal modeling. *Tectonics*, *25*, TC4011. https://doi.org/10.1029/2005TC001935

Xu, Q., Zhao, J., Yuan, X., Liu, H., & Pei, S. (2017). Detailed configuration of the underthrusting Indian lithosphere beneath Western Tibet revealed by receiver function images. *Journal of Geophysical Research: Solid Earth*, *122*, 8257–8269. https://doi.org/10.1002/2017JB014490

Yadav, R. K., Gahalaut, V. K., Bansal, A. K., Sati, S. P., Catherine, J., Gautam, P., et al. (2019). Strong seismic coupling underneath Garhwal-Kumaun region, NW Himalaya, India. *Earth and Planetary Science Letters*, *506*, 8–14. https://doi.org/10.1016/j.epsl.2018.10.023

Yin, A. (2006). Cenozoic tectonic evolution of the Himalayan orogen as constrained by along-strike variation of structural geometry, exhumation history, and foreland sedimentation. *Earth-Science Reviews*, *76*(1–2), 1–131. https://doi.org/10.1016/j.earscirev.2005.05.004

Yin, A., Harrison, M. T., Murphy, M. A., Grove, M., Nie, S., Ryerson, F., et al. (1999). Tertiary deformation history of southeastern and southwestern Tibet during the Indo-Asian collision. *Geological Society of America Bulletin*, *111*(11), 1644–1664. https://doi.org/10.1130/0016-7606(1999)111<1644:Tdhosa>2.3.Co;2

Yin, A., Harrison, T. M., Ryerson, F. J., Chen, W. J., Kidd, W. S. F., & Copeland, P. (1994). Tertiary structural evolution of the Gangdese Thrust System, Southeastern Tibet. *Journal of Geophysical Research*, *99*(B9), 18175–18201. https://doi.org/10.1029/94JB00504

Yuan, X. P., Huppert, K. L., Braun, J., Shen, X., Liu-Zeng, J., Guerit, L., et al. (2021). Propagating uplift controls on high-elevation, low-relief landscape formation in the southeast Tibetan Plateau. *Geology*, *50*(1), 60–65. https://doi.org/10.1130/G49022.1

Zhang, J. Y., Yin, A., Liu, W. C., Wu, F. Y., Lin, D., & Grove, M. (2012). Coupled U-Pb dating and Hf isotopic analysis of detrital zircon of modern river sand from the Yalu River (Yarlung Tsangpo) drainage system in southern Tibet: Constraints on the transport processes and evolution of Himalayan rivers. *Geological Society of America Bulletin*, *124*(9–10), 1449–1473. https://doi.org/10.1130/B30592.1

Zhang, Y., Wang, R., Walter, T. R., Feng, W., Chen, Y., & Huang, Q. (2017). Significant lateral dip changes may have limited the scale of the 2015 Mw 7.8 Gorkha earthquake. *Geophysical Research Letters*, *44*, 8847–8856. https://doi.org/10.1002/2017GL074095

Zuza, A. V., Wu, C., Wang, Z., Levy, D. A., Li, B., Xiong, X., & Chen, X. (2018). Underthrusting and duplexing beneath the northern Tibetan Plateau and the evolution of the Himalayan-Tibetan orogen. *Lithosphere*, *11*(2), 209–231. https://doi.org/10.1130/L1042.1